Micro and Nano-patterning of Graphene and Graphene Oxide for Biosensing Applications

NG MING HUA ANDREW

NATIONAL UNIVERSITY OF SINGAPORE

2015

Micro and Nano-patterning of Graphene and Graphene Oxide for Bio-sensing Applications

NG MING HUA ANDREW
B.Sc (Hons)
Curtin University of Technology, Perth, Australia

A THESIS SUBMITTED

FOR THE DEGREE OF DOCTOR OF PHILOSPHY

DEPARTMENT OF CHEMISTRY

NATIONAL UNIVERSITY OF SINGAPORE

2015

Declaration

I hereby declare that this thesis is my original work and it has been written by me in its entirety, under the supervision of Prof Loh Kian Ping, (in the laboratory Graphene Research Centre), Chemistry Department, National University of Singapore and Institute of Materials Research and Engineering, between 2010 and 2015.

I have duly acknowledged all the sources of information which have been used in the thesis.

This thesis has also not been submitted for any degree in any university previously.

The content of the thesis has been partly published in:

1) Carbon (Chapter 3)

2) Biosensors and Bioelectronics (Chapter 4)

Ng Ming Hua, Andrew		12 December 2015
Name	Signature	Date

Acknowledgments

This thesis was only possible due to the constant support and encouragement of the people around me.

I would like to thank my supervisor Prof Loh Kian Ping for his advice and guidance which has allowed me to become a better researcher. His drive and creativity are truly inspiring.

I would like to thank my co-supervisor Prof Low Hong Yee whose insights and solutions have allowed me to prioritize and understand what matters the most. Her enthusiasm and focus is something I aspire to emulate.

I would like to thank those who I have worked with over the course of my thesis Prof Lim Chwee Teck, Hendrix Tanoto, Tan Wui Siew, Priscilla Ang, Kenry, Wang Yu, Jacky Lee and Vincent Lim. Thank you for your efforts and valuable input.

To my colleagues at IMRE, Goh Seok Hong, Man Shu Mei and Lim Su Hui thanks for being a source of encouragement in those times when it was needed.

To my friends that constantly are there for me in times of need Rowie, Howie, Jean, Victor, Sue Anne, Jasper, Vicky, Wendy, Pastor Josh, Brendon, Daniel and Adrian your presence has provided a safe harbor for me when times got rough. Special thank you to YW who has constantly been there and for keeping an eye out for me during my journey and through it all.

To J P Veder and L dyer Laurence - some of the smartest people I know, thanks for your valuable input, help, and most of all your friendship. It really is a privilege.

I would like to thank my dad and mum who always believed in me, and allowed me to explore my world. Your method of parenting grew my curiosity to understand and deconstruct what was going on around me. To Joey, Nick and Janice, although you have no idea the content of my research, thank you for your endless support and encouragement.

I would like to thank my son Ethan. Even after a disappointing day in the lab, coming home to your smile and laughter always made the day better and, finally to my beautiful wife Karen - none of this would have been even remotely possible without you. Thank you for putting up with me during the stressful times, and being strong for the family. Your loving words and hugs have been so important in keeping me going. I love you with all my heart and this thesis is dedicated to you.

List of Publications

1. **Ng, A. M. H**., Kenry, null, Teck Lim, C., Low, H. Y. & Loh, K. P. Highly sensitive reduced graphene oxide microelectrode array sensor. Biosens. Bioelectron. **65C**, 265–273 (2014).

2. **Ng, A. M. H**., Wang, Y., Lee, W. C., Lim, C. T., Loh, K. P. & Low, H. Y. Patterning of graphene with tunable size and shape for microelectrode array devices. Carbon **67**, 390–397 (2014).

3. Kajen, R. S., Chandrasekhar, N., Pey, K. L., Vijila, C., Jaiswal, M., Saravanan, S., **Ng, A. M. H**., Wong, C. P. & Loh, K. P. Trap Levels in Graphene Oxide: A Thermally Stimulated Current Study. ECS Solid State Lett. **2**, 17–19 (2013).

4. Kajen, R. S., Chandrasekhar, N., Pey, K. L., Vijila, C., Jaiswal, M., Saravanan, S., **Ng, A. M. H**., Wong, C. P. & Loh, K. P. Charge transport in lightly reduced graphene oxide: A transport energy perspective. J. Appl. Phys. **113**, 063710 (2013).

Patents Granted

SG Patent Application No. 201400407-1 (Filing Date: 17 January 2014)
Invention: Method to Fabricate Graphene Microelectrode Array via Nanoimprint Technology
Inventors: Ng Ming Hua, Andrew, Low Hong Yee, Loh Kian Ping
ETPL ref: IMR/P/07550/01/SG
IMRE ref: 201233

Table of Contents

Summary

Graphene and its derivatives have shown to possess exceptional electronic and physical properties. One of the areas that show graphene's promise is in the area of electrochemical sensing. In the drive to move this material towards sensing applications, there are two major challenges that need to be addressed. 1) Manipulating the nanometre thick graphene materials on a large scale. 2) Understanding the sensing behavior of reduced graphene oxide as an electroactive material under microelectrode array conditions.

This thesis describes the manipulation of chemical vapor deposition (CVD) graphene and reduced graphene oxide. The atomically thin material was manipulated into various shapes and sizes such as microdiscs and hexagonal rings on a large scale through the use of nanoimprint lithography. The patterned graphene was encapsulated in a PMMA layer and could be transferred onto other substrates such as SiO2 and glass. A graphene microelectrode array sensor (MEA) device was fabricated using a novel self-aligning technique, that was developed using a water soluble imprint resist, coupled with a water insoluble polymer material. The device was used to detect H_2O_2 that was secreted by MCF-7 breast cancer cells, seeded at a low density of 3000 cells cm^{-2}.

The mild process conditions of the self-aligning technique allowed MEA fabrication on flexible plastic substrates. A reduced graphene oxide MEA (rGO MEA) biosensor was fabricated. The rGO MEA was used to detect dopamine and tyrosine and found to have higher sensitivities than other reported graphene based sensors. The device was also compared to a

commercial gold microelectrode and was found to be over 3 orders of magnitude more sensitive than the commercial gold microelectrode towards dopamine. The device was also integrated into a microfluidic system and showed excellent steady state currents in dopamine detection even in a flowing environment.

Optimization of MEA density was investigated to determine the minimum interelectrode spacing to maximize MEA performance. This was done by characterizing rGO MEAs of various interelectrode spacings using cyclic voltammetry to determine at which spacing microelectrode behavior occurred. The optimum ratio of interelectrode spacing to microelectrode radius would serve as a guide rule for future rGO based MEA devices.

Lastly, an rGO – Fmoc FF nanocomposite (rGO NC) electro active layer that would allow for uniform coating over large areas and increased device sensitivities was investigated. This was done by determining the concentration and pH for peptide fibril formation without critical hydrogel cluster formation. The Fmoc-FF peptide self-assembled into a network that allowed for a higher number of exposed rGO active sites which increased current gains of the sensor without needing to increase the sensor size. The rGO NC was used to detect serotonin even in the presence of dopamine and ascorbic acid interferents showing the potential for this nanocomposite to be used as an active layer in future biosensor devices.

List of Tables

List of Figures

Figure 4.1. (a) PVA is spin coated onto electrochemically reduced graphene oxide (rGO). (b) PVA layer is patterned into a pillar array through NIL. (c) Patterned PVA layer is etched down to remove unwanted rGO, leaving PVA pillars protecting the rGO active layer array. (d) PMMA layer is spin-coated on top of the patterned and etched PVA layer. (e) PMMA layer etched to expose PVA layer. (f) PVA layer is dissolved in DI water to reveal underlying rGO active layer. The final product consists of exposed rGO disk array surrounded by PMMA, the latter passivates the unexposed area from the electrolyte.

Figure 4.2. (a) Schematic of diffusion hemisphere overlapping when microelectrodes are fabricated in close proximity and no overlapping of diffusion hemispheres when microelectrodes are fabricated at pitch distances greater than twice the radius of the diffusion hemisphere. (b) CV data with increasing scan rate, using a 0.25 cm^2 rGO macroelectrode. (c) CV data of rGO MEA with 30 µm pitch spacing. (d) CV data of rGO MEA with 60 µm pitch spacing. (e) SEM image of rGO layer inside an exposed microelectrode.

Figure 4.3. (a) Comparison of rGO MEA and Au microelectrode. Inset shows surface of rGO MEA with 10 µm microelectrode holes. (b) CA of Au microelectrode towards 100 µM injections of DA. Top inset shows image of gold active layer, bottom inset shows calibration graph. (c) CA of rGO MEA towards 20 µM injections of DA. Top inset shows single microelectrode and bottom inset shows calibration graph. (d) Simultaneous detection of DA and Tyrosine (Tyro) using DPV.

Figure 4.4. CA graph of hydrogen peroxide. 3 x 10 µM H_2O_2 injected followed by 8 x 50 µM injections. Inset calibration graph.

Figure 4.5. (a) CV of rGO macroelectrode in 0.1M KCl solution. (b) CV of rGO MEA in 0.1M KCl solution. (c) CV of rGO macroelectrode in DI water. (d) CV of rGO MEA in DI Water.

Figure 4.6. (a) Image of the rGO MEA device in the microfluidic system. (b) Steady state currents for differing concentrations of DA pumping through the microfluidic channel. (c) Example of CA response to the flowing of 25 µM DA and flushing with pure Na-PBS.

Figure 4.7. DPV spectra of rGO MEA device showing fouling caused by AA and after cleaning at 0.6 V in 0.1 M Na-PBS solution for 3 minutes the fouling is removed and the device performance is unchanged.

Figure 4.8. (a) rGO MEA device cut from ITO/PET substrate where it is fabricated on. (b) Comparison of rGO MEA performance towards DA when flexed at different radius of curvatures. (c) Flex tests of rGO MEA device over

Figure 6.15. DPV spectra of Serotonin (5-HT) detection using one layer rGO NC with interfering dopamine (DA) and ascorbic acid (AA) compounds.

Figure 6.16. (a) Optical image of transferred PMMA layer onto rGO NC substrate. The 4 10 μm diameter microelectrode holes can be clearly seen. (b) CV voltammogram of the device showing MEA characteristics.

List of Abbreviations and Symbols

CA	Chronoamperometry
CV	Cyclic Voltammetry
CVD	Chemical Vapor Deposition
DA	Dopamine
DI	Deionized
DPV	Differential Pulse Voltammetry
FET	Field Effect Transistor
Fmoc-FF	N-fluorenylmethoxycarbonyldiphenylalanine
FTO	Fluorine tin oxide
GMEA	Graphene Microelectrode Array
GO NC	Graphene Oxide Nanocomposite
GO	Graphene Oxide
GOMEA	Graphene oxide microelectrode array
ITO	Indium Tin Oxide
ITOMEA	Indium Tin Oxide Microelectrode Array
MEA	Microelectrode Array
Na-PBS	Sodium Phosphate Buffered Saline
NIL	Nanoimprint Lithography

PBS	Phosphate Buffer Saline
PC	Poly carbonate
PDMS	Polydimethylsiloxane
PEDOT	Poly(3,4-ethylenedioxythiophene)
PET	Polyethylene Teraphthalate
PMA	Phorbal 12-myristate 13-acetate
PMMA	Poly methyl methacrylate
PVA	Polyvinyl Alcohol
rGO NC	Reduced Grapheen Oxide Nanocomposite
rGO	Reduced Graphene Oxide
rGOMEA	Reduced Graphene Oxide Microelectrode Array
SEM	Scanning Electron Microscopy
SPE	Screen Printed Electrodes
Tg	Glass transition temperature
XPS	X-Ray Photoelectron Spectroscopy
c	Concentration
Cd	Double Layer Capacitance
D	Diffusion Coefficient
DA_c	Concentration of Dopamine

D_r	Diffusion Radius
E_d	Interelectrode Distance
E_r	Radius of Electrode
F	Faradays Constant
i	Current
L	Microelectrode Recess depth over radius of microelectrode
n	Moles
r	Radius of microelectrode
R_u	Uncompensated Resistance
t	Time
$Tyro_c$	Concentration of Tyrosine

Chapter 1. Introduction

1.1. Graphene

Graphene, since its discovery in 2004, has garnered intense research into its electrical and physical properties.[1] Graphene is found in a hexagonal lattice formation consisting of sp^2 hybridized carbon atoms (Figure 1). Out of the four valence electrons, three are used to form strong σ bonds with neighboring carbon atoms in the 2s, $2p_x$ and $2p_y$ orbitals. The fourth electron lies in the $2p_z$ orbital orientated perpendicular to the basal plane. Due to the close interatomic distances of the carbon atoms, (0.142 nm) the $2p_z$ orbitals overlap, allowing the fourth delocalized electron to obtain large Fermi velocities even at room temperature.[2]

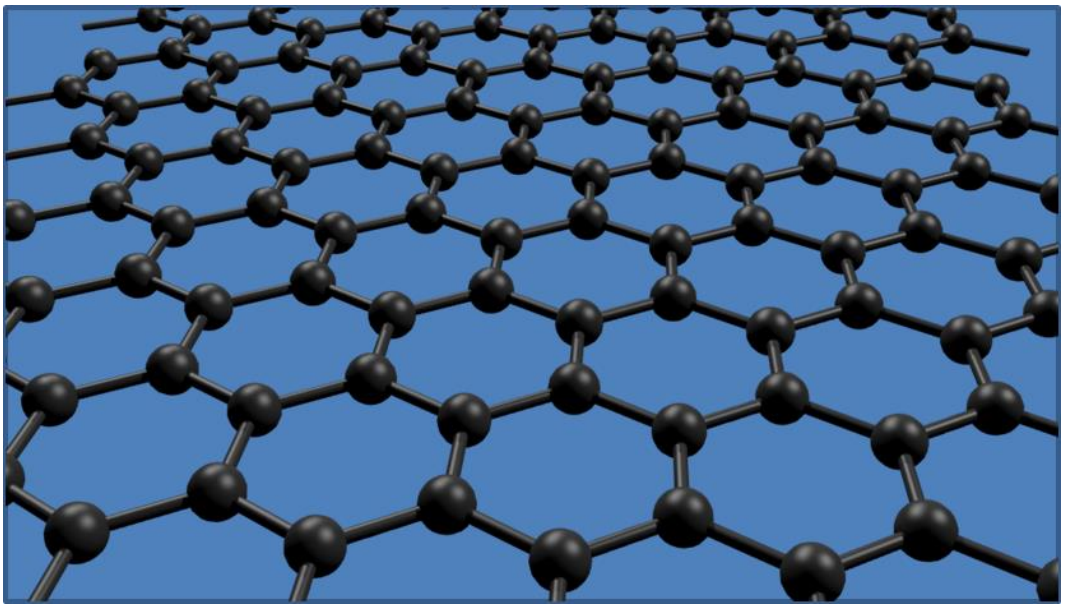

Figure 1.1. Schematic diagram of Graphene lattice

In the early stages of graphene research, characterizing graphene and its properties was the main research thrust. It has been reported that graphene is the strongest material currently found with a measured Young's modulus of 1 TPa[3] and intrinsic strength of 130 GPa,[4] the fastest conductor of electricity possessing ballistic conduction at room temperatures,[5] has a high heat conductivity,[6] is inert to many chemical attacks,[7] is flexible[8] and is optically transparent where one sheet of graphene allows 97.7% transmission of visible light.[9] These characteristics have spurred a large impetus to drive graphene research towards applications.

1.2. Graphene Oxide

Graphene also comes in other derivative forms - Graphene oxide (GO) and reduced graphene oxide (rGO). GO is a graphene layer that has oxygen moieties such as epoxides, hydroxyl, carbonyl and phenol groups strewn across the surface (Figure 1.2).[10] Although graphene loses much of its inherent attractive characteristics in this form due to the disruption of the π conjugation,[11] the benefits of using graphene oxide is that it is water soluble.[12] The oxygen atoms attached to the surface of the individual graphene sheets repel adjacent graphene oxide sheets keeping them suspended in solution.

Solution processing allows another avenue of fabricating graphene-based devices. Graphene synthesis commonly used chemical vapor deposition (CVD) techniques that would require high vacuum and temperature conditions limiting graphene production.[13] GO provides a quick method to create a large

amount of graphene based material that could be deposited over a large area via drop casting or spin coating.

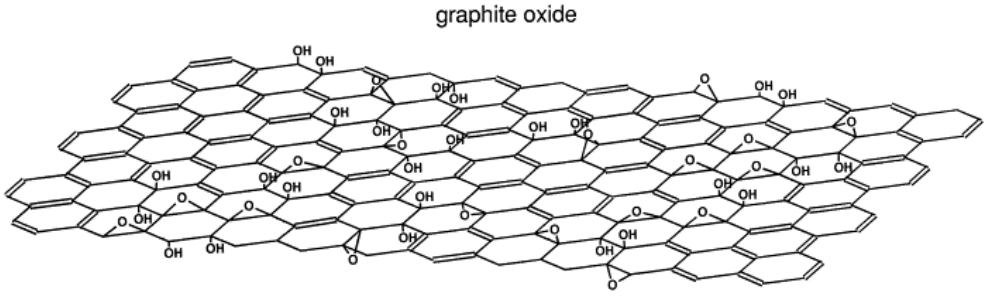

Figure 1.2. Schematic diagram of a GO layer. Reproduced with permission from ref 14.

1.3. Reduced Graphene Oxide

In order to recover the electrical properties of graphene from GO, several methods have been used to remove the oxygen moieties to restore the pi-pi bonds.[15] One method is to expose the GO sheets to ultraviolet irradiation.[16] Thermal annealing in a furnace has also been reported to be an effective method to remove oxygen groups.[17,18] Another method is through chemical reduction processes using reagents such as hydrazine and sodium borohydride[19,20]. A last method is electrochemical reduction where a high negative potential is passed through the GO layer to remove the oxygen groups and restore the π conjugation.[21,22]

It must be noted that although electrical conductivity can be restored, the current reduction methods are limited and can leave behind defects within the graphene layer or is unable to remove all oxygen groups. Consequently, rGO's conductivity will always be lower when compared to the conductivity

found in pristine graphene.[23, 24] However, the conductivity of rGO is still large enough to be useful in applications especially in electrochemical sensing.

1.4. Electrochemistry

A sensor is a device that detects events or changes in environments and outputs these reactions as an electrical signal. They are used across the whole spectrum of the research field and come in various shapes, sizes and uses. Sensors have been built to detect physical changes such as temperature and pressure, and to detect the presence of bioanalytes such as DNA and small gas molecules. At the basic structure of a sensor, the working parts must be conductive and so graphene, which exhibits excellent electrical properties, has seen a natural progression as a research topic in this field.

1.4.1. Electrochemical Sensor Operation

The mechanism for electrochemical sensing occurs when an electron transfer event takes place between the target analyte and the electrode. Electron transfer can occur when the electrode potentials are driven to higher negative or positive potentials causing the energy the electrons acquire to be sufficient enough to transfer into vacant electronic states on the analyte, thus creating a cathodic current (Figure 1.3(a)) or lowered to a point where the electrons on the analyte deems it more energy favorable to transfer to the electrode, creating an anodic current (Figure 1.3(b)).[31] This type of transfer is called a faradaic process. The potentials at which electron transfer occurs are related

to the standard potentials, and vary depending on target analytes and electrode types. The charge that is detected from the electron transfer is stoichiometrically related to the concentration of the analyte and can therefore be used to measure the amount of analyte in a given environment.

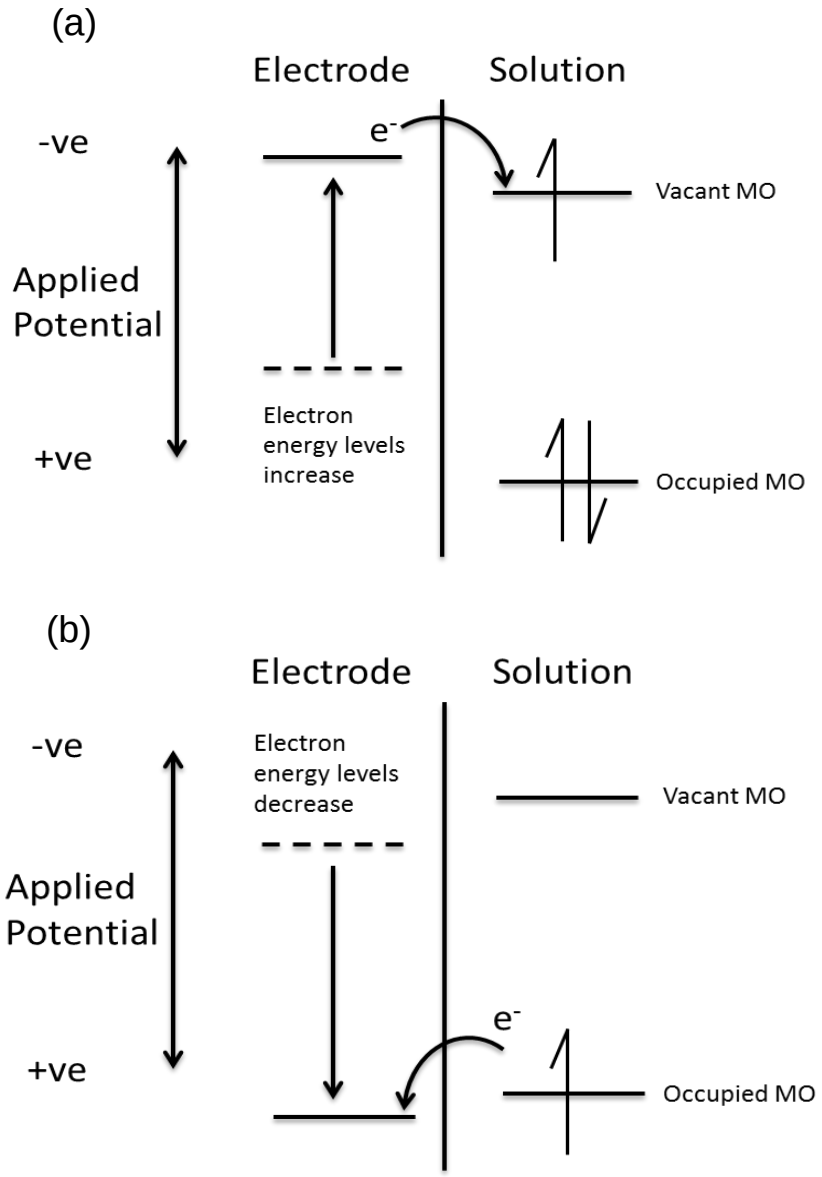

Figure 1.3. (a) Electron transfer from electrode to analyte LUMO when sufficient negative potentials are reached causing a cathodic current. (b) Electron transfer from analyte HOMO to electrode when sufficient positive potential is applied.

There are two types of processes that occur at electrodes. As previously discussed, one process is referred to as a faradaic process where electron transfer occurs across the solution and into the electrode. The other process that can occur is caused by adsorption and desorption of ions in the electrolyte solution that can cause currents to flow. This process is a non-faradaic current and must be taken into account when analyzing electrochemical data.[31]

Sensors that operate via electrochemical detection have four main modes of function. These are changes in capacitance, voltage, current and resistance.[32] The environment of sensing, target analyte, and sensor system will determine which method would be most suitable. Care must also be taken in the design of the sensor so that perturbations in the capacitance, voltage, current or resistance is caused only by the target analyte. Otherwise, false positives can readily occur.

1.4.2. Microelectrodes

A microelectrode is loosely classified as any sensor that has an active layer size in the micron regime. Largely ignored until the mid-80's, microelectrodes have since secured its place in fundamental and applied studies within the field of electrochemistry. Microelectrodes can be fabricated in various shapes, such as hemispheres, discs, wire and ring types.[36]

Microelectrodes have sparked much interest due to several advantages over macroelectrodes. Firstly, their smaller sizes allow their use in areas that otherwise cannot accommodate the size of a macroelectrode. Also, a microelectrode's smaller footprint allows it to be less invasive, which is important when dealing with biological systems.

Microelectrodes also reduce the contribution to charging currents. As potentials are changed, electrons move into or away from the electrode surface. This current flow is not a result of the electron transfer from the target analyte and can distort experimental results. Therefore, increasing the ratio of the faradaic contribution to the charging current is desirable when using a sensor. It has been studied that the charging current is proportional to the square of the radius of the microelectrode area and since the faradaic current is linearly proportional, reducing the size of the sensor results in an increase in the faradaic to charging current ratio.[37]

Lastly microelectrodes are less susceptible to iR drop. As current flows from the counter electrode to the working electrode, a potential field is generated which leads to a partial 'loss' of the applied potential. This results in the potential at the working electrode 'lagging' the applied potential at the

potentiostat which can critically distort output data especially the onset potential of oxidation/reduction values. The iR drop is related to the square of the working electrodes radius, similar to the charging current. Thus as a sensor moves into a microelectrode scale size, the effect of iR drop is lessened. In controlled experiments, where iR drop is a greater problem for macroelectrodes, higher supporting electrolyte concentrations can be used to mitigate the onset of iR drop.[38] However, in real world systems, manipulation of the electrolyte concentration may not be feasible and therefore shows the usage of microelectrodes to be clearly superior in this regard.

It has been reported that graphene based microelectrodes have been fabricated and used in the detection of dopamine (DA) and in a composite microelectrode neural sensor, showing that the electrical performance of graphene at the micro scale is promising even at these dimensions.[39,40]

1.4.3. Diffusion Layer

A diffusion layer occurs in the area near an electrode surface where the concentration of the target analyte differs from the concentration in the bulk solution. The difference in these concentration levels causes diffusion of the target analyte towards the electrode. The size of this diffusion layer is largely dependent on the diffusion coefficient of the analyte, the size of the electrode and the scan rate used. For macroelectrodes, the diffusion layer is planar and extends perpendicular from the surface of the electrode.[31] The diffusion layer changes profile as the electrode active area scales down to micron regimes. As the size is reduced, the edges of the diffusion layer have a greater influence

on the diffusion profile and push it from a planar form to a hemispherical one. This hemispherical diffusion profile allows for a greater flux of analyte towards the electrode.[41] As mentioned previously, since iR drop and charging currents are smaller when dealing with microelectrode regimes, the increase in analyte and therefore electron transfer to the electrode surface improves the signal to noise ratio of the microelectrode sensor significantly. Figure 1.4 shows a typical microelectrode CV. As can be seen, the difference between a typical macroelectrode CV (Figure 2.10) and a microelectrode CV (Figure 1.4) is that the microelectrode CV is sigmoidal in shape and does not contain the characteristic peaks and large depletion zone usually associated with macroelectrode CVs. Instead, a steady state current is seen. This is due to the increased diffusion flux of the analyte towards the microelectrodes surface. The diffusion is fast enough to replenish the depleted analyte resulting in the sigmoidal shape that is characteristic of a microelectrode.[36]

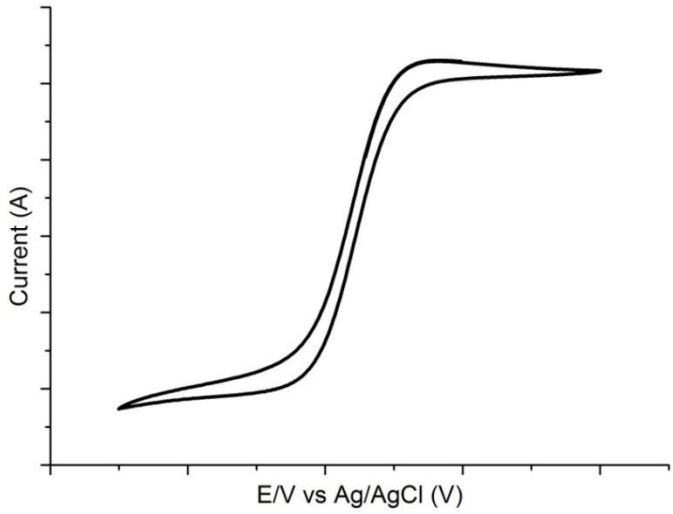

Figure 1.4. Typical sigmoidal shape of a CV voltammogram of a microelectrode.

1.4.4. Microelectrode array

As discussed, microelectrodes have many advantages that are attractive in the area of electrochemistry. However, due to the small sizes of a microelectrode, current signals are extremely small and usually in the nano to pico amp range. These small currents can put great strain on conventional electrochemical equipment or require expensive noise filtering components.[38] However, a way to overcome this limitation of small current signals is to fabricate the microelectrode into an array format. In an array configuration, each microelectrode works in parallel resulting in a larger overall signal.[42]

However, the pitch spacing between individual microelectrodes on a microelectrode array (MEA) must be taken into account. As previously discussed, a diffusion layer hemisphere forms during the operation of a microelectrode. The radius of this hemisphere is dependent on the electroactive material kinetics involved in oxidizing/reducing the target analyte, the scan rate used and the radius of the microelectrode. Overlap of the diffusion hemisphere between the microelectrodes in the array must be avoided otherwise the system shifts back into a macroelectrode regime, resulting in the loss of all benefits associated with microelectrodes.[43]

There have been reports of carbon based MEAs utilizing carbon nanotubes or carbon nanofibres as the electro active area.[44,45] However, these techniques require photolithography and high temperature CVD processes to fabricate, which can be a limiting factor in terms of scaling. Other graphene based MEA attempts have been reported by Li et al., which details reducing a GO surface at selective areas using a stamp method of hydrazine polydimethylsiloxane

(PDMS) wells.[46] The drawback with this is that after time, the unreduced GO areas of the surface will become active and therefore the device will eventually lose its MEA characteristics. There have also been other reports of rGO microelectrode array bands. Ueno et al. reports using photolithography to fabricate rGO/Au microarray bands to study the redox cycling of *p*-aminophenol.[47] Hsiao et al. also fabricates a rGO-Poly(3,4-ethylenedioxythiophene) (PEDOT) microarray band device that was then used to promote the adhesion and accelerate differentiation of human mesenchymal stem cells.[48] However, these reports do not investigate how the rGO active layer affects the performance of the MEA device itself. Little consideration has been given to how rGO performs and the fabrication guide rules required for a graphene based MEA device to operate in a microelectrode regime, which still leaves the question, 'What is the optimal interelectrode distance for an rGO MEA?'. This will be addressed in Chapter 5.

1.4.5. MEA Diffusion Types

As previously mentioned, a microelectrode will exhibit hemispherical diffusion profiles. Typically this will always result in a sigmoidal shaped cyclic voltammogram. However, in an array format the diffusion hemispheres now have a chance to interact with neighboring microelectrode diffusion hemispheres. The extent of this interaction is dependent on the interelectrode spacing of the microelectrode and the scan rate used. At faster scan times, the diffusion hemisphere has less time to increase in size from the active layer surface. The shorter diffusion hemisphere radius means the

chance for overlap is less likely. Conversely, at longer scan times, the diffusion hemispheres have more time to increase in size and diffusion overlap is more likely if the interelectrode spacing is close enough.[49]

Figure 1.6 shows computer simulations showing the 5 main categories for MEA diffusion types and their corresponding voltammograms. Category 1 (Figure 1.6a) occurs when electrode radius ($E_{r)}$ >> diffusion hemisphere radius (D_r). The individual microelectrode behaves as a macroelectrode and the resulting profile is peak-shaped. Category 2 (Figure 1.6b) shows diffusion hemispheres that overlap, resulting in a profile between peak-shaped and sigmoidal. Category 3 (Figure 1.6c) shows $E_r << D_{r.}$ However the interelectrode distance is spaced far apart enough so that the diffusion hemispheres do not overlap and the profile is sigmoid, showing steady state characteristics. Category 4 (Figure 1.6d) occurs when $E_r << D_r$ but the interelectrode spacing is close enough so that there is still some interaction between neighboring diffusion hemispheres. This results in a mixed diffusion regime whose profile is in between peak and sigmoidal shaped voltammgrams. Category 5 (Figure 1.6e) occurs when the diffusion layer completely overlaps with its adjacent diffusion hemisphere pushing the diffusion profile back into a planar regime which results in a macroelectrode peak-shaped voltammogram.

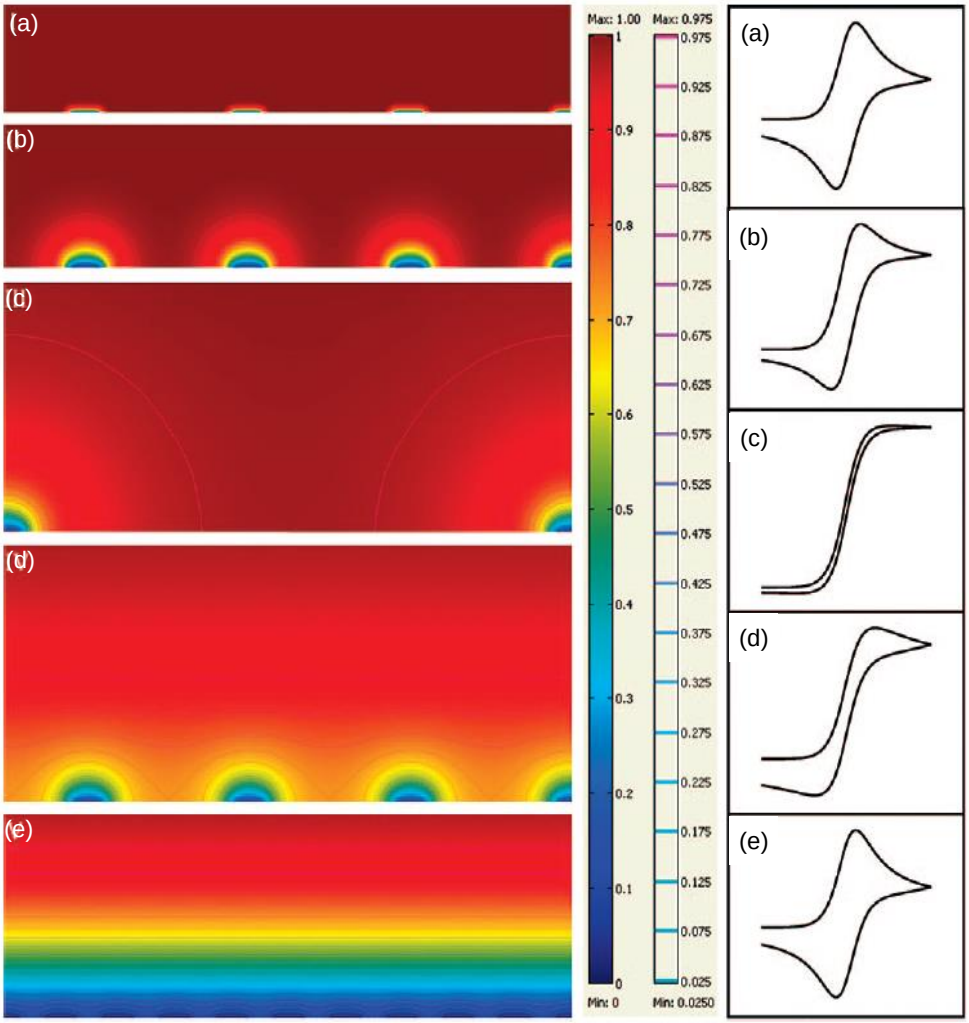

Figure 1.6. Simulated concentration profiles with isoconcentration contour lines over a microelectrode array representing the five main categories of diffusion modes: (a) planar diffusion layers on individual microdisk; (b) mixed diffusion layers on individual microdisk; diffusion mode between planar and hemispherical diffusion; (c) hemispherical diffusion layers on individual microdisk; (d) mixed diffusion layers; diffusion mode of partial overlapping of adjacent diffusion layers; (e) planar diffusion layer over the entire microelectrode array; diffusion mode of complete overlapping of individual diffusion layers. In the scale bar next to the figure, the red color represents the bulk concentration and the blue color represents zero concentration. The second scale bar represents a relative concentration scale for the contour lines. Reprinted (adapted) with permission from ref 50. Copyright (2009) American Chemical Society.

It is important to understand the correlation between diffusion profiles and its resulting cyclic voltammogram. This is because the advantageous characteristics of a microelectrode can be removed from an MEA sensor if

diffusion hemispheres overlap such that planar diffusion results during sensor operation, as in Category 5. Keeping an MEA operating within Category 3 and 4 profiles is ideal and will be studied in greater depth in chapter 5.

1.4.6. Microelectrode Array Fabrication

Microelectrodes have been traditionally fabricated using metals such as gold, silver and platinum as the active layer as conductive materials are required for electron transfer to occur.[51–55] These microelectrode arrays benefit from all the advantages of a microelectrode as mentioned in the previous section, but are able to output higher current. This occurs because the multiple microelectrodes on the surface act in concert with each other to create an overall larger current.

MEA fabrication can come in several configurations. Firstly there are vertically aligned MEAs where the active microelectrodes protrude out from the collector substrate.[45,56] Secondly, there are inlaid MEAs where the active layer is level with the substrate surface.[37] Lastly there are recessed MEAs where the active materials lies indented into the insulating layer.[50] It is this last conformation of MEAs that this thesis will focus on.

Typical recessed MEA fabrication techniques as shown in Figure 1.7 include a series of lithography sacrificial layers and wet chemical etch methods. First, an active layer such as platinum, gold, silver etc. is selected and deposited onto a substrate. Next a photoresist layer is spincoated onto the metal layer and photolithography is used to pattern the electrode shape onto the substrate.

The photoresist is washed away and reactive ion etching is employed to remove the unwanted metal areas. The residual photoresist is then washed away and a passivating layer is deposited onto the patterned metal electrodes. Photoresist is spin coated onto the passivating layer and a photomask is aligned so that the resist that is removed exposes the passivating layer that is covering the active electrodes. Once the resist is washed away, etching is used to remove the passivating layer covering the active metal electrodes and the final step involves washing away all the photoresist.

As can be seen, the etch steps in a conventional MEA fabrication process are not amenable to be used with thin layer active materials such as graphene. Controlling the etch times to remove the passivating layer without also removing the graphene layer is currently too difficult to control. With metal based MEAs, longer etch times can be used to completely remove the unwanted passivating layer, knowing that the metal layer is thick enough to not be completely removed. This is not so with single layer or few nanometer thick graphene active layers as sometimes even a few seconds in an reactive ion etch environment can completely remove the graphene material.

It is for this reason that there has not been much study graphene based MEAs. In order to study graphene microelectrode arrays (GMEA), a new method of MEA fabrication is required. This can be done through a process whereby the graphene active layer is protected by another material that is later on easily removed without having to resort to etching processes. This will be discussed in Chapter 3.

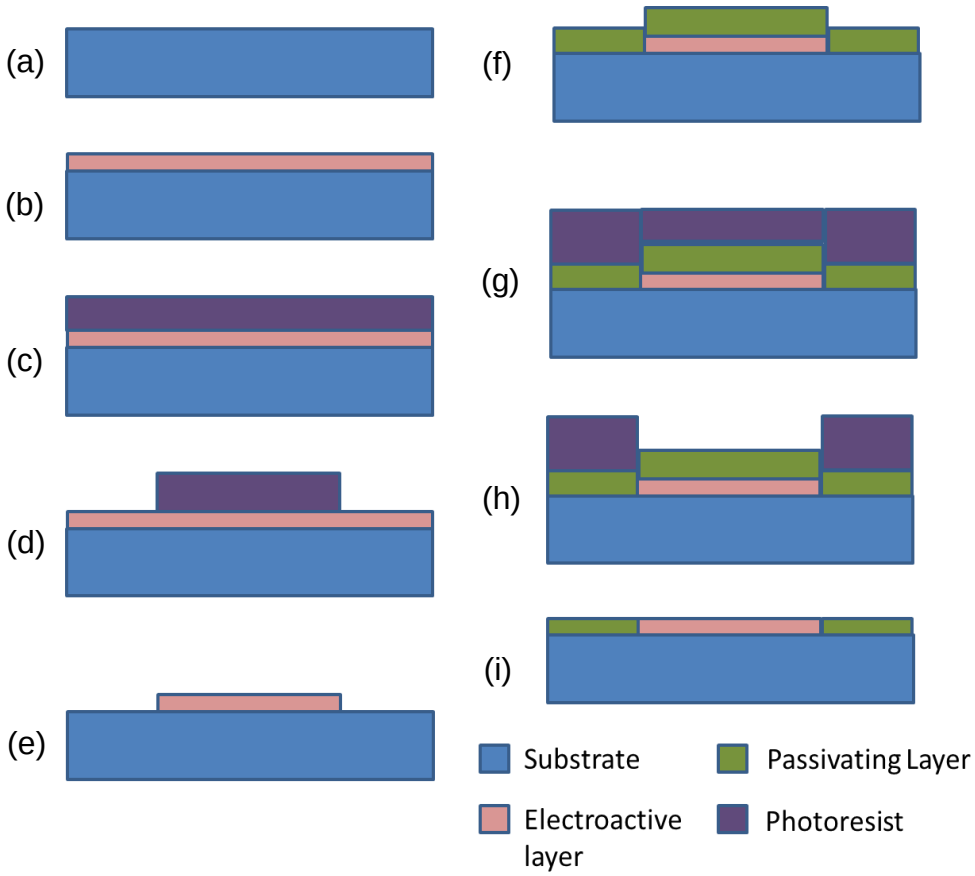

Figure 1.7. MEA fabrication process. (a) Substrate is cleaned (b) The electroactive layer is deposited onto the substrate. (c) Photoresist is spin coated onto the electroactive layer. (d) Photolithography is used (e) Removal of the unwanted electro active areas is done by chemical or wet etching. (f) A passivating layer is deposited onto the patterned electro active layer. (g) Photoresist is spin coated on top of the passivating layer. (h) Photolithography is used to expose the passivating layer that is covering the electroactive areas. (i) Etching is used to remove the passivating layer exposing the electro active layer and removal of residual photoresist.

1.4.7. MEA Fabrication using Nanoimprint lithography (NIL)

NIL was the main method used to fabricate graphene based MEAs. NIL is a surface patterning technique capable of fabricating nanometer scale patterns on various substrates[25] using thermal or UV curable photoresists at elevated temperatures and pressures. At temperatures past the glass transition temperature (T_g), the resist layer flows into the patterns of the mold. Once

allowed to cure using UV light or lowering the temperature below Tg levels, a negative pattern of the Si mold is left on the surface (Figure 1.8).[26] Pattern resolutions have been fabricated down to 5 nm,[27] far exceeding pattern resolutions found in conventional lithography techniques that are limited by the wavelength of visible light (approx. 200nm).

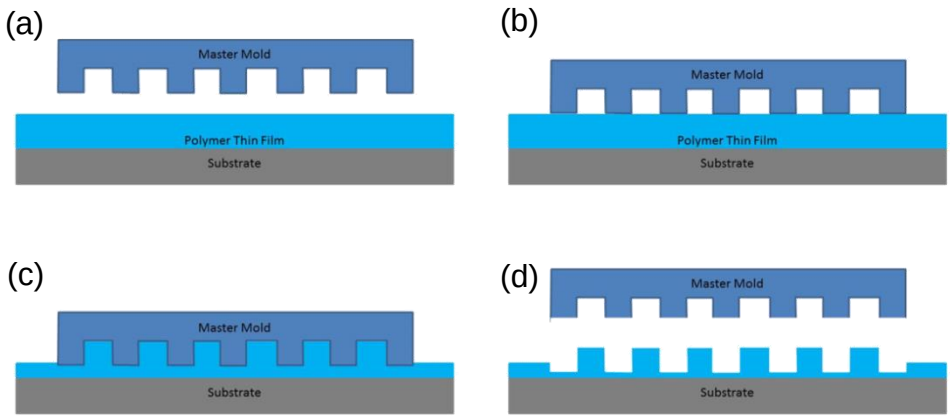

Figure 1.8. Typical NIL process (a) Resist is spin coated onto a substrate. (b) Mold comes into contact with resist layer under pressure and temperature. (c) Once T_g of resist is reached it starts to flow and fill in the cavities of the mold. (c) Temperature is reduced and mold is reduced leaving behind a negative patterning of the mold

NIL has been largely used in the area of creating functional surfaces. Studying surface structures in nature that possess characteristics based on surface structuring alone. Such as, colorization of the butterfly wing,[28] super hydrophobic self-cleaning properties of the lotus leaf[29] and hydrophobic water pinning effect found in rose petals (Figure 1.9).[30] Using NIL, the surface structures of these biological systems can be replicated in the lab resulting in materials that possess the same characteristics as the mimicked biological system.

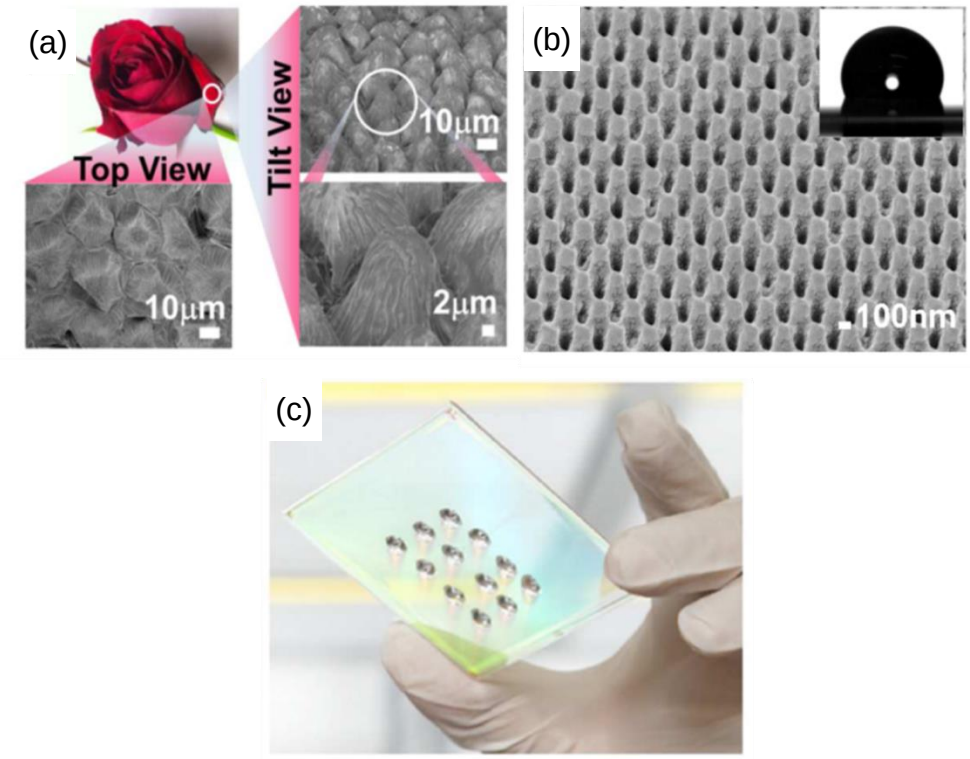

Figure 1.9 (a) Rose petal and SEM imaging of petal surface. (b) NIL imprinted surface of poly carbonate (PC) substrate with a similar structure as the rose petal surface. (c) Pinning of water droplets on the surface of patterned PC. Reproduced with permission from ref 30.

A secondary use of NIL is to utilize the process to create sacrificial layers for etching. This process is similar to masking techniques used with photolithography, except that NIL allows the resolutions of the etch patterns to go down to the 10 nm regime.

NIL is a method that can create periodic surface structures across a substrate and therefore is an excellent method to fabricate MEAs which require periodic microelectrode holes across a conducting substrate. Furthermore, NIL can create these structures on a large scale allowing for a relatively higher throughput fabrication process for MEAs.

1.4.8. MEA Applications

Applications for microelectrode arrays have found their uses in environmental, neuroscience, drug discovery and biological detection research areas.[57–59] MEAs lend themselves well to these fields due to the small nature of the environments the target analytes reside in, such as neuron cells, ion channels or even molecular level drugs and bioanalytes, which MEAs are more sensitive to due to their characteristic higher signal to noise ratios. Documented MEA usage include tracking neuron propagation,[60] acting as a brain-machine interface to restore motor function,[61] detection of bio analytes,[43,62–64] bacteria detection,[65] gas sensing,[66] and DNA detection[67,68]. As can be seen, the electrochemical properties that an MEA possesses can be used over a wide area of research fields.

1.4.9. rGO as an active material in MEA

As discussed previously, traditional active materials have been mainly metals such as platinum, gold and silver. However with the discovery of an ever increasing number of electrically conductive materials, the electroactive layer of a sensor has expanded to include other materials such as indium tin oxide (ITO), fluorine tin oxide (FTO), glassy carbon etc.[62,69–72] Naturally, since its discovery as being an excellent electrical conductor, graphene has been used as an electrode active layer and has been extensively reported in many different configurations, from gated field effect transistors (FET)s to changing the active layer of sensors to improve performance.[73–77] Graphene is a suitable electroactive layer for several key reasons. Graphene has a wide

electrochemical window, is chemically stable, is relative inert, is highly tunable to be selective to specific analytes, contains no impurities as compared to metal based active layers, flexible and is low cost.[34,78–80]

One area that graphene has not been investigated in is the MEA format. As previously mentioned, GMEA fabrication has not been trialed due to difficulties in controlling etch times for thin layer active materials. Traditionally when metals are used as the active layers, the layers are thick enough to compensate for etch methods removing any protective layer but also exposing the metal active layer. However, when one is dealing with nanometer thick graphene based active layers, controlling the etch time to remove the insulating layer without also removing the graphene active layer becomes a nearly impossible technical issue. However, a method was developed to protect the graphene active layer by using an imprintable resist layer of poly vinyl alcohol (PVA). This method is not restricted to atomically thick graphene but also to few nm thick materials such as rGO. rGO is an attractive derivative of graphene due to its applicability to solution processing, and its high electron mobility and oxygen groups that can act as chemical functionalization sites or in some cases active centers for faradaic currents to occur.

Using this technique, MEAs were fabricated under conditions that were relatively mild and therefore could be used with plastics substrates, creating a technique to fabricate flexible plastic substrate sensors which will be discussed in greater detail in Chapter 4.

1.5. Objectives and work scope

To realize graphene based devices, methods must be developed to enable selective control over the placement of graphene and its derivatives on a large scale. The intrinsic graphene characteristics of electrical conductivity, flexibility and bio compatibility lends itself well to be used in sensing applications.

In view of this, graphene manipulation on a large scale was explored through the use of nanoimprint lithography (NIL) in chapter 3. NIL was amenable to templating substrates over a large area in various shapes and sizes.

Graphene and reduced graphene oxide (rGO) was incorporated as an active layer into a microelectrode array (MEA) sensor. A novel self-aligning method was developed and the fabricated rGO MEA biosensors performance was investigated in chapter 4. Sensitivities towards bioanalytes such as dopamine and hydrogen peroxide were studied as well as the biosensors ability to be incorporated into a microfluidic system and the devices flexibility was also investigated.

MEA design requires interelectrode spacings of the microelectrodes to be spaced far enough from each other so that the diffusion hemispheres do not overlap. Chapter 5 investigates the optimal interelectrode spacing for an rGO MEA using rGO MEAs with varying interelectrode distances and cyclic voltammetry characterization to determine the distance at which the device would operate in a microelectrode regime.

The active layer material plays an important part in the performance of an electrochemical sensor. Ideally an active layer should be able to be deposited onto an electrode in a uniform manner so that its performance is consistent across large area electrodes. Leveraging on the self-assembling nature of the peptide hydrogel N-fluorenylmethoxycarbonyldiphenylalanine (Fmoc-FF) to form a 3D scaffold, a reduced graphene oxide/Fmoc-FF nanocomposite (rGO NC) was synthesized to determine pH and concentration parameters so that the rGO NC could coat a large area electrode substrate uniformly. Characterization of the rGO NC sensitivities was conducted and compared with an rGO layer without the self-assembling peptide scaffold. The rGO NC's use in bioapplications was investigated through the detection of serotonin in the presence of dopamine and ascorbic acid interferents. Lastly, the rGO NC layer was fabricated into an MEA configuration.

The findings in this thesis are important to furthering the development of new methods to shape graphene materials and fabricate graphene based MEA sensors. The work showed graphene as an excellent active layer for MEA devices and is especially amenable to flexible biosensor platforms. Elucidating the optimal interelectrode spacing to microelectrode radius ratio serves as an important guide rule for future rGO based MEA devices. Lastly, developing an rGO NC active layer using self-assembling peptides that can be uniformly coated over a large area with increased sensitivities can be used for future biosensing devices.

1.6. References

1. Novoselov, K. S. Electric Field Effect in Atomically Thin Carbon Films. *Science* **306,** 666–669 (2004).

2. Hua-Qiang, W., Chang-Yang, L., Hong-Ming, L. & He, Q. Graphene applications in electronic and optoelectronic devices and circuits. *Chin. Phys. B* **22,** 098106 (2013).

3. Jiang, J.-W., Wang, J.-S. & Li, B. Young's modulus of graphene: A molecular dynamics study. *Phys. Rev. B* **80,** 113405 (2009).

4. Lee, C., Wei, X., Kysar, J. W. & Hone, J. Measurement of the elastic properties and intrinsic strength of monolayer graphene. *Science* **321,** 385–388 (2008).

5. Morozov, S. V., Novoselov, K. S., Katsnelson, M. I., Schedin, F., Elias, D. C., Jaszczak, J. A. & Geim, A. K. Giant Intrinsic Carrier Mobilities in Graphene and Its Bilayer. *Phys. Rev. Lett.* **100,** 016602 (2008).

6. Chen, S., Wu, Q., Mishra, C., Kang, J., Zhang, H., Cho, K., Cai, W., Balandin, A. A. & Ruoff, R. S. Thermal conductivity of isotopically modified graphene. *Nat. Mater.* **11,** 203–207 (2012).

7. Mayavan, S., Siva, T. & Sathiyanarayanan, S. Graphene ink as a corrosion inhibiting blanket for iron in an aggressive chloride environment. *RSC Adv.* **3,** 24868–24871 (2013).

8. Cong, H.-P., Ren, X.-C., Wang, P. & Yu, S.-H. Flexible graphene–polyaniline composite paper for high-performance supercapacitor. *Energy Environ. Sci.* **6,** 1185–1191 (2013).

9. Nair, R. R., Blake, P., Grigorenko, A. N., Novoselov, K. S., Booth, T. J., Stauber, T., Peres, N. M. R. & Geim, A. K. Fine Structure Constant Defines Visual Transparency of Graphene. *Science* **320,** 1308–1308 (2008).

10. Song, J., Wang, X. & Chang, C.-T. Preparation and Characterization of Graphene Oxide. *J. Nanomater.* **2014,** 1-6 (2014).

11. Li, Z. J., Yang, B. C., Zhang, S. R. & Zhao, C. M. Graphene oxide with improved electrical conductivity for supercapacitor electrodes. *Appl. Surf. Sci.* **258,** 3726–3731 (2012).

12. Marcano, D. C., Kosynkin, D. V., Berlin, J. M., Sinitskii, A., Sun, Z., Slesarev, A., Alemany, L. B., Lu, W. & Tour, J. M. Improved Synthesis of Graphene Oxide. *ACS Nano* **4,** 4806–4814 (2010).

13. Yu, Q., Jauregui, L. A., Wu, W., Colby, R., Tian, J., Su, Z., Cao, H., Liu, Z., Pandey, D., Wei, D., Chung, T. F., Peng, P., Guisinger, N. P., Stach, E. A., Bao, J., Pei, S.-S. & Chen, Y. P. Control and characterization of individual grains and grain boundaries in graphene grown by chemical vapour deposition. *Nat. Mater.* **10,** 443–449 (2011).

14. He, H., Klinowski, J., Forster, M. & Lerf, A. A new structural model for graphite oxide. *Chem. Phys. Lett.* **287,** 53–56 (1998).

15. Feng, H., Cheng, R., Zhao, X., Duan, X. & Li, J. A low-temperature method to produce highly reduced graphene oxide. *Nat. Commun.* **4,** 1539 (2013).

16. Mulyana, Y., Uenuma, M., Ishikawa, Y. & Uraoka, Y. Reversible Oxidation of Graphene Through Ultraviolet/Ozone Treatment and Its Nonthermal Reduction through Ultraviolet Irradiation. *J. Phys. Chem. C* **118,** 27372–27381 (2014).

17. Chen, W., Yan, L. & Bangal, P. R. Preparation of graphene by the rapid and mild thermal reduction of graphene oxide induced by microwaves. *Carbon* **48,** 1146–1152 (2010).

18. Yang, D., Velamakanni, A., Bozoklu, G., Park, S., Stoller, M., Piner, R. D., Stankovich, S., Jung, I., Field, D. A., Ventrice Jr., C. A. & Ruoff, R. S. Chemical analysis of graphene oxide films after heat and chemical treatments by X-ray photoelectron and Micro-Raman spectroscopy. *Carbon* **47,** 145–152 (2009).

19. Gao, X., Jang, J. & Nagase, S. Hydrazine and Thermal Reduction of Graphene Oxide: Reaction Mechanisms, Product Structures, and Reaction Design. *J. Phys. Chem. C* **114,** 832–842 (2009).

20. Shin, H.-J., Kim, K. K., Benayad, A., Yoon, S.-M., Park, H. K., Jung, I.-S., Jin, M. H., Jeong, H.-K., Kim, J. M., Choi, J.-Y. & Lee, Y. H. Efficient Reduction of Graphite Oxide by Sodium Borohydride and Its Effect on Electrical Conductance. *Adv. Funct. Mater.* **19,** 1987–1992 (2009).

21. Shao, Y., Wang, J., Engelhard, M., Wang, C. & Lin, Y. Facile and controllable electrochemical reduction of graphene oxide and its applications. *J. Mater. Chem.* **20,** 743–748 (2010).

22. Toh, S. Y., Loh, K. S., Kamarudin, S. K. & Daud, W. R. W. Graphene production via electrochemical reduction of graphene oxide: Synthesis and characterisation. *Chem. Eng. J.* **251,** 422–434 (2014).

23. Loryuenyong, V., Totepvimarn, K., Eimburanapravat, P., Boonchompoo, W. & Buasri, A. Preparation and Characterization of Reduced Graphene Oxide Sheets via Water-Based Exfoliation and Reduction Methods. *Adv. Mater. Sci. Eng.* **2013,** e923403 (2013).

24. Gómez-Navarro, C., Weitz, R. T., Bittner, A. M., Scolari, M., Mews, A., Burghard, M. & Kern, K. Electronic Transport Properties of Individual Chemically Reduced Graphene Oxide Sheets. *Nano Lett.* **7,** 3499–3503 (2007).

25. Chou, S. Y., Krauss, P. R. & Renstrom, P. J. Nanoimprint lithography. *J. Vac. Sci. Technol. B* **14,** 4129–4133 (1996).

26. Guo, L. J. Nanoimprint Lithography: Methods and Material Requirements. *Adv. Mater.* **19,** 495–513 (2007).

27. Michael D. Austin, H. G. Fabrication of 5 nm linewidth and 14 nm pitch features by nanoimprint lithography. *Appl. Phys. Lett.* **84,** 5299–5301 (2004).

28. Kustandi, T. S., Low, H. Y., Teng, J. H., Rodriguez, I. & Yin, R. Mimicking Domino-Like Photonic Nanostructures on Butterfly Wings. *Small* **5,** 574–578 (2009).

29. Saison, T., Peroz, C., Chauveau, V., Berthier, S., Sondergard, E. & Arribart, H. Replication of butterfly wing and natural lotus leaf structures by nanoimprint on silica sol–gel films. *Bioinspir. Biomim.* **3,** 046004 (2008).

30. Law, J. B. K., Ng, A. M. H., He, A. Y. & Low, H. Y. Bioinspired Ultrahigh Water Pinning Nanostructures. *Langmuir* **30,** 325–331 (2013).

31. Ciobanu, M., Wilburn, J. P., Krim, M. L. & Cliffel, D. E. in *Handb. Electrochem.* (ed. Zoski, C. G.) 3–II (Elsevier, 2007). at <http://www.sciencedirect.com/science/article/pii/B978044451958050002 1>

32. Bakker, E. & Qin, Y. Electrochemical Sensors. *Anal. Chem.* **78,** 3965–3984 (2006).

33. Chen, S. in *Handb. Electrochem.* (ed. Zoski, C. G.) 33–III (Elsevier, 2007).

34. Brownson, D. A. C. *Handbook of Graphene Electrochemistry*. (Springer, 2014).

35. Denuault, G., Sosna, M. & Williams, K.-J. in *Handb. Electrochem.* (ed. Zoski, C. G.) 431–469 (Elsevier, 2007).

36. Aoki, K. Theory of ultramicroelectrodes. *Electroanalysis* **5,** 627–639 (1993).

37. Bond, A. M., Oldham, K. B. & Zoski, C. G. Theory of electrochemical processes at an inlaid disc microelectrode under steady-state conditions. *J. Electroanal. Chem. Interfacial Electrochem.* **245,** 71–104 (1988).

38. Nirmaier, H.-P. & Henze, G. Characteristic behavior of macro-, semimicro- and microelectrodes in voltammetric and chronoamperometric measurements. *Electroanalysis* **9,** 619–624 (1997).

39. Bai, J., Wang, X., Meng, Y., Zhang, H.-M. & Qu, L. Fabrication of graphene coated carbon fiber microelectrode for highly sensitive detection application. *Anal. Sci. Int. J. Jpn. Soc. Anal. Chem.* **30,** 903–909 (2014).

40. Deng, M., Yang, X., Silke, M., Qiu, W., Xu, M., Borghs, G. & Chen, H. Electrochemical deposition of polypyrrole/graphene oxide composite on

microelectrodes towards tuning the electrochemical properties of neural probes. *Sens. Actuators B Chem.* **158,** 176–184 (2011).

41. Montenegro, M. I., Montenegro, I., Queirós, M. A. & Daschbach, J. L. *Microelectrodes: Theory and Applications: Theory and Applications*. (Kluwer Academic Publishers, 1991).

42. Huang, X.-J., O'Mahony, A. M. & Compton, R. G. Microelectrode Arrays for Electrochemistry: Approaches to Fabrication. *Small* **5,** 776–788 (2009).

43. Bhavik Anil Patel, C. C. L. A planar microelectrode array for simultaneous detection of electrically evoked dopamine release from distinct locations of a single isolated neuron. *The Analyst* (2013). doi:10.1039/c3an36770c

44. Chen, Y.-C., Hsu, H.-L., Lee, Y.-T., Su, H.-C., Yen, S.-J., Chen, C.-H., Hsu, W.-L., Yew, T.-R., Yeh, S.-R., Yao, D.-J., Chang, Y.-C. & Chen, H. An active, flexible carbon nanotube microelectrode array for recording electrocorticograms. *J. Neural Eng.* **8,** 034001 (2011).

45. Park, J., Kwon, S., Jun, S. I., Mcknight, T. E., Melechko, A. V., Simpson, M. L., Dhindsa, M., Heikenfeld, J. & Rack, P. D. Active-Matrix Microelectrode Arrays Integrated With Vertically Aligned Carbon Nanofibers. *IEEE Electron Device Lett.* **30,** 254–257 (2009).

46. Li, F., Xue, M., Ma, X., Zhang, M. & Cao, T. Facile patterning of reduced graphene oxide film into microelectrode array for highly sensitive sensing. *Anal. Chem.* **83,** 6426–6430 (2011).

47. Yuko Ueno, K. F. Graphene-modified Interdigitated Array Electrode: Fabrication, Characterization, and Electrochemical Immunoassay Application. *Anal. Sci. Int. J. Jpn. Soc. Anal. Chem.* **29,** 55–60 (2013).

48. Hsiao, Y.-S., Kuo, C.-W. & Chen, P. Multifunctional Graphene–PEDOT Microelectrodes for On-Chip Manipulation of Human Mesenchymal Stem Cells. *Adv. Funct. Mater.* n/a–n/a (2013). doi:10.1002/adfm.201203631

49. Tomcik, P. Microelectrode Arrays with Overlapped Diffusion Layers as Electroanalytical Detectors: Theory and Basic Applications. *Sensors* **13,** 13659–13684 (2013).

50. Guo, J. & Lindner, E. Cyclic Voltammograms at Coplanar and Shallow Recessed Microdisk Electrode Arrays: Guidelines for Design and Experiment. *Anal. Chem.* **81,** 130–138 (2009).

51. White, H. S., Kittlesen, G. P. & Wrighton, M. S. Chemical derivatization of an array of three gold microelectrodes with polypyrrole: fabrication of a molecule-based transistor. *J. Am. Chem. Soc.* **106,** 5375–5377 (1984).

52. Ahn, B. Y., Duoss, E. B., Motala, M. J., Guo, X., Park, S.-I., Xiong, Y., Yoon, J., Nuzzo, R. G., Rogers, J. A. & Lewis, J. A. Omnidirectional Printing of Flexible, Stretchable, and Spanning Silver Microelectrodes. *Science* **323,** 1590–1593 (2009).

53. Wassum, K. M., Tolosa, V. M., Wang, J., Walker, E., Monbouquette, H. G. & Maidment, N. T. Silicon Wafer-Based Platinum Microelectrode Array Biosensor for Near Real-Time Measurement of Glutamate in Vivo. *Sensors* **8,** 5023–5036 (2008).

54. Thormann, W., Van den Bosch, P. & Bond, A. M. Voltammetry at linear gold and platinum microelectrode arrays produced by lithographic techniques. *Anal. Chem.* **57,** 2764–2770 (1985).

55. Uhlig, A., Schnakemberg, U. & Hintsche, R. Highly sensitive heavy metal analysis on platinum- and gold-ultramicroelectrode arrays. *Electroanalysis* **9,** 125–129 (1997).

56. Castro Smirnov, J. R., Jover, E., Amade, R., Gabriel, G., Villa, R. & Bertran, E. Vertically aligned carbon nanotubes for microelectrode arrays applications. *J. Nanosci. Nanotechnol.* **12,** 6941–6947 (2012).

57. Thomas Jr., C. A., Springer, P. A., Loeb, G. E., Berwald-Netter, Y. & Okun, L. M. A miniature microelectrode array to monitor the bioelectric activity of cultured cells. *Exp. Cell Res.* **74,** 61–66 (1972).

58. Rizzo, J. F., Wyatt, J., Loewenstein, J., Kelly, S. & Shire, D. Perceptual Efficacy of Electrical Stimulation of Human Retina with a Microelectrode Array during Short-Term Surgical Trials. *Invest. Ophthalmol. Vis. Sci.* **44,** 5362–5369 (2003).

59. Nordhausen, C. T., Maynard, E. M. & Normann, R. A. Single unit recording capabilities of a 100 microelectrode array. *Brain Res.* **726,** 129–140 (1996).

60. Bakkum, D. J., Frey, U., Radivojevic, M., Russell, T. L., Müller, J., Fiscella, M., Takahashi, H. & Hierlemann, A. Tracking axonal action potential propagation on a high-density microelectrode array across hundreds of sites. *Nat. Commun.* **4,** (2013).

61. Jackson, A. & Zimmermann, J. B. Neural interfaces for the brain and spinal cord—restoring motor function. *Nat. Rev. Neurol.* **8,** 690–699 (2012).

62. Babaei, A., Babazadeh, M. & Momeni, H. R. A Sensor for Simultaneous Determination of Dopamine and Morphine in Biological Samples Using a Multi-Walled Carbon Nanotube/Chitosan Composite Modified Glassy Carbon Electrode. *Int J Electrochem Sci* **6,** 1382–1395 (2011).

63. Alwarappan, S., Liu, C., Kumar, A. & Li, C.-Z. Enzyme-Doped Graphene Nanosheets for Enhanced Glucose Biosensing. *J. Phys. Chem. C* **114,** 12920–12924 (2010).

64. Colin-Orozco, E., Corona-Avendano, S., Ramirez-Silva, M. T., Romero-Romo, M. & Palomar-Pardave, M. On the Electrochemical Oxidation of Dopamine, Ascorbic Acid and Uric Acid onto a Bare Carbon Paste Electrode from a 0.1 M NaCl Aqueous Solution at pH 7. *Int. J. Electrochem. Sci.* **7,** 6097–6105 (2012).

65. Radke, S. M. & Alocilja, E. C. A high density microelectrode array biosensor for detection of E. coli O157:H7. *Biosens. Bioelectron.* **20,** 1662–1667 (2005).

66. Huang, X.-J., Aldous, L., O'Mahony, A. M., del Campo, F. J. & Compton, R. G. Toward Membrane-Free Amperometric Gas Sensors: A Microelectrode Array Approach. *Anal. Chem.* **82,** 5238–5245 (2010).

67. Choi, Y.-S. & Park, D.-H. Electrochemical gene detection using multielectrode array DNA chip. *J.-KOREAN Phys. Soc.* **44,** 1556–1559 (2004).

68. Pacios, M., Yilmaz, N., Martín-Fernández, I., Villa, R., Godignon, P., Del Valle, M., Bartrolí, J. & Esplandiu, M. J. A simple approach for DNA detection on carbon nanotube microelectrode arrays. *Sens. Actuators B Chem.* **162,** 120–127 (2012).

69. Yang, J., Strickler, J. R. & Gunasekaran, S. Indium tin oxide-coated glass modified with reduced graphene oxide sheets and gold nanoparticles as disposable working electrodes for dopamine sensing in meat samples. *Nanoscale* **4,** 4594 (2012).

70. Blau, A. Cell adhesion promotion strategies for signal transduction enhancement in microelectrode array in vitro electrophysiology: An introductory overview and critical discussion. *Curr. Opin. Colloid Interface Sci.* **18,** 481–492 (2013).

71. McCreedy, T. & Fielden, P. R. Amperometric detector for high-performance liquid chromatography, featuring a glassy carbon working electrode array in the wall-jet configuration. *Analyst* **120,** 2343–2346 (1995).

72. VanDersarl, J. J., Mercanzini, A. & Renaud, P. Integration of 2D and 3D Thin Film Glassy Carbon Electrode Arrays for Electrochemical Dopamine Sensing in Flexible Neuroelectronic Implants. *Adv. Funct. Mater.* **25,** 78–84 (2015).

73. Ohno, Y., Maehashi, K., Yamashiro, Y. & Matsumoto, K. Electrolyte-Gated Graphene Field-Effect Transistors for Detecting pH and Protein Adsorption. *Nano Lett.* **9,** 3318–3322 (2009).

74. Ang, P. K., Chen, W., Wee, A. T. S. & Loh, K. P. Solution-Gated Epitaxial Graphene as pH Sensor. *J. Am. Chem. Soc.* **130,** 14392–14393 (2008).

75. Al-Mashat, L., Shin, K., Kalantar-zadeh, K., Plessis, J. D., Han, S. H., Kojima, R. W., Kaner, R. B., Li, D., Gou, X., Ippolito, S. J. & Wlodarski, W. Graphene/Polyaniline Nanocomposite for Hydrogen Sensing. *J. Phys. Chem. C* **114,** 16168–16173 (2010).

76. Eswaraiah, V., Balasubramaniam, K. & Ramaprabhu, S. One-pot synthesis of conducting graphene–polymer composites and their strain sensing application. *Nanoscale* **4,** 1258–1262 (2012).

77. Lin, Q., Li, Y. & Yang, M. Tin oxide/graphene composite fabricated via a hydrothermal method for gas sensors working at room temperature. *Sens. Actuators B Chem.* **173,** 139–147 (2012).

78. Tang, L., Wang, Y., Li, Y., Feng, H., Lu, J. & Li, J. Preparation, Structure, and Electrochemical Properties of Reduced Graphene Sheet Films. *Adv. Funct. Mater.* **19,** 2782–2789 (2009).

79. Brownson, D. A. C. & Banks, C. E. Graphene electrochemistry: an overview of potential applications. *Analyst* **135,** 2768–2778 (2010).

80. Alwarappan, S., Erdem, A., Liu, C. & Li, C.-Z. Probing the Electrochemical Properties of Graphene Nanosheets for Biosensing Applications. *J. Phys. Chem. C* **113,** 8853–8857 (2009).

Chapter 2. Experimental techniques

This chapter covers the techniques used to characterize, fabricate and probe the properties of the graphene based devices.

2.1. Photolithography

Photolithography is used to create micro patterns on a substrate through the use of a photomask and light sensitive photoresists. The photomask is typically made from glass with a layer of chrome that defines the pattern. The chrome layer serves to block the UV light from contacting the photoresist while allowing the other desired areas to be exposed. Depending on the type of photoresist (negative or positive), the areas that are exposed to UV light will either wash away or remain on the substrate when it undergoes the photo developer process respectively. Figure 2.1 illustrates the process of a typical photolithography technique. Once the photo resist has been developed, leaving behind the patterned resist layer, etching techniques can be employed to pattern the underlying SiO_2 substrate. The photoresist can then be easily removed with a solvent such as acetone leaving behind a patterned substrate.

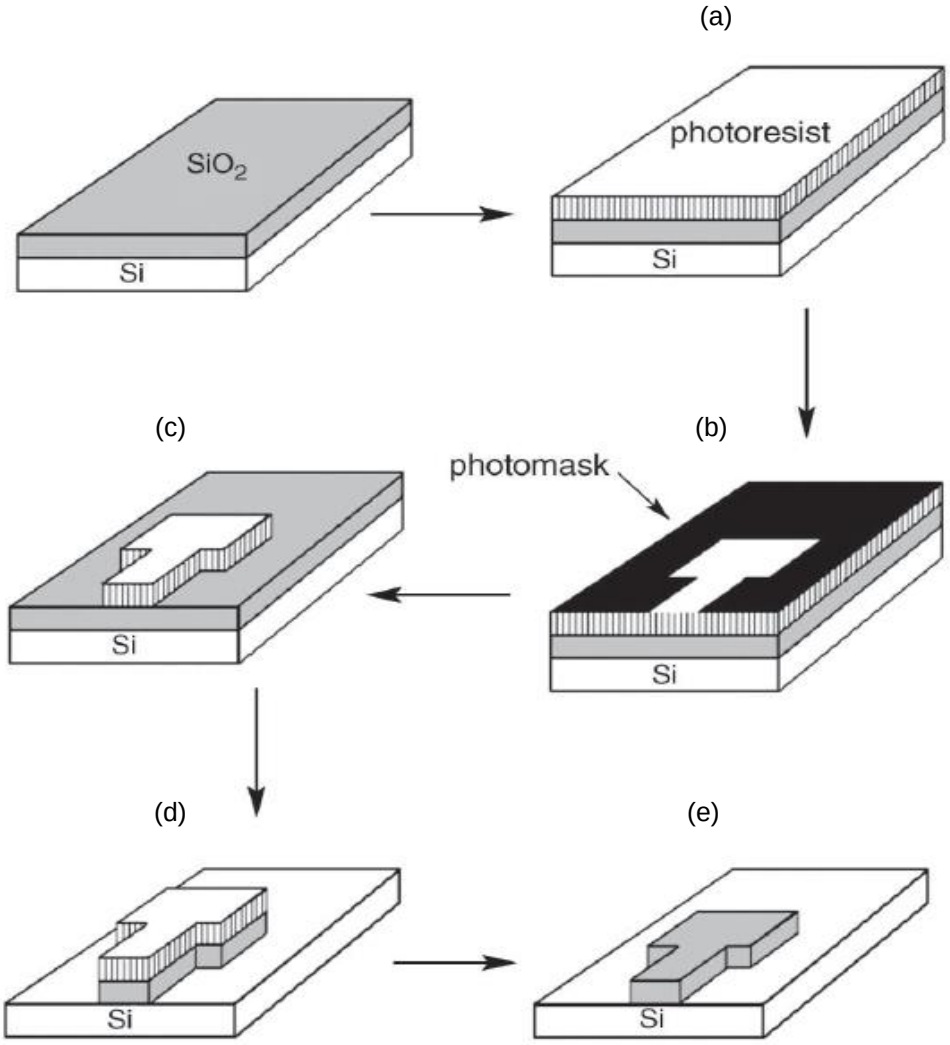

Figure 2.1. The process of photolithography used in microchip construction. A photoresist is spin-coated onto the oxidized surface of the silicon wafer (a) and a photomask is aligned on top (b). The unit is subjected to UV light, the photomask is removed, and the unpolymerized photoresist is rinsed away (c). Finally, the exposed, oxidized surface of the silicon wafer is etched away (d), and the remaining polymer is removed (e) to result in a silicon chip patterned in the negative image of the photomask. Reprinted (adapted) with permission from ref 1. Copyright (2005) American Chemical Society.

2.2. Atomic Force Microscopy (AFM)

AFM is a surface imaging technique that utilizes a sharp probe to investigate relative surface height differences on a sample. AFM has demonstrated sub

nanometre resolutions and has become an important tool in surface imaging (Figure 2.2).

AFM operates by the use of Van der Waals interactions. When the probe tip is brought close to the surface of the sample, the force exerted on the tip by the surface atoms either attract or repel the probe and a laser that is aligned directly onto the cantilever that the probe is attached to detects these small deflections. Using a photodiode and imaging software, the surface topography can be generated. AFM can be operated in its other useful mode, tapping mode AFM. Tapping mode AFM operates via a small piezoelectric element that oscillates the cantilever near its resonant frequency. As the oscillating tip is brought near the surface, the interacting forces dampen the amplitude of the oscillations. A feedback mechanism is used to monitor the change in amplitude and the AFM tip height is adjusted so that it continues oscillating at its resonant frequency. The method of tapping is preferred to the contact mode AFM as there is less likelihood of the tip or sample being damaged.

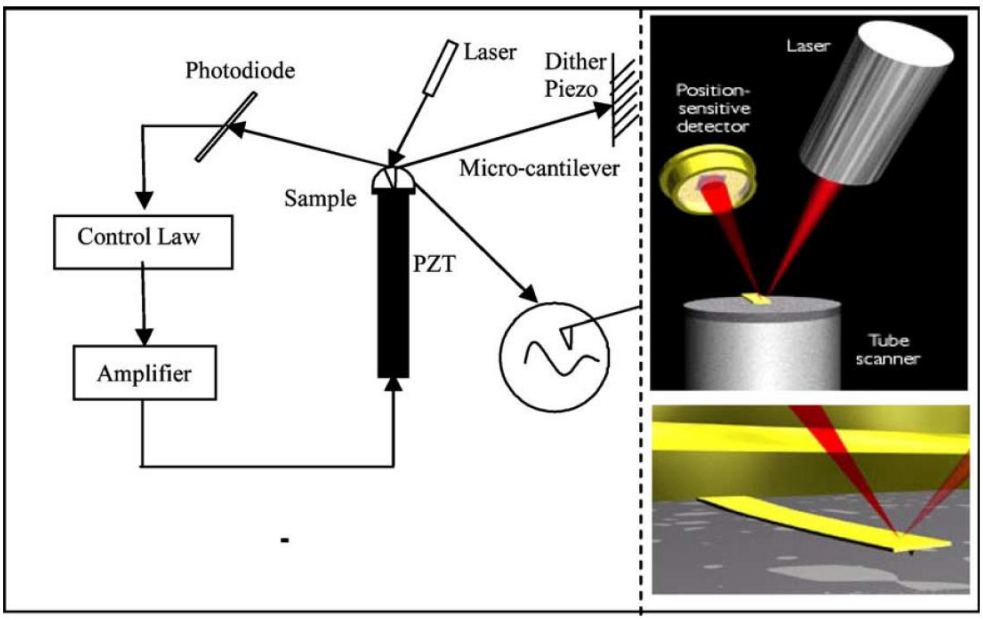

Figure 2.2. Schematic of basic AFM operation (left), real micro-cantilever and components (right). Reprinted with permission from ref 2.

AFM was particularly useful in measuring the dimensions of the rGO MEA hole openings and the thickness of the PMMA protective layer, and also the surface roughness of the self assembled GO nanocomposites as presented later in chapter 6.

2.3. Scanning Electron Microscopy (SEM)

SEM is a characterization technique that uses electrons to produce images of a sample. The most common mode of SEM imaging is done by an electron beam that is rastered across the sample surface. The electron beam has an energy ranging from 0.2 to 40 keV. This beam is then focused via two condenser lenses (Figure 2.3) after which it passes through deflector coils that deflect the beam in the x-y plane to allow it to scan over a sample area. The

atoms in the sample are excited by the electron beam and eject secondary electrons. These secondary electrons are collected and amplified. The position of the incident electron beam is then correlated with the intensity of the collected signal. Resolutions for SEM can go down to 1 nm and the scan speeds are relatively fast.

SEM sample preparation usually involves coating the sample with a thin layer of conductive metal. This is to prevent unwanted charging effects caused by the incident electron beam.

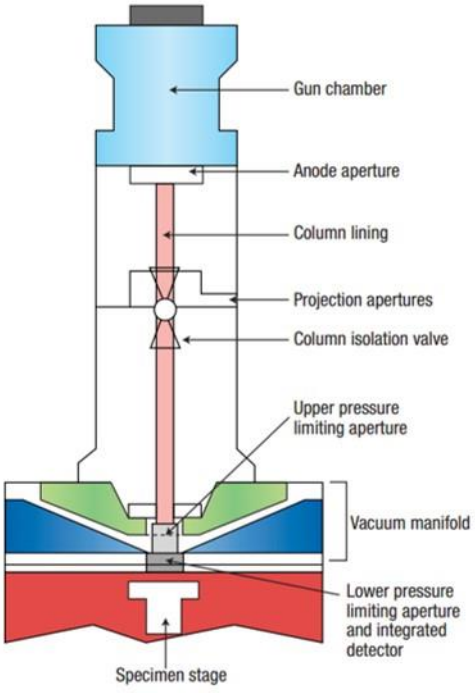

Figure 2.3. Global schematic of an SEM setup. Reprinted with permission from ref 3.

The use of SEM allowed relatively large area surveys of the GO samples. This was especially useful when observing the morphologies of the GO nanocomposites.

2.4. Raman Spectroscopy

Raman spectroscopy is a powerful technique that is able to identify unknown materials through output data of a materials unique Raman spectral fingerprint. Raman spectroscopy operates through the use of photons from an emitted laser that interact with the electron density of atoms or molecules. When a photon collides with a molecule it will undergo elastic or inelastic scattering. It is the inelastic scattering where a photon loses part of its energy to the material and causes atoms to vibrate that is considered as the Raman scattering process and named after its discoverer, C. V. Raman.

When energy is lost, it is considered as 'Stokes' and where energy is gained, it is considered as 'anti-stokes' (Figure 2.4). The change in energy is dependent on the frequency of the vibration of the molecule.

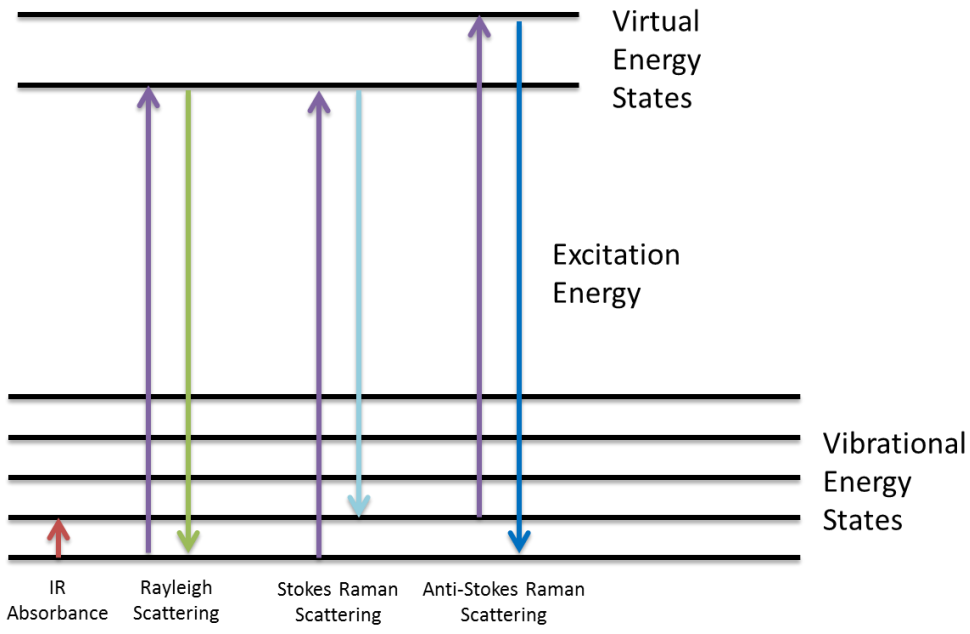

Figure 2.4. Energy Level Diagram

Raman spectroscopy has been used extensively in graphene characterization. It can differentiate between the graphene derivatives such as graphene oxide (GO), reduced graphene oxide (rGO) and pristine graphene. It can also give information on the whether the graphene is single layer or few layers.[4]

Primarily, pristine graphene has a peak that occurs at 1580 cm^{-1} called a G peak which is a result of the in-plane vibration of the sp^2 bonds, and another peak at 2700 cm^{-1} called a 2D peak which is a second order of the D peak.[5]

The Raman spectra of GO has a G peak at the 1600 cm^{-1} and a D peak at 1350 cm^{-1}. The rise of this D peak that is not found in pristine graphene is due to defects in the breathing mode of the sp^2 rings.[6] rGO can be distinguished from GO materials by the relative intensities of the D and G peak. As GO is reduced more sp^2 domains form and results in an increase of the intensity of the D peak. Higher D to G peak ratios indicate the presence of rGO.[7]

2.5. X-Ray photoelectron spectroscopy (XPS)

XPS is a versatile characterization technique used to determine the elemental composition of elements within a material. XPS works by irradiating a sample with low energy X-rays. If the transferred energy is large enough to excite the electrons they will be emitted as a photoelectron (Figure 2.5). Once detected the kinetic energy of the electrons is measured as the incident energy minus the binding energy. Since incident and kinetic energy is known, the binding energy can be calculated and therefore the parent element of the electron can be determined.

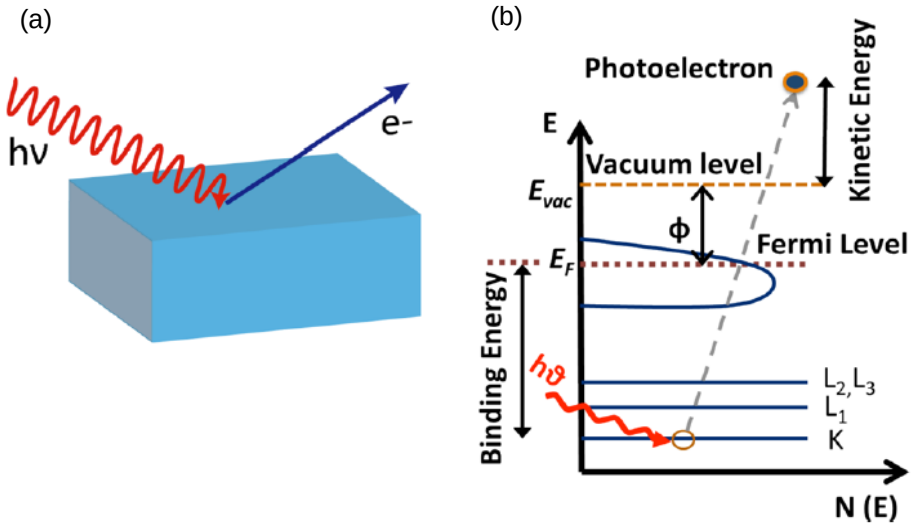

Figure 2.5. (a) Schematic diagram showing the photoelectric effect. Upon shining light of energy hν, photoelectrons are ejected from the material. (b) Energy level diagram of a metal showing electrons being photoejected from a core level to a state above the vacuum level with a finite kinetic energy. Reprinted (adapted) with permission from ref 8. . Copyright (2013) American Chemical Society.

XPS can also provide chemical bonding information. Depending on what elements the parent atom is bonded too, the energy levels of the ejected electrons will shift slightly giving information to what chemical compounds are present. XPS also gives quantitative information and is regularly used in determining the amount of oxygen to carbon ratios in graphene oxide and reduced graphene oxide samples.[6]

2.6. Differential Pulse Voltammetry (DPV)

DPV is a type of electrochemical measurement that involves the potentiostat outputting a series of regular voltage pulses (Figure 2.6). The current is sampled before the potential change and the difference is plotted against the

potential. Measuring the current in this fashion minimizes the effect of non-faradaic currents and allows for more sensitive target analyte-electrode reactions to be analyzed. This potential stepping technique allows the simultaneous detection of analytes of different oxidation points, and is a useful technique in the area of biosensing.

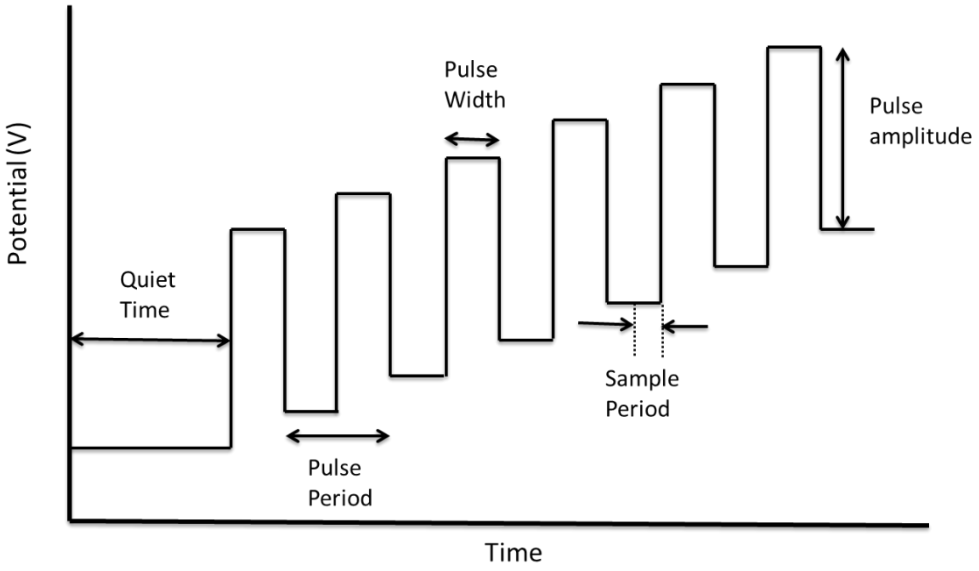

Figure 2.6. DPV Potential wave form profile.

2.7 Chronoamperommetry (CA)

One of the main electrochemical detection techniques used in this thesis is CA. CA is an excellent method for quantitative analysis. In CA, the current is measured as a response to a potential pulse of a set duration. At the beginning of the experiment, the working electrode is held at E_0 – usually at a point where no electrochemical processes occur. At t=0, the potential is stepped up to E_1 where it is the potential of interest (Figure 2.7).[33]

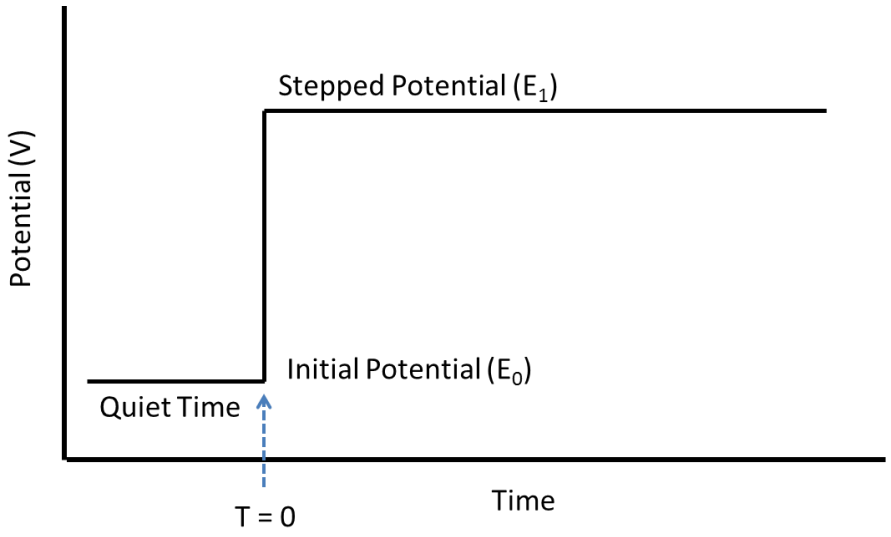

Figure 2.7. Sweep profile of CA.

It is important to note that at short times, the current detected by CA consists largely of a non-faradaic component due to the formation of the double layer capacitance. This non-faradaic current decays exponentially with a time constant that is determined by the uncompensated resistance (R_u) and the double layer capacitance (C_d). Therefore, experimental measurements should be taken at values greater than R_uC_d in order to minimize the effect of the double layer capacitance.[33]

Figure 2.8 shows a typical response to CA. This current line can be described by the Cottrell equation and is a function of $t^{-1/2}$.

$$i = \frac{nFAc\sqrt{D}}{\sqrt{\pi t}}$$

Where i is the current in A, n is the number of electrons participating in the reaction, F is faradays constant, A is the surface area of the electrode in cm^2, c is the initial concentration of the analyte in mol/cm^3, D is the diffusion coefficient of the analyte in cm^2/s and t is the time in seconds.

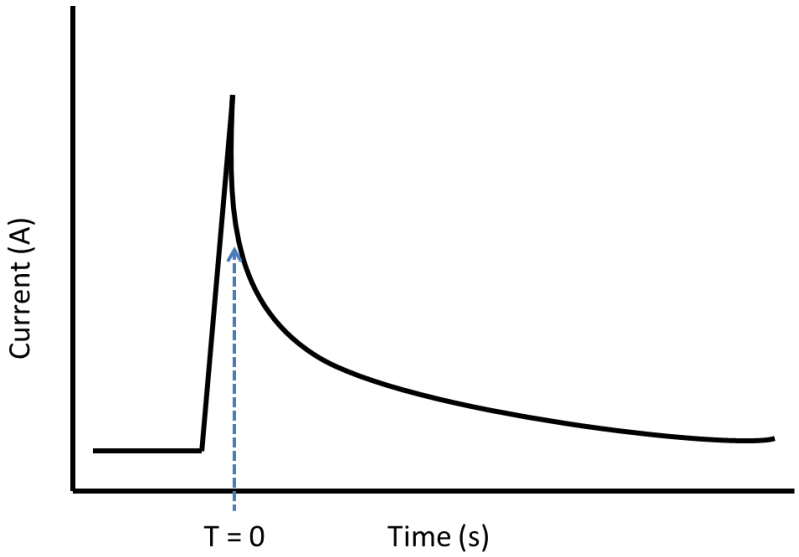

Figure 2.8. Resulting output from a typical CA experiment. The decaying of the current follows the Cottrell equation.

This decay occurs as the working electrode is stepped to a potential that allows for oxidation/reduction of the analyte at t=0, the region in which the immediate vicinity of the electrode converts the target analyte to its counter oxidation/reduction form. This creates a concentration gradient, where the analyte that is in the bulk concentration diffuses towards the electrode surface where electron transfer can occur. As the electrode remains at this potential, the concentration gradient extends further out from the electrode surface as more of the analyte is depleted. This region is called the diffusion layer.[34]

2.8 Cyclic Voltammetry (CV)

CV is a fast electrochemical tool that can provide qualitative and quantitative information. It is an electrochemical method that involves sweeping the electrode potential between two potential points at a controlled sweep rate, and

the corresponding current is recorded as a function of the potential sweep (Figure 2.9).

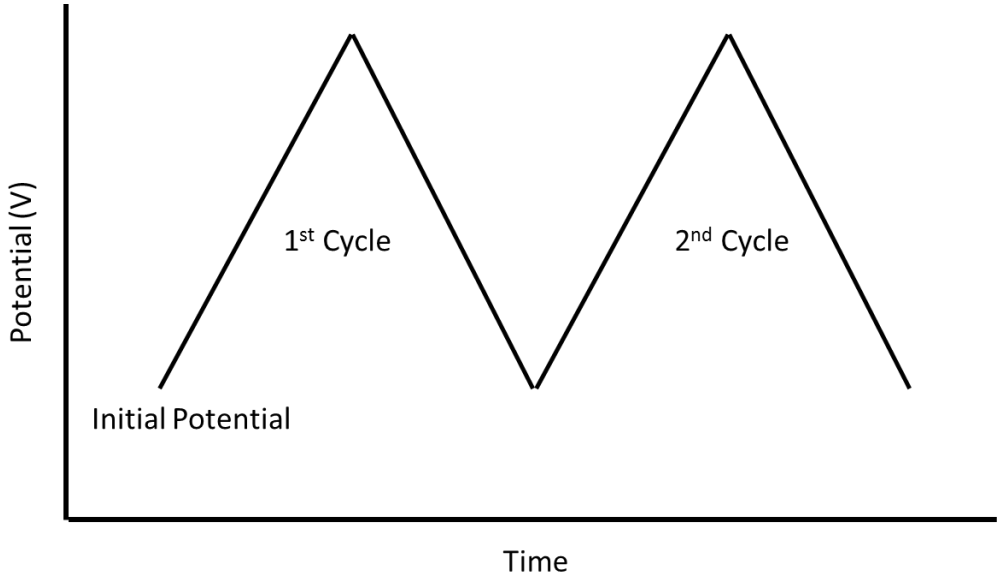

Figure 2.9. Sweep profile of CV

Figure 2.10 shows a typical CV voltammogram. This CV is peak shaped, showing a maxima/minima for reduction/oxidation reactions respectively. After the peak, it can be seen there is a depletion zone. This occurs when the voltage continues to sweep to higher potentials, the diffusion of the unreduced/unoxidized analyte towards the electrode surface is slower than the electron transfer rate and subsequently the current falls off.[33] This electrochemical method can be used to investigate the behavior of an electrode whether it is operating in the macro or microelectrode regime. Peak shaped CVs are indicative of macroelectrode behavior and sigmoidal shaped CVs are indicative of microelectrode behavior.

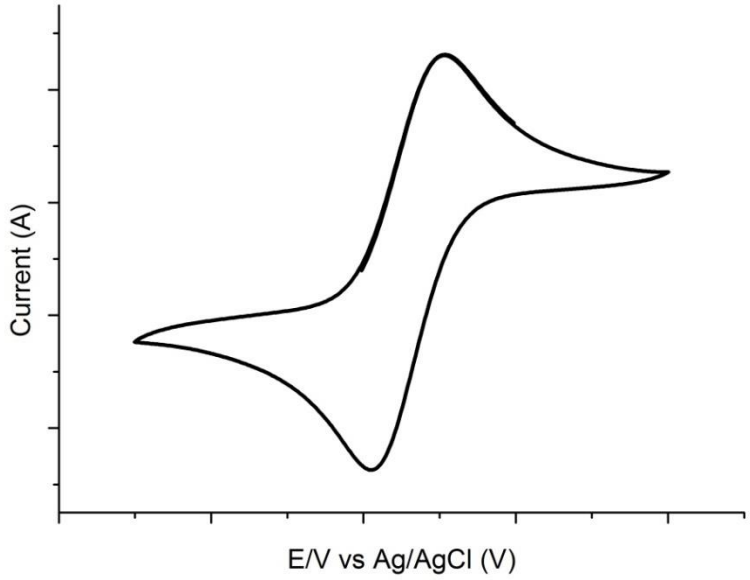

Figure 2.10. Typical peak shaped CV voltammogram.

Other key interest points involve the potentials at which the redox peaks appear, giving insight to when an electrode material causes oxidation/reduction of a target analyte to occur. The peak separation also gives information into the transfer kinetics, where ideally, a reversible process would follow the Nernstian value of 59.2/n mV, meaning a one electron transfer process would have a CV peak separation of 59.2 mV. Other information that can be gathered from CV is the concentration of the target analyte as the peak currents are stoichiometrically related to the amount of converted analyte that is being oxidized/reduced at the electrode surface, this is the basic mechanism for analyte detection.[35]

2.9 References

1. Berkowski, K. L., Plunkett, K. N., Yu, Q. & Moore, J. S. Introduction to Photolithography: Preparation of Microscale Polymer Silhouettes. *J. Chem. Educ.* **82,** 1365 (2005).

2. Jalili, N. & Laxminarayana, K. A review of atomic force microscopy imaging systems: application to molecular metrology and biological sciences. *Mechatronics* **14,** 907–945 (2004).

3. Donald, A. M. The use of environmental scanning electron microscopy for imaging wet and insulating materials. *Nat. Mater*. **2,** 511-516 (2003).

4. Malard, L. M., Pimenta, M. A., Dresselhaus, G. & Dresselhaus, M. S. Raman spectroscopy in graphene. *Phys. Rep.* **473,** 51–87 (2009).

5. Ferrari, A. C. & Basko, D. M. Raman spectroscopy as a versatile tool for studying the properties of graphene. *Nat. Nanotechnol.* **8,** 235–246 (2013).

6. Yang, D., Velamakanni, A., Bozoklu, G., Park, S., Stoller, M., Piner, R. D., Stankovich, S., Jung, I., Field, D. A., Ventrice Jr., C. A. & Ruoff, R. S. Chemical analysis of graphene oxide films after heat and chemical treatments by X-ray photoelectron and Micro-Raman spectroscopy. *Carbon* **47,** 145–152 (2009).

7. Díez-Betriu, X., Álvarez-García, S., Botas, C., Álvarez, P., Sánchez-Marcos, J., Prieto, C., Menéndez, R. & Andrés, A. de. Raman spectroscopy for the study of reduction mechanisms and optimization of conductivity in graphene oxide thin films. *J. Mater. Chem. C* **1,** 6905–6912 (2013).

8. Sarma, D. D., Santra, P. K., Mukherjee, S. & Nag, A. X-ray Photoelectron Spectroscopy: A Unique Tool To Determine the Internal Heterostructure of Nanoparticles. *Chem. Mater.* **25,** 1222–1232 (2013).

Chapter 3. Patterning of graphene with tunable size and shape for microelectrode array devices

Abstract

Large size and high quality graphene grown by chemical vapor deposition (CVD) has been fabricated into an array of discrete graphene sheets with well defined sizes and shapes. A fabrication process based on nanoimprint lithography has been developed to achieve shape tunability with sizes ranging from micrometer to nanometer. The technique preserves the quality of the CVD grown graphene and offers the versatility of transferring the graphene array onto any rigid or flexible substrate. The process is then expanded to fabricating a graphene based microelectrode array whose performance is demonstrated in the real time sensing of peroxidise excreted by breast cancer cells. The device displayed a linear working range of 0.01 to 25 mM and a sensitivity of 8.8 mA mol^{-1}.

3.1. Introduction

Since its discovery in 2004, graphene has attracted a large research interest due to its unique properties such as massless dirac fermions, room temperature ballistic conduction, high intrinsic bond strength and optical transparency.[1,2] Graphene, being atomically thick, possesses high surface to volume ratios that allow for increased active sites for target analytes. This property, coupled with graphene's high conductivity that results in low signal-to-noise ratios and

increased detection sensitivities,[3] has prompted a strong impetus to move it from a research platform to areas of utility where it can impact a diverse range of applications. Graphene based devices require their components to be fabricated in a particular shape/size and positioned on or within the device at specific locations. Currently, graphene sensing devices have largely been unconcerned with the size and shape of the graphene active site. However, in order to further push graphene based devices to positively impact commercial areas such as large array of transferable electric circuitry,[4,5] super capacitors,[6-8] transistors,[9-11] and sensors,[12,13] the parameters of scalability and consistency need to be addressed in order to fabricate reliable devices in a manner that is scalable.

Manipulating atomically thin graphene into desired shapes and sizes with high fidelity while allowing for large batch processing is not trivial as graphene sheets can be fragile and polymer residues from the transfer process can contaminate the active areas. Intense research efforts have been dedicated towards developing high fidelity transfer of these sheets onto arbitrary substrates.

Previous attempts at patterning include the use of polystyrene balls as a masking layer during the etching of grapheme which results in mesh-like patterns[14], microcontact printing where layers of graphene are lifted by means of a transfer substrate and stamped onto a receiving surface.[9] Ink jet printing of solution-processible graphene has also been demonstrated[15,16] and graphene sheets have also been patterned using a laser ablation process.[17] However, these methods have limitations in pattern design and upscaling. There is a

need to develop a process for shaping graphene into any desired conformation and transferring these patterned graphene onto specific areas.

This chapter reports an imprint patterning method that is amenable to size (micron to nano scales) and shape control in the structuring of the graphene sheet, encapsulating the graphene patterns which can then be transferred onto any arbitrary substrate. This process is then used to fabricate a workable graphene based sensor device.

3.2. Materials and Methods

3.2.1. Graphene Patterning

Graphene was grown using a chemical vapor deposition (CVD) process on copper foil. 1um thick poly methyl methacrylate (PMMA) from Microresist was spin coated onto the surface and imprinted using an Obducat Nanoimprinter at 150 degrees C, 50 Bar, for 5 minutes using silicon molds with differing patterns. Etching was carried out by an Oxford RIE to etch into the imprinted PMMA/Graphene/Copper foil sample. The timing was controlled to ensure the unwanted graphene areas were etched and a protective layer of PMMA remained. PMMA was once again spincoated over the freshly etched sample and the copper substrate dissolved in 0.5M $FeCl_3$ solution.

3.2.2. Graphene Fluorescence

Fluorescein sodium salt was purchased from Sigma Aldritch Co. 10mg of fluorescein salt was added to 1ml of ethanol solution. 1ml of 500nm thick PMMA solution was added to the fluorescein/ethanol solution to make a fluorescein resist. The resist was spin coated onto the transferred graphene paper. An Olympus BX 51 fluorescent microscope with NIS Elements D3.0 software was used for imaging.

3.2.3. Graphene Microelectrode Array Fabrication

A graphene microelectrode array (GMEA) was fabricated using a CVD graphene monolayer that was transferred onto an indium tin oxide (ITO)/glass substrate. A 10% w/w polyvinyl alcohol (PVA) solution was spin coated onto the graphene/ITO/glass substrate and imprinted. Upon demolding, the PVA patterned graphene sample was etched, resulting in a ITO/glass substrate with patterned graphene on its surface with a residual protective layer of PVA. This layer of PVA was then covered by a 1μm thick layer of PMMA which serves as an insulating layer. A subsequent etching was carried out on the PMMA layer and the time of etching controlled so that the underlying PVA layer was exposed. The sample was then placed in deionized water at 60 degrees C overnight under gentle stirring. This allows the protective PVA layer to be dissolved away to expose the underlying graphene layer to the environment (process in supporting documents). Graphene oxide microelectrode array (GOMEA) on ITO/polyethylene teraphthalate (PET) was fabricated in the same fashion, with the graphene monolayer replaced with

spin coating 2.5mg/ml GO solution onto the ITO/PET substrate at 5000rpm for 60 seconds.

3.2.4. H_2O_2 Detection

20mM of H_2O_2 in 1mM phosphate buffer saline (PBS) solution was used to characterize the response of GMEA and ITO microelectrode array (ITOMEA).

3.2.5. MCF-7 Breast Cell Growth

Cell culture: Human breast cancer MCF-7 cells were purchased from American Type Culture Collection (ATCC). The cells were grown in DMEM (Gibco) supplemented with 2mg/ml insulin, 1mM sodium pyruvate, 1mM nonessential amino acids, 4mM glutamine, 10% fetal calf serum (Gibco) and 50U/mL penicillin/streptomycin (Gibco). One day before testing, cells were trypsinized and seeded at a density of 3000 cells cm^{-2} on the GMEA.

3.2.6. Cyclic Voltammetry Characterisation

Cyclic voltammetry (CV) characterization was conducted in 1M KCl electrolyte solution, with Platinum mesh counter electrode, Ag/Cl reference electrode and 2.5mM Ruthenium Hexamine (III) Chloride redox agent.

3.2.7. Graphene Oxide Reduction

Electrochemical reduction of graphene oxide (GO) was conducted by immersing the GOMEA in 1M Na-PBS solution at 4.7pH. Using chrono amperometry (CA), the system was held at -0.9V for 270 seconds.

3.3. Results and Discussion

3.3.1. Graphene Patterning

Nanoimprint lithography (NIL) was employed as the primary technique to pattern graphene. Traditionally NIL uses a combination of a rigid mold and a resist. Under pressure and temperatures above the glass transition temperature of the resist, micron/nano sized structures can be created on the surface of the resist as it conforms to the shape of the patterns on the mold. Changing the structure types is dependent on the mold used during the imprint step and the size of the imprinted area is limited only by the size of the mold used. This flexibility in the NIL process is highly useful in graphene patterning as it possesses high tunability of the patterns with the generation of graphene patterns that could number into hundreds of thousands per imprint cycle. The high-resolution patterned molds used in NIL are usually fabricated by electron beam lithography (EBL).[18] Although EBL may be used directly to pattern graphene, and it has the flexibility of writing different shapes, it is a slow patterning process. As a result, EBL fabricated samples are costly. The synergy of using an EBL fabricated template for replication in NIL has been considered a more viable option for scale-up consideration. Importantly, for

the current work, NIL offers the flexibility in the choice of materials that can be used in the process.

In this work NIL is used as a templating instrument with the fabricated structures functioning as a masking template on top of graphene grown by a CVD process on copper foil. CVD graphene on copper foil is chosen as it allows for a large pristine graphene sheet to be obtained. However this method is not restrictive to CVD graphene.

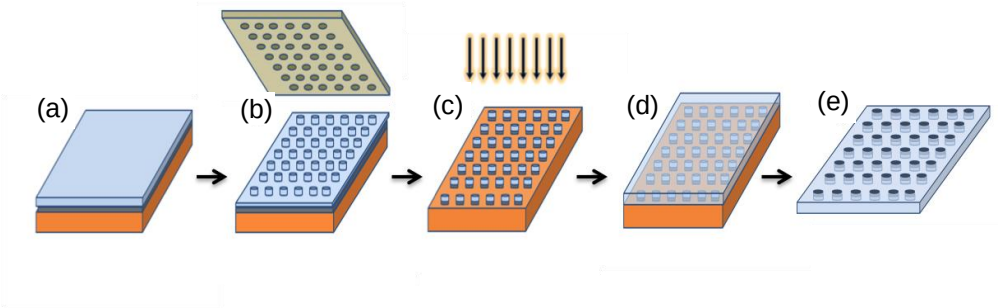

Figure 3.1. Process flow of imprint-patterning and transferring of graphene (a) 1µm PMMA layer is spin coated onto the graphene layer. (b) PMMA layer is imprinted. (c) Patterns are etched down into the underlying graphene layer. (d) Another layer of PMMA is spin coated onto the surface encapsulating the patterned graphene sheets on copper foil. (e) Copper foil is dissolved away in $FeCl_3$ solution leaving patterned graphene encapsulated in PMMA.

Graphene patterning has conventionally been restricted to transferring a graphene sheet onto a hard substrate on which patterning would then be conducted. However this restricts the substrate types that graphene patterns can be fabricated on. The substrate would need to be etch-resistant and flat so that consistent graphene patterns are fabricated across the imprint area. Patterning graphene post CVD synthesis and then encapsulating the patterns in a PMMA layer overcomes these restrictions as all fabrication processes are completed before transferring. Figure 3.1 illustrates the patterning and encapsulation process. The 1st PMMA layer acts as a pattern defining as well

as a protective layer. Reactive ion etching is then employed to etch away the unwanted graphene, leaving behind graphene patterns in the shape of the silicon mold patterns. Another layer of PMMA is then spin coated on top and the copper substrate dissolved in $FeCl_3$ solution. Allowing for this step, coupled with removal of the copper substrate, produces patterned graphene encased in a free standing PMMA layer that can be transferred onto any arbitrary substrate.

It must be highlighted the ease in which the different types of graphene patterns can be fabricated using this method, restricted only by the initial mold pattern. Patterns with straight edges, curved edges, patterns with holes within or a combination of these, with dimensions ranging from micron to submicron scales can be produced in a versatile method and on a large scale (Figures 3.2(a-c)).

The graphene patterns were transferred onto a silicon substrate with a 300 nm thick oxide layer. The encapsulated graphene patterns were positioned face down onto the substrate and placed on a heater at 105 ºC for 10 minutes. Any moisture between the encapsulated graphene patterns and substrate was removed allowing the patterned graphene to come into intimate contact with the substrate surface. The PMMA was then dissolved in acetone and the graphene patterns preferentially remained on the substrate surface. The sample was further treated in a vacuum furnace heated at 800 ºC for 1 hour to remove PMMA residuals that was not fully dissolved by the acetone wash.[19,20]

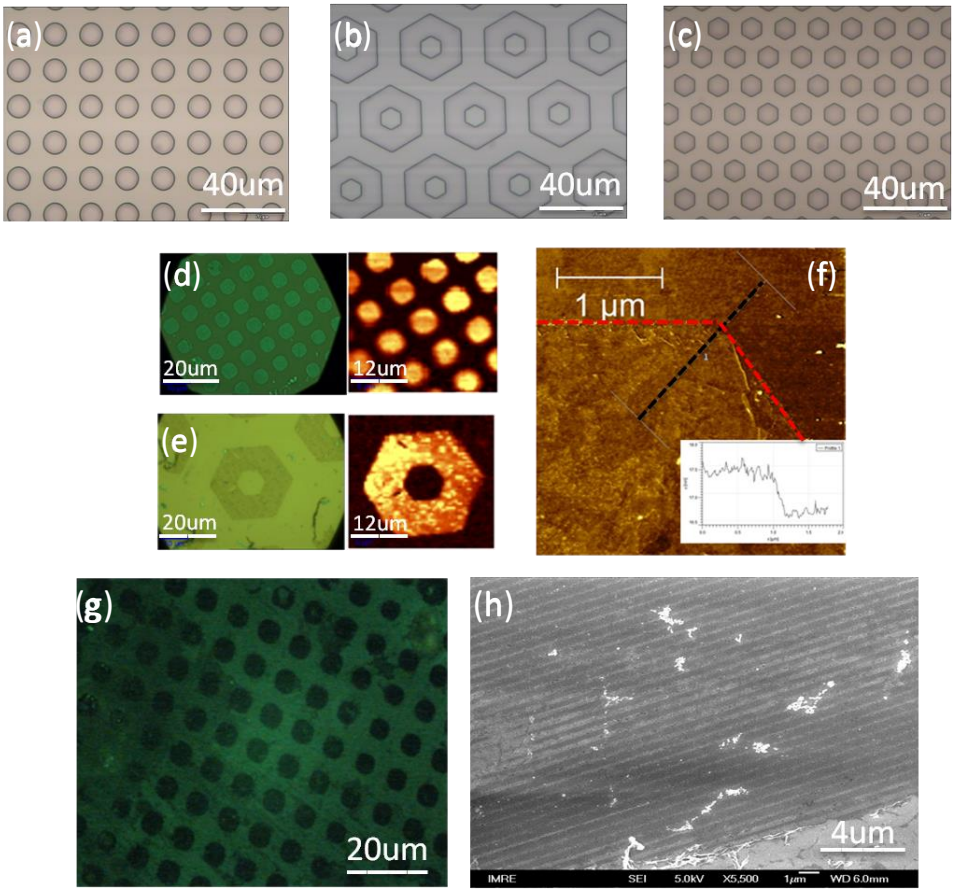

Figure 3.2. (a-c) Silicon molds used to pattern grapheme (discs, hexagon rings, hexagons) (d) Optical image of 5um graphene discs patterned and transferred onto SiO_2/Si substrate with corresponding 2D peak raman map. (e) Optical image of 14um sided hexagonal rings patterned and transferred onto SiO_2/Si substrate with corresponding 2D peak raman map. (f) Atomic force microscopy (AFM) image of the edge of a transferred 8um hexagon graphene sheet (g) Fluorescence quenching of 5µm graphene discs. (h) Scanning electron microscope (SEM) image of 250nm wide graphene line gratings.

Raman spectroscopy was used to identify the location of the transferred graphene. The Raman map of the 2D band follows a one-to-one spatial correlation with the optical images of the transferred graphene patterns (Figure 3.2 (d) and (e)). Figure 3.2(f) shows AFM imaging of the edge of an 8 µm hexagon graphene pattern transferred onto a SiO_2/Si substrate. The dotted red line indicates the ideal straight edge of the hexagon pattern. Although there was some evidence of lifting and folding of graphene at the edges caused by inadequate contact during the transfer process, overall there is a high fidelity

in the transferred graphene patterns, which attests to the robustness of the patterning process. The inset depicts the step height profile with a sharp edge step height of about 0.8 nm, characteristic of transferred graphene sheets.[21] The root-mean-square surface roughness of the patterned graphene was measured to be ~0.4 nm arising due to the differences in thermal expansion between graphene and the copper foil substrate it is grown upon, this caused slight wrinkling of the graphene surface post transfer.[22,23]

Due to graphene's semimetallic character, it possesses fluorescence quenching properties.[24] This property can be exploited to spatially locate graphene domains when a dye is applied. 100 nm thick fluorescein/PMMA/ethanol solution was spin coated onto a substrate that had 5 µm graphene disks transferred onto the surface. Figure 3.2(g) shows the 5 µm disks appearing darker compared to the surroundings, which evidenced the presence of graphene. Figure 3.2(h) shows graphene submicron line grating patterns of 250nm in width patterned and transferred onto SiO_2/Si substrate. The images in Figure 3.2(d) and (e) depict graphene patterns with high fidelity that were fabricated with high throughputs per imprint step. Figure 3.3 shows various graphene patterns with corresponding, 2D peak mapping and G and 2D band peaks of graphene being seen at 1580 and 2700 cm^{-1} respectively,[25,26] in all patterned arrays.

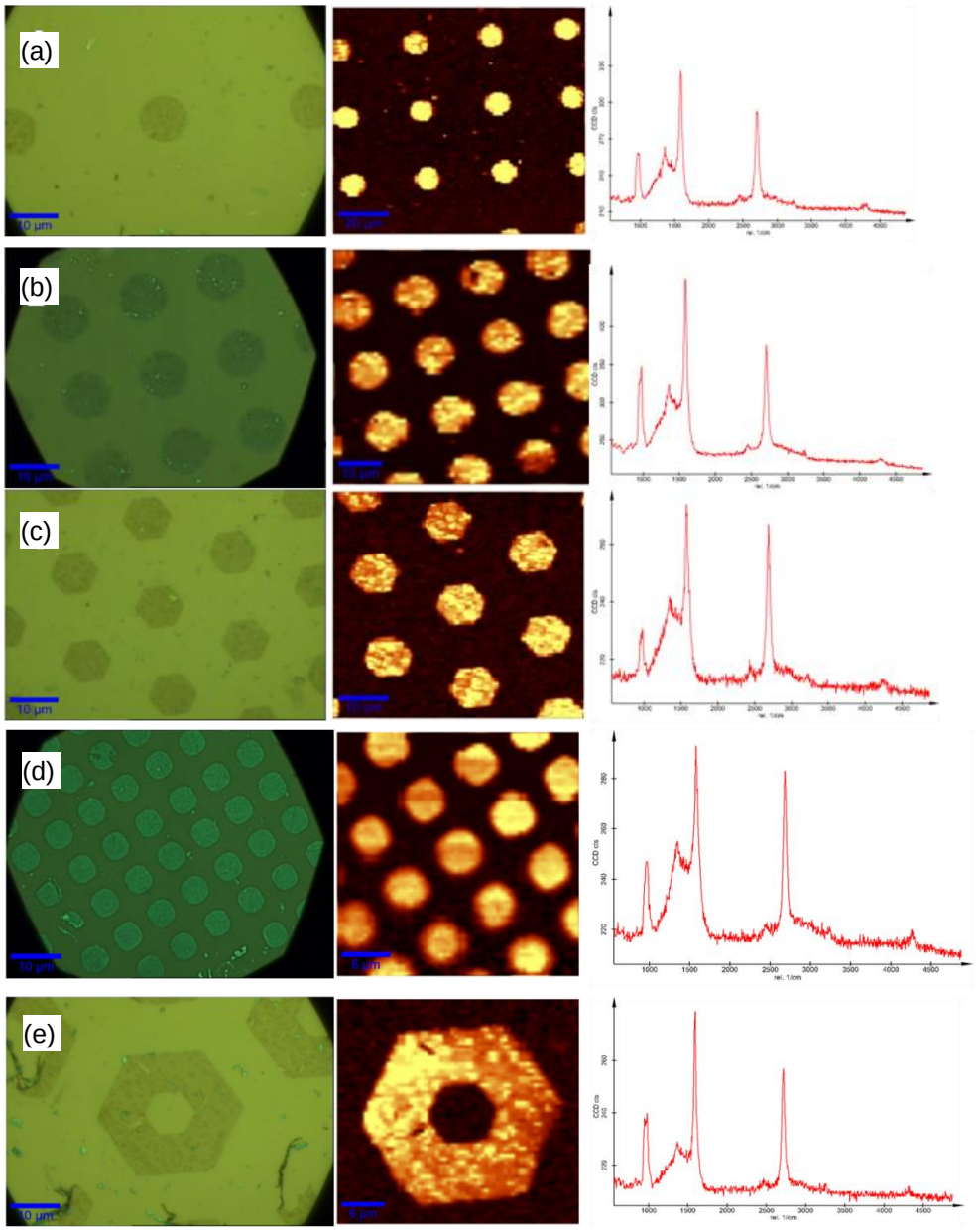

Figure 3.3. (Left to Right) Graphene Patterns: Optical Image, 2D peak Raman Map, Raman Spectroscopy of graphene areas showing strong G and 2D peaks. (a) 10 um discs with 30 um pitch separation (b) 10 um discs with 10 um separation (c) 8 um sided hexagons (d) 5 um discs (e) Hexagon Rings.

3.3.2. Graphene Microelectrode Array

The imprint process was adapted to fabricate a GMEA (Figure 3.4) using a 10% w/w solution of poly vinyl alcohol (PVA) as the resist pattern layer. In this

process PVA and PMMA were selected because of their different solubility properties. Once patterned and etched, the PVA layer was readily dissolved in water to expose the underlying graphene active site.

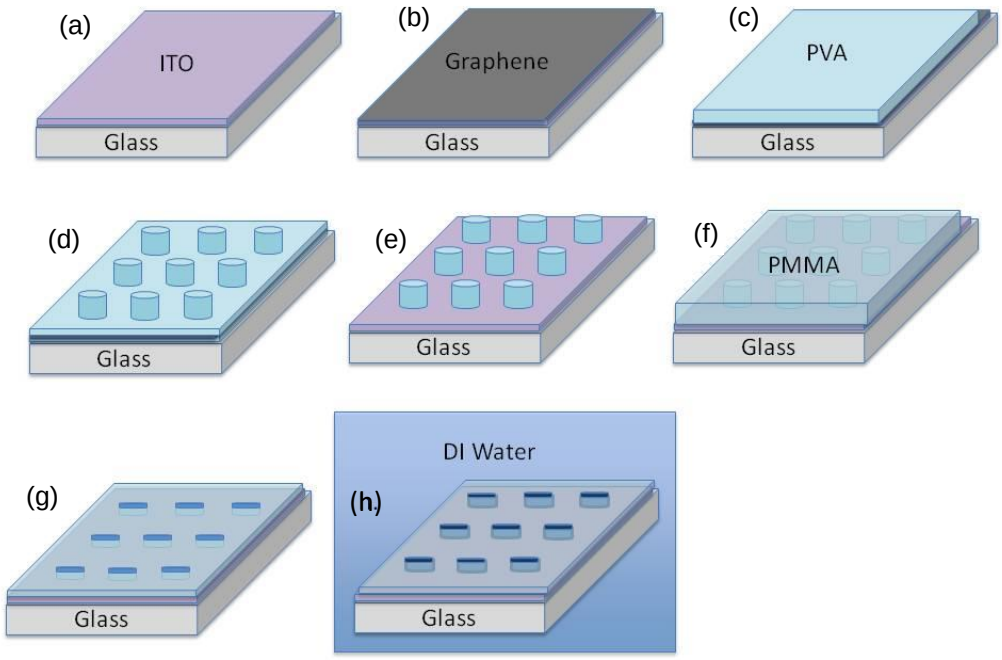

Figure 3.4. Work flow of Graphene microelectrode array fabrication (a) ITO/glass substrate is cleaned. (b) CVD graphene is transferred onto ITO/glass substrate. (c) 10% w/w PVA layer is spincoated over the graphene. (d) PVA is imprinted. (e) Reactive ion etching is employed to etch the graphene layer but leave a residual PVA protective layer. (f) A 1 um thick PMMA layer is spincoated over the patterned PVA layer. (g) The PMMA is etched to expose the underlying PVA patterns. (h) The device is placed into a 60 ^{o}C deionized water bath to dissolve the PVA and expose the underlying active graphene site.

A microelectrode has several advantages over conventional electrode sensors being capable of functioning in highly resistive environments, possessing higher detection sensitivity for trace analytes, exhibiting very little capacitance and solution resistance effects, and having high mass transport rates. Furthermore, once a microelectrode is fashioned into an array assembly, an

amplification effect of the signal is created which allows for even lower detection limits.[27,28] Being able to incorporate graphene into the active sites where electrochemical interaction occurs between the analyte and the device further enhances the sensors performance as graphene possesses a wide electrochemical window, strong affinity to single strand nucleic acids and chemical stability.[29,30]

Figure 3.5(a) and (b) show the images of the patterned GMEA. 10 µm discs with 60 µm hole-to-hole separation were used to reduce the overlap of diffusion hemispheres during CV characterization. This was necessary for the GMEA device to exhibit microelectrode behavior identifiable by a sigmoidal response in the CV shape. It should be noted that as with the patterning process, the ability to tailor the shape, size and hole to hole separation of the active areas of the GMEA was carried out by changing the original silicon mold used to pattern the sacrificial layer.

The performance of the GMEAs were characterized using CV with 2.5 mM Ruthenium Hexamine (III) Chloride as the redox agent. Figure 3.5(c) depicts sigmoidal responses at small scan rates, which was evidence of microelectrode array behavior. As scan rates increased, the redox peaks became much more prominent. This was due to microelectrodes tending towards a mixture of planar and radial diffusion at the individual active sites resulting in peak-like responses.[31] The peak currents were correlated to the square root of the scan rate and found to be linear, correlating to a diffusion limited behavior.

Figure 3.5(d) shows anodic oxidation of 20 mM hydrogen peroxide (H_2O_2) that was carried out on the GMEA and an ITOMEA without graphene using

CV in 1 mM PBS solution. The GMEA device displayed superior catalytic properties towards H_2O_2 as compared to the ITOMEA, displaying an anodic current 20 times stronger than an ITOMEA without graphene as the active site. The oxidation peak was recorded at 0.4 V and reduction peak at -0.1 V consistent with previous findings.[24] The device demonstrated a linear working range of 0.01 mM to 25 mM with a sensitivity of 8.8 mA mol^{-1}. Although this figure was lower than other reported values, it must be noted that the active area was significantly smaller than other reported graphene sensors[24] and H_2O_2 was detected without any mediating reagents or modification of the graphene surface.[32,33]

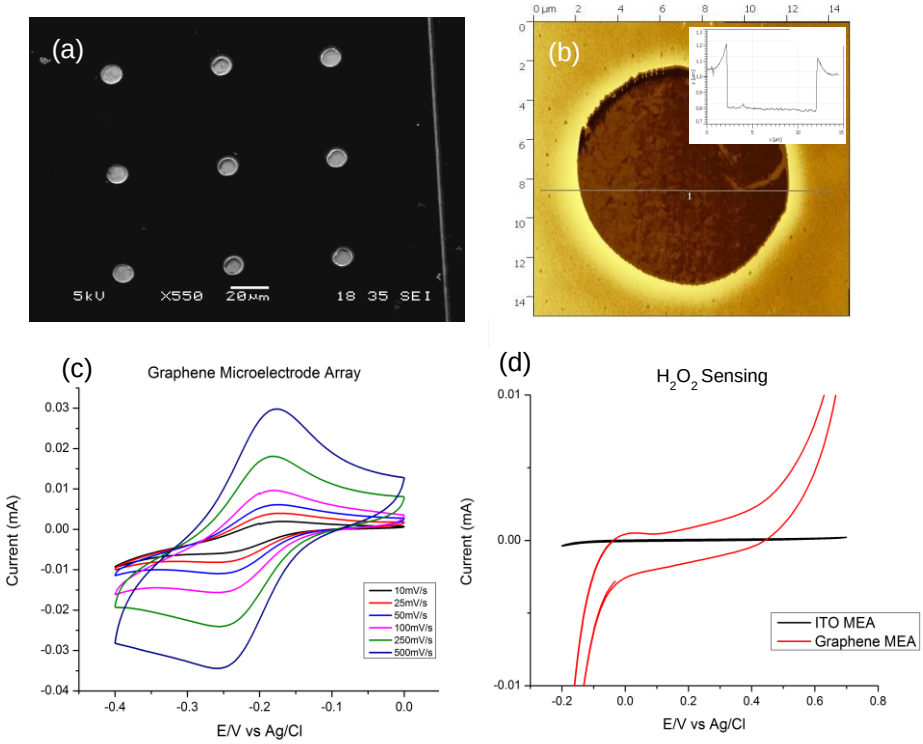

Figure 3.5. (a) SEM image of the GMEA. (b) AFM imaging of one circular GMEA disk. Inset profile shows step height due to 250 nm thick PMMA passivation layer. (c) CV of GMEA showing sigmoidal behavior at low scan rates and increasing peak-shaped behavior at high scan rates. (d) CV of H_2O_2 sensitivity, compared to a microelectrode array with no graphene.

The GMEA device can be applied for the dynamic sensing of cancerous cells. Early determination of cancer cells is a crucial step for successful oncological treatment. MCF-7 breast cancer cells were grown on the GMEA device after which Phorbol 12-myristate 13-acetate (PMA) was used to stimulate the MCF-7 cells to generate H_2O_2.[34] A low seeding density of 3000 cells per cm^{-2} was used (Figure 3.6(a)). Figure 3.6(b) shows CA of the GMEA device analyzing the presence of peroxidise excreted by the breast cancer cells. Each current spike corresponded to the moment when PMA was introduced into the system, indicating a release of H_2O_2 molecules by the cancer cells that then catalyze at the graphene active sites. Once the H_2O_2 at the active sites were fully consumed, the current returned to a stable level. Approximately 100 µl of 0.5 ug/ml of PMA was injected each time to stimulate the cells to produce H_2O_2. Upon injection, the signal spiked instantaneously. A control test performed on a second device that did not have any MCF-7 cells showed no response, thus eliminating the possibility of current peaks from the PMA itself. In addition, the cells on the GMEA device were killed by washing with 0.5 M of potassium hydroxide, and the sensing experiment was repeated. No peak signals were observed upon injection of PMA. The electrochemical sensing results therefore demonstrate clearly that the GMEA have exposed surfaces with active electrochemical activity and was not passivated by residual organic resists. Also the GMEA device shows promise in real world sensing applications. Further optimization and modification of the graphene active sites would allow for a wider range of chemicals to be detected and increase in sensitivities and detection limits.

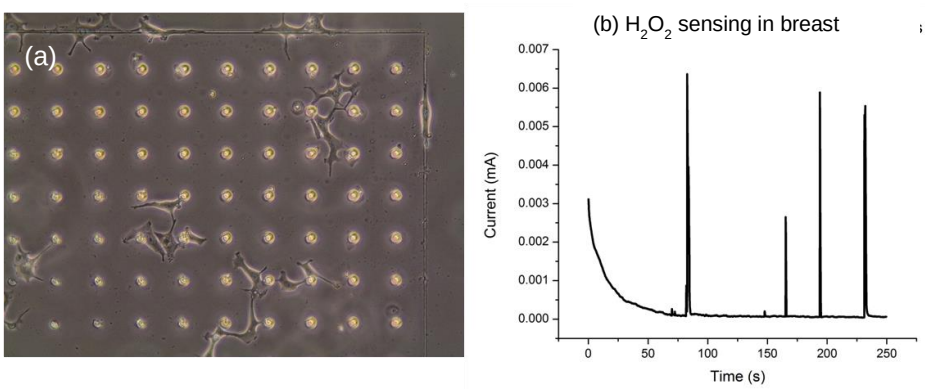

Figure 3.6. (a) Optical image of MCF-7 breast cancer cells grown on the surface of the GMEA. (b) CA of GMEA device. CA spikes corresponding to the release of peroxidase from cancer cells upon injection of PMA.

3.4. Conclusions

A high fidelity method of transferring patterned graphene with a wide range of shapes and sizes onto arbitrary substrates was demonstrated. The process was also adapted to fabricate periodic graphene arrays for application in MEA sensors. Utilizing this process to fabricate sensors at low processing temperatures and pressures that displayed real world applications, the prototype sensor was able to detect H_2O_2 excreted from breast cancer cells.

Further research can be carried out to optimize the sensitivities and detection limits of the devices and to integrate multiple differing active sites on a single device where sensing of different analytes can be carried out simultaneously.

3.5. References

1. Hernandez, F. J. & Ozalp, V. C. Graphene and Other Nanomaterial-Based Electrochemical Aptasensors. *Biosensors.* **2**, 1-14 (2012).

2. Brownson, D. A. C. & Banks, C. E. Graphene electrochemistry: an overview of potential applications. *Analyst.* **135**, 2768-2778 (2010).

3. Novoselov, K. S., Geim, A. K., Morozov, S. V., Jiang, D., Katsnelson, M. I., Grigorieva, I. V., Dubonos, S. V. & Firsov, A. A. Two-dimensional gas of massless Dirac fermions in graphene. *Nature.* **438**, 197-200 (2005).

4. Hong JY, Shin KY, Kwon OS, Kang H & Jang J A strategy for fabricating single layer graphene sheets based on a layer-by-layer self-assembly. *Chem. Commun.*. **47**, 7182-7184 (2011).

5. Cox M, Gorodetsky A, Kim B, Kim K S, Zhang J, Kim P, Nuckolls C & Kymissis I Single-layer graphene cathodes for organic photovoltaics. *Appl. Phys. Lett.*. **98**, 3 (2011).

6. Stoller MD, Park S, Zhu Y, An J & Ruof RS Graphene-Based Ultracapacitors. *Nano Lett.* **8**, 3498-3502 (2008).

7. Wang, D. W., Li, F., Wu, Z. S., Ren, W. & Cheng, H. M. Electrochemical interfacial capacitance in multilayer graphene sheets: Dependence on number of stacking layers. *Electrochemistry Communications.* **11**, 1729-1732 (2009).

8. Yoo, J. J., Balakrishnan, K., Huang, J., Meunier, V., Sumpter, B. G., Srivastava, A., Conway, M., Mohana Reddy, A. L., Yu, J., Vajtai, R. & Ajayan, P. M. Ultrathin planar graphene supercapacitors. *Nano Lett.* **11**, 1423-1427 (2011).

9. Allen, M. J., Tung, V. C., Gomez, L., Xu, Z., Chen, L. M., Nelson, K. S., Zhou, C., Kaner, R. B. & Yang, Y. Soft Transfer Printing of Chemically Converted Graphene. *Advanced Materials.* **21**, 2098-2102 (2009).

10. Çağlar Ö. Girit & A. Zettl Graphene at the Edge: Stability and Dynamics. *Science.* **323**, 1705-1708 (2009).

11. Jeroen B Oostinga, Hubert B Heersche, Xinglan Liu, Alberto F Morpurgo & Lieven M K Vandersypen Gate-induced insulating state in bilayer graphene devices. *Nat Mater.* **7**, 151-157 (2007).

12. Ohno Y, Maehashi K, Yamashiro Y & Matsumoto K Electrolyte-gated graphene field-effect transistors for detecting pH and protein adsorption. *Nano Lett.* **9**, 3318-3322 (2009).

13. Ye Lu, B R Goldsmith, N J Kybert & A T C Johnson DNA-decorated graphene chemical sensors. *Applied Physics Letters.* **97**, 3 (2010).

14. Rajat Kanti Paul, Sushmee Badhulika, Nuvia M Saucedo & Ashok Mulchandani Graphene Nanomesh As Highly Sensitive Chemiresistor Gas Sensor. *Anal. Chem.*. **84**, 8171-8178 (2012).

15. Dua, V., Surwade, S. P., Ammu, S., Agnihotra, S. R., Jain, S., Roberts, K. E., Park, S., Ruoff, R. S. & Manohar, S. K. All-Organic Vapor Sensor Using Inkjet-Printed Reduced Graphene Oxide. *Angewandte Chemie International Edition.* **49**, 2154-2157 (2010).

16. Seok Ju Kang Inking Elastomeric Stamps with Micro-Patterned, Single Layer Graphene to Create High-Performance OFETs. *Advanced materials.* **23**, 3531-3535 (2011).

17. Gao, W., Singh, N., Song, L., Liu, Z., Reddy, A. L. M., Ci, L., Vajtai, R., Zhang, Q., Wei, B. & Ajayan, P. M. Direct laser writing of micro-supercapacitors on hydrated graphite oxide films. *Nature nanotechnology.* **6**, 496-500 (2011).

18. Fabrication of a Graphene Nanoribbon with Electron Beam Lithography Using a XR-1541/PMMA Lift-Off Process. *Transactions on Electrical and Electronic Materials.* **11**, 190-193 (2010).

19. Lin, Y. C., Lu, C. C., Yeh, C. H., Jin, C., Suenaga, K. & Chiu, P. W. Graphene annealing: how clean can it be? *Nano Lett.* **12**, 414-419 (2012).

20. Pirkle, A., Chan, J., Venugopal, A., Hinojos, D., Magnuson, C. W., McDonnell, S., Colombo, L., Vogel, E. M., Ruoff, R. S. & Wallace, R. M. The effect of chemical residues on the physical and electrical properties of chemical vapor deposited graphene transferred to SiO2. *Applied Physics Letters.* **99**, 122108-122108 (2011).

21. Riedl, C., Coletti, C. & Starke, U. Structural and electronic properties of epitaxial graphene on SiC (0 0 0 1): a review of growth, characterization, transfer doping and hydrogen intercalation. *Journal of Physics D: Applied Physics.* **43**, 374009 (2010).

22. Guo, C. X., Zheng, X. T., Lu, Z. S., Lou, X. W. & Li, C. M. Biointerface by cell growth on layered graphene-artificial peroxidase-protein nanostructure for in situ quantitative molecular detection. *Advanced materials (Deerfield Beach, Fla.).* **22**, 5164-5167 (2010).

23. Chae, S. J., Güneş, F., Kim, K. K., Kim, E. S., Han, G. H., Kim, S. M., Shin, H. J., Yoon, S. M., Choi, J. Y., Park, M. H., Yang, C. W., Pribat, D. & Lee, Y. H. Synthesis of Large-Area Graphene Layers on Poly-Nickel Substrate by Chemical Vapor Deposition: Wrinkle Formation. *Advanced Materials.* **21**, 2328-2333 (2009).

24. Penmatsa, V., Kim, T., Beidaghi, M., Kawarada, H., Gu, L., Wang, Z. & Wang, C. Three-dimensional graphene nanosheet encrusted carbon micropillar arrays for electrochemical sensing. *Nanoscale.* **4**, 3673-3678 (2012).

25. Ni, Z., Wang, Y., Yu, T. & Shen, Z. Raman spectroscopy and imaging of graphene. *Nano Research.* **1**, 273-291 (2008).

26. Ferrari, A. C., Meyer, J. C., Scardaci, V., Casiraghi, C., Lazzeri, M., Mauri, F., Piscanec, S., Jiang, D., Novoselov, K. S., Roth, S. & Geim, A. K. Raman Spectrum of Graphene and Graphene Layers. *Phys Rev Lett.* **97**, (2006).

27. Hans-Peter Nirmaier & Günter Henze Characteristic behavior of macro-, semimicro- and microelectrodes in voltammetric and chronoamperometric measurements. *Electroanalysis.* **9**, 619-624 (1997).

28. M Irene Montenegro, M Arlete Queirós & John L Daschbach in 227 , Portugal, 1990).

29. Li, F., Xue, M., Ma, X., Zhang, M. & Cao, T. Facile patterning of reduced graphene oxide film into microelectrode array for highly sensitive sensing. *Anal Chem.* **83**, 6426-6430 (2011).

30. Brownson, D. A. C., Lacombe, A. C., Gómez-Mingot, M. & Banks, C. E. Graphene oxide gives rise to unique and intriguing voltammetry. *RSC Advances.* **2**, 665-665 (2011).

31. Guo, J. & Lindner, E. Cyclic voltammograms at coplanar and shallow recessed microdisk electrode arrays: guidelines for design and experiment. *Anal Chem.* **81**, 130-138 (2009).

32. Wang, A. J., Zhang, P. P., Li, Y. F., Feng, J. J., Dong, W. J. & Liu, X. Y. Hydrogen peroxide sensor based on glassy carbon electrode modified with β-manganese dioxide nanorods. *Microchimica Acta.* **175**, 31-37 (2011).

33. Zhang, L., Yuan, S. M., Yang, L. M., Fang, Z. & Zhao, G. C. An enzymatic glucose biosensor based on a glassy carbon electrode modified with manganese dioxide nanowires. *Microchimica Acta.* , (2013).

34. M, N. Cellular antioxidant and antiproliferative activity of ethanolic extract of Coleus tuberosus. *Journal of Medicinal Plants Research.* **6**, (2012).

Chapter 4. Highly Sensitive Reduced Graphene Oxide Microelectrode Array Sensor

Abstract

Reduced graphene oxide (rGO) has been fabricated into a microelectrode array (MEA) using a modified nanoimprint lithography (NIL) technique. Through a modified NIL process, the rGO MEA was fabricated by a self-alignment of conducting Indium Tin Oxide (ITO) and rGO layer without etching of the rGO layer. The rGO MEA consists of an array of 10 μm circular disks and microelectrode signature has been found at a pitch spacing of 60 μm. The rGO MEA shows a sensitivity of 1.91 nA μm^{-1} to dopamine (DA) without the use of mediators or functionalization of the reduced graphene oxide (rGO) active layer. The performance of rGO MEA remains stable when tested under highly resistive media using a continuous flow set up, as well as when subjecting it to mechanical stress.. The successful demonstration of NIL for fabricating rGO microelectrodes on flexible substrate presents a route for the large scale fabrication of highly sensitive, flexible and thin biosensing platform.

4.1. Introduction

A microelectrode has many advantages which include enhanced signal to noise ratios, increased mass diffusion, ease of miniaturization and operation in highly resistive media.[1,2] However one of the disadvantages of reducing electrode sizes to sub-millimeter length scales is the reduced signals associated with the reduction in active area, where the current levels are reduced to nano and pico amp ranges. A commonly reported approach to enhance the signals is to functionalize the active layer with nanoparticles.[3,4] Another method is to fabricate the sensor device into an array to allow an increase in total effective active area, thereby increasing the sensitivity of the sensor.[1] In such an approach, the spacing between each microelectrode should be optimized so that the boundary layer of each microelectrode where concentration of the analyte differs from the concentration in bulk solution, also known as a diffusion hemisphere, do not overlap,[5] as the latter occurrence will compromise the fast radial diffusion characteristics of an MEA.[6,7]

In sensors, besides the electrode, the other critical component is the material that allows electrochemical reactions to occur – the active layer. Conventionally, gold, platinum and silver metals have been the predominant material used since the active layer needs to be electrically conductive.[8–12] However there are other emerging organic electro-active materials such as poly(ethylenedioxythiophene), glassy carbon electrodes, carbon nanotubes, graphene, and reduced graphene oxide (rGO).[13–17] These materials are generally lower in cost to use and potentially allow for more useful fabrication techniques in contrast to conventional metal sputtering/lithography methods, generating research interest in utilizing them in electrochemical applications.[18]

There are several advantages of using rGO as an active layer in sensing applications. rGO is prepared by the chemical or thermal reduction of GO. Following the reduction process, oxygen atoms are partially removed from the surface and the sp^2 conjugation is recovered to some extent, thus allowing the rGO layer to be electrically conductive.[19] When used as an electrode, rGO can oxidize or reduce the target analyte depending on the analytes formal potential. rGO is has a large electrochemical potential window, easily solution processable, has oxygen moieties strewn across its carbon lattice that allow electrochemical reactions to take place. These attributes have been extensively covered in literature.[20–25] Most previous studies focused on planar, macroscopic electrodes made of drop-casted or spin-coated rGO multilayer films onto pre-fabricated electrode platforms such as a glassy carbon electrode (GCE).[26,27] The solution processable nature of rGO allows it to be readily functionalized, creating an active material that can be highly tuned to specific analytes ranging from proteins, DNA and enzymes. Further in-depth reading into the detection properties of rGO has been published in the review article by Wu et al.[28] However, addressing the problems of MEA fabrication of thin film active layers on rGO has been scarce due to the difficulties in integrating these into MEA configurations. One method to increase the currents is to fabricate the microelectrodes into an array format. In an array configuration with multiple microelectrode openings, these active layers work in parallel to increase the overall current in the sensor. However conventional microelectrode array fabrication methods have been developed mainly for thick metal active layers,[29] and the fabrication challenges for rGO MEAs arise

from the difficulty in controlling the depth of etching for thin 2-D materials like rGO.

Li. F. et al previously reported a rGO MEA based on coating a substrate with a GO layer and using hydrazine filled polydimethylsiloxane (PDMS) wells to generate a spatial array of electrochemically active rGO disks. However one drawback with this method is that the initially insulating GO layer becomes electrochemically active due to inevitable electrochemical reduction during actual usage, which will lead to a loss of well-defined electrochemically active areas on the surface.[30] He. Q. et al reported patterning micron-size wide bands of GO using capillary actions through a PDMS stamp followed by its chemical reduction.[31] However, this method is limited in terms of the shape and size of the rGO layers.

NIL is a method to create micro to nano scale surface patterns using thermal or UV curable resists. It is a mechanical replication process where the negative of the relief structure on a mold (typically Si or quartz) is transferred to a resist either at elevated temperature or under the exposure of UV radiation. The pattern resolution in NIL is governed primarily by the pattern resolution of the mold, and the imprint fidelity is mainly dependent on material properties and process optimization. NIL allows patterning of surfaces on a large scale with the patterned area only limited by the size of the mold. Most importantly, NIL is a versatile lithographic technique where various resists materials can be used and the imprint process window is tuneable according to the material properties. NIL presents a suitable fabrication method to create micro-array patterns.[32,33] Through a process modification, it was recently reported the fabrication of size and shape tunable graphene and graphene oxide.[20] Building

on the earlier process development, the fabrication of a biosensor based on microelectrode array of rGO was reported and shows that it can function as highly sensitive biosensors.

4.2. Materials and Methods

All chemicals were purchased at Sigma-Aldrich Co unless otherwise stated.

4.2.1. GO Preparation

GO was produced by adding 1.5 g of Graphite powder, 1.5 g of $NaNO_3$ and 69 ml H_2SO_4 into a conical flask and stirred in an ice bath. 9 g of $KMnO_4$ was slowly added to the mixture which was cooled in the ice bath. Solution was then transferred to an oil bath at 35 ^oC. 120 ml of deionized (DI) water was added to the flask. Further stirring for 30 minutes as temperature of oil bath increased to 90 ^oC. 300ml of water was slowly added. 9 ml of H_2O_2 was added to the mixture. The solution was then filtered and washed through with DI water, leaving GO powder. The GO powder was then sonicated in DI water using a 500 W Fisher Scientific probe sonicator at 30% amplitude, 3 second on/off pulse for 15 minutes.

4.2.2. rGO MEA Device Fabrication

10% Polyvinylalcohol (PVA) was spin coated on rGO at 3000 rpm for 30 seconds. An Obducat nanoimprinter was used to imprint PVA at 105 ^oC, 50 bar for 10 minutes. The imprinted PVA layer was then etched using an Oxford RIE using 10 sccm of O_2 for 8 minutes. 1 µm thick Poly methylmethacrylate (PMMA) from Microresist Technology was then spin coated on top of the patterned and etched PVA layer at 3000 rpm for 30 seconds. The PMMA layer was then etched in an Oxford RIE using 10 sccm of O_2 for 5 minutes. The exposed PVA layer was then dissolved in DI water for 2 hours.

4.2.3. Electrochemical Reduction of GO

After spincoating GO onto the an Indium Tin Oxide/Polyethylene Terephthalate (ITO/PET), the GO layer was reduced by immersing the GO/ITO/PET substrate in 0.1 M Sodium phosphate buffer saline (Na-PBS) solution pH 4.5. The device was then held at -0.9 V for 3 minutes. XPS data was then carried out on GO and rGO samples to determine the difference in oxygen ratios after reduction (Appendix A).

4.2.4. Electrochemical Experiments

Cyclic Voltammetry (CV), Differential Pulse Voltammetry (DPV) and Chronoamperometry (CA) were carried out using an Autolab potentiostat with a 3 electrode setup. A platinum mesh was used as the counter electrode and Ag/AgCl was used as the reference electrode.. Ruthenium (III) hexamine in 0.1 M KCl solution was used as the redox couple during CV.

DPV was conducted in 0.1 M Na-PBS (pH 7.4) solution with settings of 5 mV step potential, 25 mV modulation amplitude and 0.5 s interval time.

CA was conducted in 0.1 M Na-PBS (pH 7.4) solution with a constant potential of 0.5 V and 0.14 V and data acquisition of 0.05 s intervals for the interference experiment.

4.2.5. Microfluidic Device Fabrication

The microfluidic device has a width of 500 µm and a height of 100 µm and was designed using CAD software. The design was then fabricated in PDMS polymer (Sylgard 184, Dow Corning, USA) based on soft lithographic technique. In brief, the patterned SU-8-based silicon master was first silanized with trichloro(1H, 1H, 2H, 2H-perfluorooctyl)silane. Next, the PDMS pre-polymer was mixed with the curing agent, poured onto the silanized silicon wafer in a ratio of 10:1 (w/w) and subsequently cured at 80 ^{o}C for 2 hours. Holes of 1.5 mm were cored for fluidic inlets and outlets. Finally, the PDMS mold was bonded to microscopic glass slide, with the rGO MEA sandwiched in between, using a homemade physical clamp.

4.3. Results and Discussion

4.3.1. rGO MEA Device Fabrication

In an earlier report, a sacrificial dual-resist NIL technique was developed to pattern chemical vapor deposited (CVD) graphene and graphene oxide.[20] This technique allows us to pattern the molecular-thin graphene and graphene-oxide without needing an etching step, hence it offers the advantage of preserving the quality of the CVD grown graphene. Based on the same working principle, the NIL technique is used in this work as it further offers the advantage in the ease of tuning the microelectrode geometry and array density. One can tune the microelectrode pitch sizes to create a pattern array geometry that exhibits microelectrode behavior while maximizing the number of microelectrode openings.

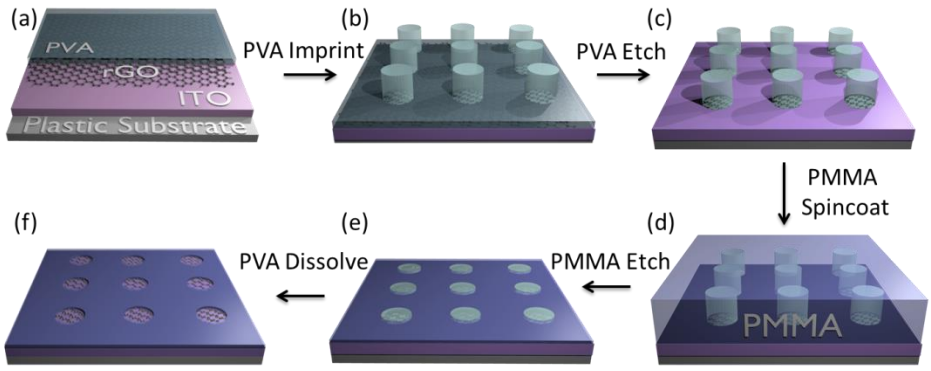

Figure 4.1. (a) PVA is spin coated onto electrochemically reduced graphene oxide (rGO). (b) PVA layer is patterned into a pillar array through NIL. (c) Patterned PVA layer is etched down to remove unwanted rGO, leaving PVA pillars protecting the rGO active layer array. (d) PMMA layer is spin-coated on top of the patterned and etched PVA layer. (e) PMMA layer etched to expose PVA layer. (f) PVA layer is dissolved in DI water to reveal underlying rGO active layer. The final product consists of exposed rGO disk array surrounded by PMMA, the latter passivates the unexposed area from the electrolyte.

Figure 4.1 shows the fabrication process for the rGO MEAs. GO is spin coated onto ITO/PET substrate and electrochemically reduced using 0.1 M Na-PBS pH4.5 at -0.9 V for 3 minutes. GO is an insulating material, due to the oxidation process disrupting the sp^2 network. GO can be readily reduced using electrochemical reduction. This results in a partial recovery of the π conjugation that is needed for electrical conduction.[19,34] A layer of PVA is then spin coated on top of the rGO layer (Figure 4.1(a)) and imprinted to create pillars of 10 µm in diameter over the surface of the rGO (Figure 4.1(b)). The patterned PVA layer functions as a sacrificial layer during the etching step, affording protection to the rGO layer below the pillars (Figure 4.1(c)). A layer of PMMA is then spin coated on top of the patterned PVA layer to act as the insulating barrier between the ITO and the electrolyte (Figure 4.1(d)). This step effectively eliminates the need to align the ITO with the rGO pattern

array. Using two resists of differing soluble properties thus allows for a self-aligning mechanism to insulate the underlying ITO.

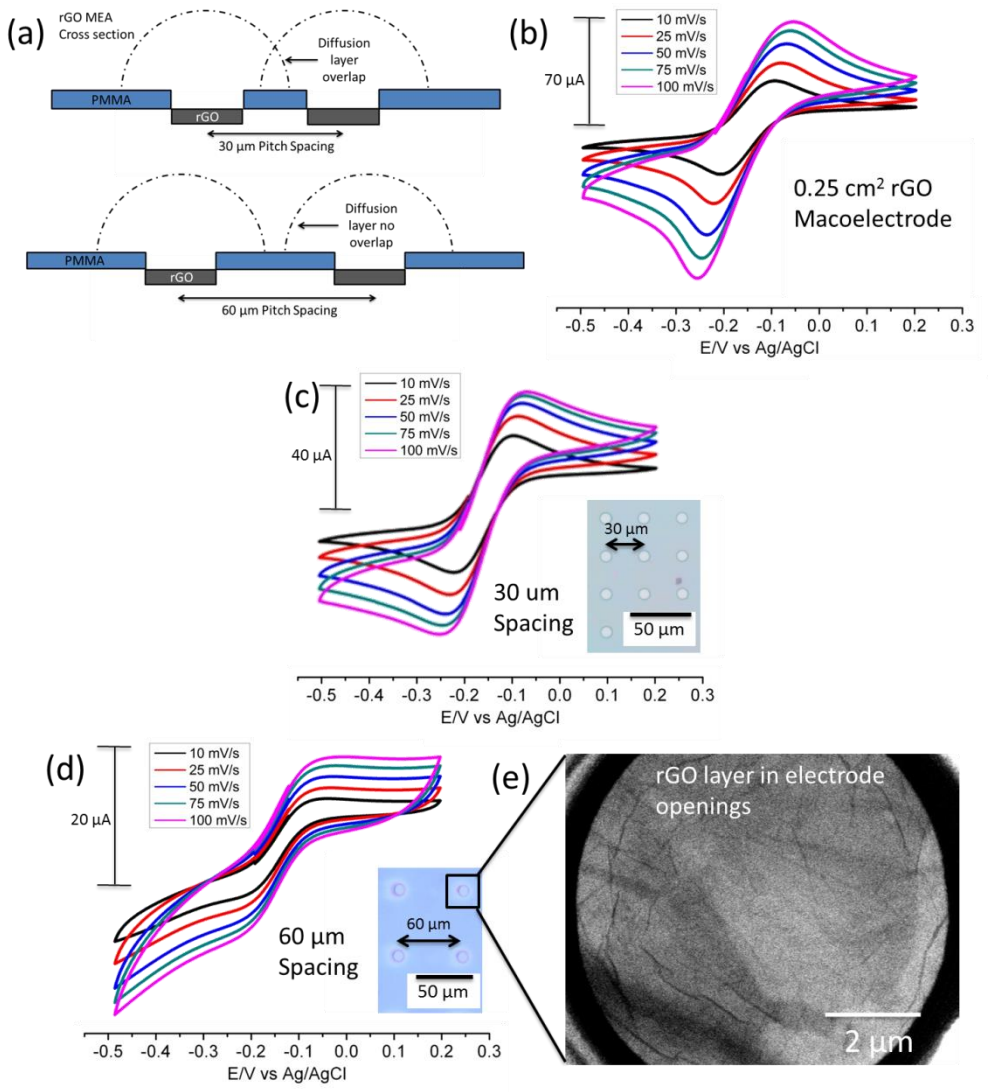

Figure 4.2. (a) Schematic of diffusion hemisphere overlapping when microelectrodes are fabricated in close proximity and no overlapping of diffusion hemispheres when microelectrodes are fabricated at pitch distances greater than twice the radius of the diffusion hemisphere. (b) CV data with increasing scan rate, using a 0.25 cm^2 rGO macroelectrode. (c) CV data of rGO MEA with 30 µm pitch spacing. (d) CV data of rGO MEA with 60 µm pitch spacing. (e) SEM image of rGO layer inside an exposed microelectrode.

The fabricated rGO MEA consists of an array of 10 µm disks separated by various pitch spacing. CV characterization was done using 2.5 mM ruthenium

hexamine as the redox probe to determine the minimum pitch spacing between the individual microelectrodes which allows microelectrode behavior. Figure 4.2(a) shows the schematic of how the MEA geometry can affect the overlap of diffusion hemispheres and cause the device to function as a macroelectrode instead of a microelectrode. Pitch distances between microelectrodes are required to be greater than two times the radius of the diffusion hemisphere in order for the diffusion layers to be non-overlapping. Using an equation to determine the diffusion layer thickness,[7] diffusion hemisphere radius was calculated to be approximately 27 µm at a scan rate of 10 mV/s. Figure 4.2(b) shows a rGO macroelectrode with classical peak shaped CV behavior; as can be seen in Figures 4.2(c) and 4.2(d), when the pitch spacing is increased from 30 to 60 µm, the depletion zone in the CV reduces and a classic sigmoidal shaped CV emerges as the sensors transit from macroelectrode to microelectrode behavior. At a spacing of 60 µm, the diffusion hemispheres of the individual microelectrodes cease to overlap as evidenced by the sigmoidal CV shape in Figure 4.2(d). This agrees with the calculation of the diffusion hemisphere radius being 27 µm. As long as the geometry for the rGO MEA has a pitch spacing larger than twice the diffusion layer radius, the device would operate in a microelectrode array regime. Subsequently all rGO MEAs were fabricated using 60 µm pitch spacings. Figure 4.2(e) shows an SEM image of the rGO active layer within a microelectrode as evidenced by the slight wrinkles that is characteristic of rGO. The image shows that rGO flakes remain stable within the microelectrode openings with no signs of lift off or peeling during electrochemical analysis.

4.3.2. rGO MEA Characterization

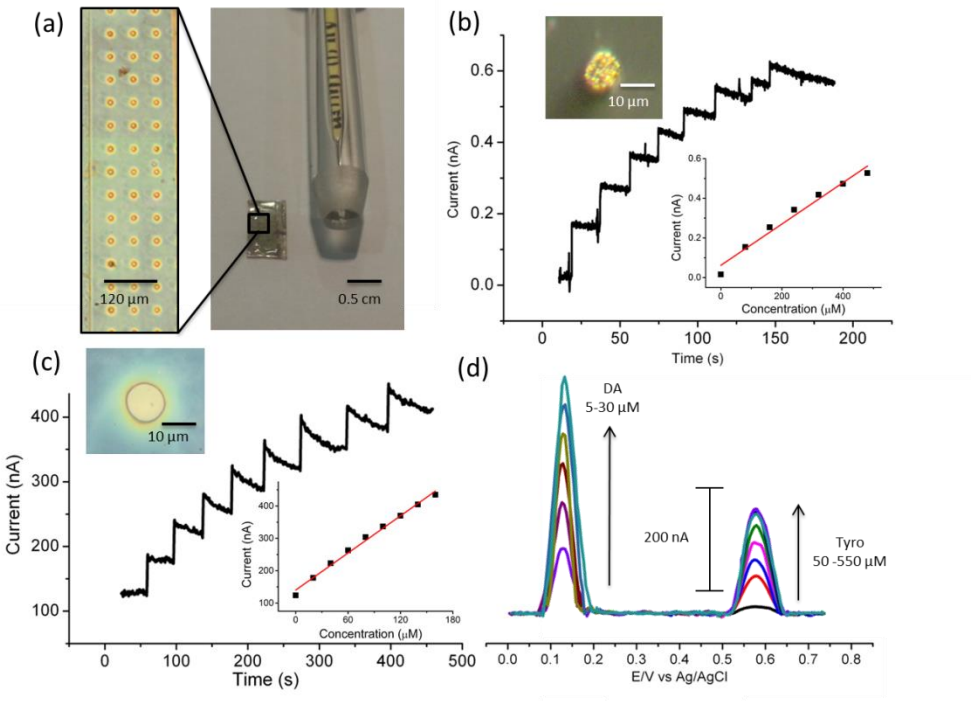

Figure 4.3. (a) Comparison of rGO MEA and Au microelectrode. Inset shows surface of rGO MEA with 10 µm microelectrode holes. (b) CA of Au microelectrode towards 100 µM injections of DA. Top inset shows image of gold active layer, bottom inset shows calibration graph. (c) CA of rGO MEA towards 20 µM injections of DA. Top inset shows single microelectrode and bottom inset shows calibration graph. (d) Simultaneous detection of DA and Tyrosine (Tyro) using DPV.

The electrochemical performance of a commercially available gold microelectrode (Metrohm) (Figure 4.3(a)) was compared to the rGO MEA device, using DA as the analyte. Irregular concentrations of DA, a neurotransmitter, is related to Parkinson's disease and attention deficit hyperactivity disorder and have been linked to other nervous system related diseases.[35–37] DA has been extensively reported to be electrochemically active towards metal and carbon based sensors including rGO.[38–45] At a potential of 0.14 V, DA undergoes a two electron-oxidation process, (one electron from each of its hydroxyl groups)[46] to the resulting in an anodic current that is

proportional to the concentration of DA in solution. Figure 4.3(b) shows CA response of the gold microelectrode towards 100 µM additions of DA, the gold microelectrode had a sensitivity of 0.001 nA μM^{-1} and a limit of detection of 3.6 µM (signal to noise ratio of 3). Figure 4.3(c) shows the CA response of the rGO MEA device towards addition of DA (20 µM). The rGO MEA device displays a sensitivity of 1.91 nA μM^{-1} with a detection limit of 0.26 µM (signal-to-noise ratio of 3). Normalising the sensitivities to account for the size of the active area gives 1.27×10^{-5} and 1.12×10^{-4} nA μM^{-1} μm^{-2} for the gold microelectrode and rGO MEA respectively. This is an increase of nearly an order of magnitude for rGO MEA.

The higher current signal in rGO MEA compared to gold microelectrode arises from the larger diffusion flux that is associated with the radial diffusion profile at its individual microelectrodes.[47] Using the CA data the sensitivity of the rGO MEA device was determined and compared with other graphene-based devices. From Table 4.1, it can be seen that the rGO MEA devices sensitivity is greater than other graphene based devices reported in the literature. It is also noted that the size of the active area is significantly smaller in our rGO MEA devices, and that no functionalization of the rGO layer has been performed, thus attesting to the fact that inherent sensitivity can be maintained even when the size is scaled down due to the enhanced diffusion flux of analytes in MEA geometry.

Sensor Type	Sensitivity (nA μM^{-1})	Active Area (mm^2)	Ref.
Glassy Carbon Electrode (GCE) with Copper Chloride Complex	2.02	7.1	[120]
Ferrocene bound Nafion Membrane Electrode	1.1	7.1	[121]
rGO with Gold Nanoparticles	0.0627	7.1	[122]
GCE with Carbon nanotubes/Chitosan Composite	0.328	7.1	[62]
Gold Microelectrode	0.001	0.0000785	This work.
rGOMEA	1.91	0.017	This work.

Table 4.1. Comparison of sensitivities of electrodes towards DA detection

Figure 4.3(d) shows simultaneous detection of Tyro and DA using DPV. Tyro is an amino precursor building block for DA. Simultaneous detection of DA and Tyro under physiological conditions could be potentially useful for diagnosis and health monitoring. It was noticed that the oxidation potential of Tyro at 0.59 V as recorded on rGO MEA is lower than the values obtained by previously reported graphene-based Tyro detection methods.[24,52] The regression equations of the peak DPV currents was i(nA) = 12.7DA_c (μM) + 75.2 and was i(nA) = 12.7$Tyro_c$ (μM) + 7.9. This shows the sensitivity of the rGO MEA devices towards DA and Tyro is 12.7 and 0.34 nA μM^{-1}, with a

detection limit of 0.1 µM and 3.7 µM (signal to noise ratio of 3), respectively. The rGO MEA was also used to detect hydrogen peroxide (Figure 4.4), where the device displays a sensitivity of 2.35 nA μM^{-1} with a detection limit of 0.35 µM (signal to noise ratio of 3).

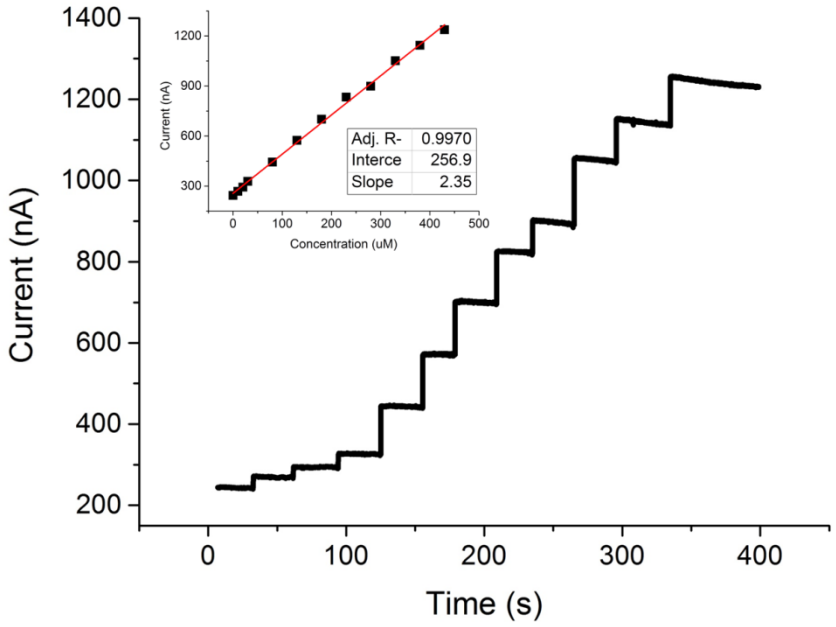

Figure 4.4. CA graph of hydrogen peroxide. 3 x 10 µM H_2O_2 injected followed by 8 x 50 µM injections. Inset calibration graph.

In physiological fluids, the solution conductivity is often low, thus it is important for a biosensor to retain its established electrocatalytic characteristics (sensitivities, point of oxidation/reduction) in these media. A 0.25 cm^2 rGO macroelectrode and rGO MEA device were comparatively tested using ruthenium hexamine as the redox analyte in 0.1M KCl and deionized water, the latter have conductivity of 12.9 mS cm^{-1} and 55 nS cm^{-1}, respectively.[53,54] As can be seen in Figure 4.5, the performance of the rGO MEA was largely unaffected in deionized water environments, the redox

peaks for ruthenium hexamine occurs at -0.1V and -0.2V, respectively. As scan rates increase, the peak-to-peak separation remains constant. This is due to the low ohmic drop associated with microelectrodes.[55] In contrast, macroelectrodes experience ohmic drop in solutions of low conductivity as the potential at the active layer of a macrolectrode lags the applied potential, this can cause significant inaccuracies in analyte detection since larger voltage sweep ranges need to be applied to account for the ohmic drop. Ohmic drop can be clearly seen in the increasing peak-to-peak separation distances in Figure 4.5(c) for the rGO macroelectrode in DI water. The peak-to-peak separation increases from 300 mV at 10 mV s^{-1} scan rate to 500 mV at a scan rate of 100 mV s^{-1}, which indicates extremely sluggish kinetics. In contrast, the peak-to-peak separation remains constant in rGO MEA with scan rate, thus the advantage of rGO MEAs is that it can operate robustly in electrolytes having conductivity differences of nearly 6 orders of magnitude.

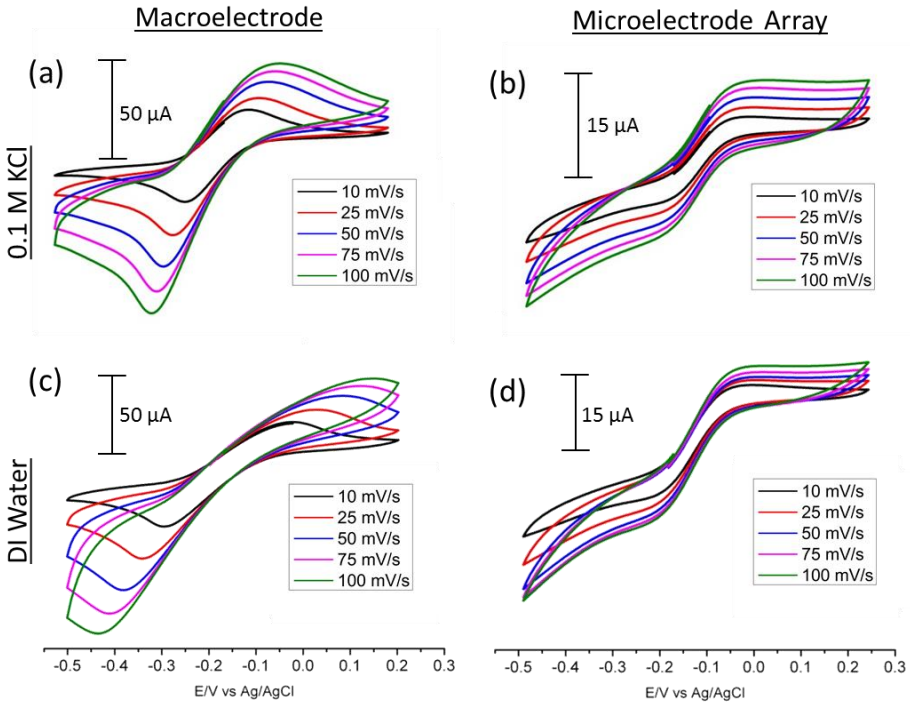

Figure 4.5. (a) CV of rGO macroelectrode in 0.1M KCl solution. (b) CV of rGO MEA in 0.1M KCl solution. (c) CV of rGO macroelectrode in DI water. (d) CV of rGO MEA in DI Water.

4.3.3. Microfluidic Integration

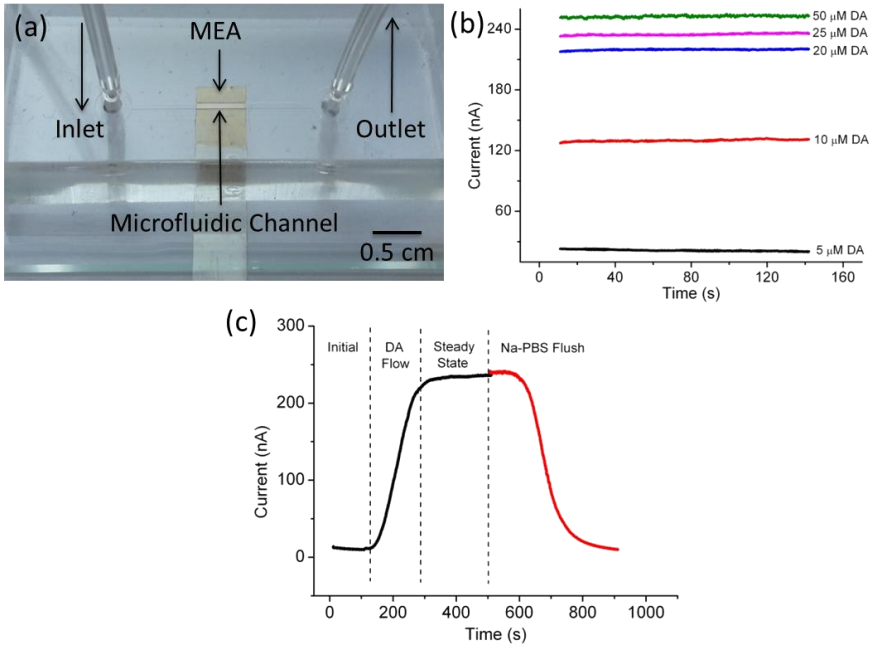

Figure 4.6. (a) Image of the rGO MEA device in the microfluidic system. (b) Steady state currents for differing concentrations of DA pumping through the microfluidic channel. (c) Example of CA response to the flowing of 25 μM DA and flushing with pure Na-PBS.

It has been reported that the operation of MEAs are relatively independent of solution flows.[56] The flat planar shape of the rGO MEA devices allows it to be readily integrated into a simple microfluidic system (Figure 4.6(a)) with a channel width of 500 μm and height of 100 μm. Solutions of 0.1M Na-PBS with differing concentrations of DA from 5 to 50 μM were injected into the channel and Figure 4.6(b) shows the steady state current response using CA. Figure 4.6(c) shows the signal response when DA flows through the system.

Flowing pure Na-PBS through the channel gave a steady state current of approximately 10 nA. Once a 25 μM DA stock solution flowed through the system, the steady state current increased to a value of 230 nA. After each run, the channel was flushed with pure NA-PBS solution. The red line depicts the signal returning to the baseline current once DA was flushed out. The highly reproducible flow sensing shows successful integration of the rGO MEA into a microfluidic system.

4.3.4. rGO MEA Cleaning

Fouling by biological solution is a common problem with biosensors. When increasing concentrations of AA was added, the DPV peak shifted to higher onset potentials and the anodic current decreased, which is evidence of surface fouling. The device could be readily cleaned in 0.1M Na-PBS by holding it at 0.6V for 3 minutes. At this potential the AA fouling was removed as AA was oxidized to L-dihydroascorbic acid which readily diffused away from the electroactive regions. (Figure 4.7) depicts the response of the cleaned device showing a similar response towards DA as compared to the pristine device before fouling.. This shows that the surface of the rGO electrode is relatively inert and only weak non-covalent bonding exists between biomolecules and the electrode surface.

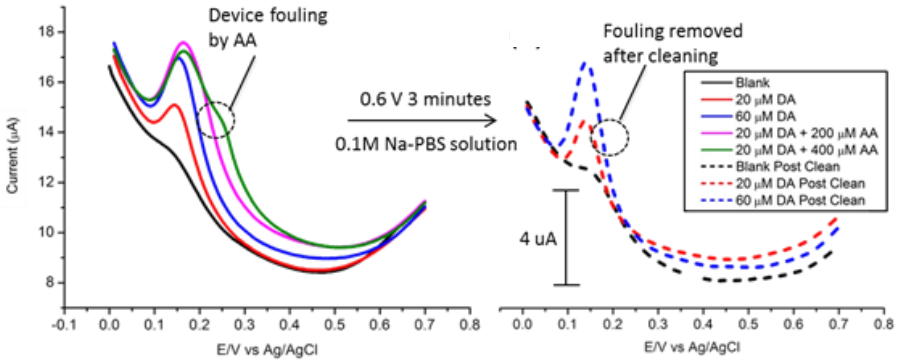

Figure 4.7. DPV spectra of rGO MEA device showing fouling caused by AA and after cleaning at 0.6 V in 0.1 M Na-PBS solution for 3 minutes the fouling is removed and the device performance is unchanged

4.3.5. Device Flexibility Characterization

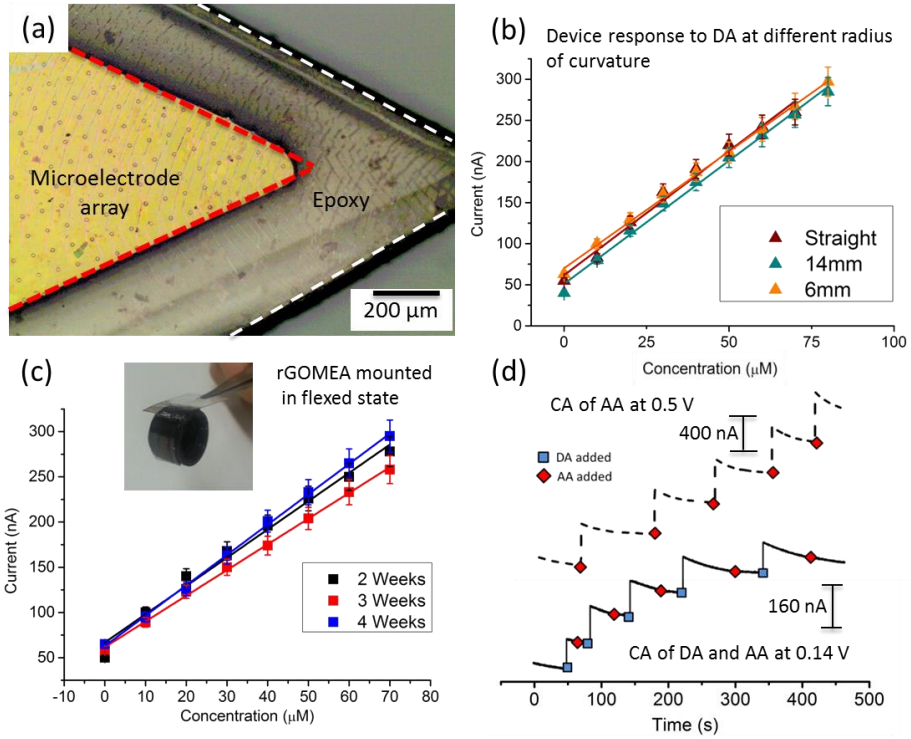

Figure 4.8. (a) rGO MEA device cut from ITO/PET substrate where it is fabricated on. (b) Comparison of rGO MEA performance towards DA when flexed at different radius of curvatures. (c) Flex tests of rGO MEA device over a span of 4 weeks, showing no change in device performance. (d) CA response graphs of rGO MEA device to AA at 0.5V (top) and DA in the presence of AA at 0.14V (bottom). At this potential the device shows selective response to DA.

The NIL fabrication process allows the microelectrode array to be fabricated across a large area on flexible substrates, after which any arbitrary size and shape of the devices active area can be cut from the original piece, this allows precise tailoring of the device dimensions to fit any given environment (Figure 4.8(a)). The mechanical flexibility of rGO is promising for flexible electronics.[57] The device performance in a flexed state towards DA detection was measured and compared to the performance in an unflexed state. The rGO MEA devices were mounted onto surfaces with radius of curvatures of 14 mm and 6 mm. The CA calibration graphs in Figure 4.8(b) shows negligible change in the device response to DA concentrations at increasing flex angles. The reliability of the sensor was tested using multiple sample runs (>15) of 10 μM DA injections and calculated the relative standard deviation to be 4.7%, which indicates good reliability .[48,58] In order to investigate if the rGO MEA remains operational when mechanically flexed, the rGO MEA was mounted on a curved surface of 6 mm radius of curvature (inset of Figure 4.8(b)) for an extended period of time. It was found that highly reproducible and stable current signals towards DA could be obtained from the device even after keeping the MEA in a continuous flexed state for 4 weeks (Figure 4.8(c)), showing that rGO is a suitable as an active layer for flexible sensor. This is attributed to the superior mechanical stability of rGO.

4.3.6. rGO MEA Selective Sensing

The rGO MEA electrode can also be operated in selective sensing mode. Figure 4.8(d) shows detection of DA with AA as an interferant. DA and AA have similar oxidizing potentials and could not be differentiated using DPV. However tuning the CA potential allows the selective detection of DA over AA. DA is more readily oxidized at the rGO surface due to its higher affinity to rGO arising from π-π stacking, as compared to AA which contains a pentene ring in its molecular structure.[59] The top CA graph in Figure 4.8(d) shows the detection of AA by the device at higher voltages (0.5V). The bottom CA graph shows consecutive DA and AA injection into the system at a voltage that allows for DA oxidation but not AA (0.14 V). As shown, the current increases (70 nA) only when DA is injected into the system whereas the increase in current when AA is injected is negligible (2 nA). Uric acid (UA) is also a common interferant however oxidation of UA only occurs at a higher potential (0.28 V) (Figure 4.9) in this case and therefore does not have any effect on DA detection when operated at a lowered potential of 0.14 V.

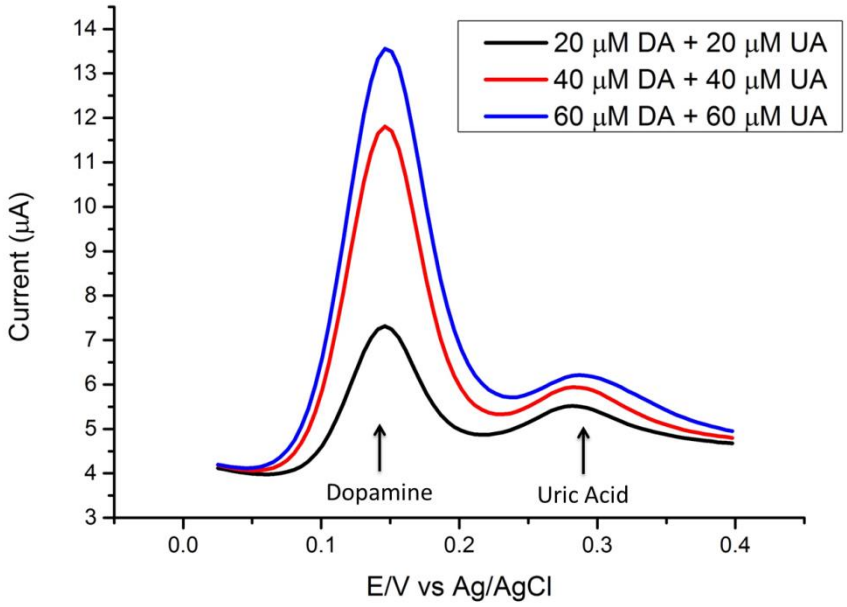

Figure 4.9. URIC acid DPV of DA and UA. DA oxidizes at 0.15 V while UA oxidizes at a higher potential of 0.28 V.

4.4. Conclusion

A microelectrode array sensor based on rGO has been successfully fabricated using NIL. The rGO MEA exhibits sigmoidal-shaped cyclic voltammetric response and high signal-to-noise ratio in the sensing of bioanalytes such as DA, Tyro and hydrogen peroxide. In the CA detection mode, rGO MEA exhibits a sensitivity of 1.91 nA μM^{-1} with a detection limit of 0.26 µM for DA and sensitivities of 2.3 nA μM^{-1} with a detection limit of 0.35 µM for hydrogen peroxide. Simultaneous detection of DA and Tyro using DPV yielded sensitivities of 12.7 and 0.34 nA μM^{-1}, with detection limits of 0.1 and 3.7 µM for DA and Tyro, respectively. The performance of the rGO MEAs is significantly higher than other macroscopic graphene electrodes in terms of sensitivity and tolerance for low conductivity electrolyte. Sensitivity was unaffected under a continuous flow condition when the rGO MEA was incorporated in a microfluidic device. Observing the rGO MEA being able to oxidise DA, UA and Tyro at differing potentials (0.14, 0.28 and 0.59 respectively) allows the possibility of an MEA device that can detect these three analytes simultaneously. Furthermore, the sensor shows remarkable mechanical stability and can be operated for an extended period of time in a flexed state.

4.5. References

1. Montenegro, M. I., Montenegro, I., Queirós, M. A. & Daschbach, J. L. *Microelectrodes: Theory and Applications: Theory and Applications*. (Kluwer Academic Publishers, 1991).

2. Huang, X.-J., O'Mahony, A. M. & Compton, R. G. Microelectrode Arrays for Electrochemistry: Approaches to Fabrication. *Small* **5,** 776–788 (2009).

3. Stern, E., Jay, S., Bertram, J., Boese, B., Kretzschmar, I., Turner-Evans, D., Dietz, C., LaVan, D. A., Malinski, T., Fahmy, T. & Reed, M. A. Electropolymerization on microelectrodes: functionalization technique for selective protein and DNA conjugation. *Anal. Chem.* **78,** 6340–6346 (2006).

4. Walcarius, A., Minteer, S. D., Wang, J., Lin, Y. & Merkoçi, A. Nanomaterials for bio-functionalized electrodes: recent trends. *J. Mater. Chem. B* **1,** 4878–4908 (2013).

5. Bard, A. J. & Faulkner, L. R. *Electrochemical Methods: Fundamentals and Applications*. (Wiley, 2000).

6. Henstridge, M. C. & Compton, R. G. Mass transport to micro- and nanoelectrodes and their arrays: a review. *Chem. Rec. N. Y. N* **12,** 63–71 (2012).

7. Tomčík, P. Microelectrode Arrays with Overlapped Diffusion Layers as Electroanalytical Detectors: Theory and Basic Applications. *Sensors* **13,** 13659–13684 (2013).

8. Finklea, H. O., Snider, D. A., Fedyk, J., Sabatani, E., Gafni, Y. & Rubinstein, I. Characterization of octadecanethiol-coated gold electrodes as microarray electrodes by cyclic voltammetry and ac impedance spectroscopy. *Langmuir* **9,** 3660–3667 (1993).

9. Jung, S.-K. & Wilson, G. S. Polymeric Mercaptosilane-Modified Platinum Electrodes for Elimination of Interferants in Glucose Biosensors. *Anal. Chem.* **68,** 591–596 (1996).

10. Lupu, S., Lete, C., Marin, M., Totir, N. & Balaure, P. C. Electrochemical sensors based on platinum electrodes modified with hybrid inorganic–organic coatings for determination of 4-nitrophenol and dopamine. *Electrochimica Acta* **54,** 1932–1938 (2009).

11. Lian, W., Wang, L., Song, Y., Yuan, H., Zhao, S., Li, P. & Chen, L. A hydrogen peroxide sensor based on electrochemically roughened silver electrodes. *Electrochimica Acta* **54,** 4334–4339 (2009).

12. Reed, D. E. & Hawkridge, F. M. Direct electron transfer reactions of cytochrome c at silver electrodes. *Anal. Chem.* **59,** 2334–2339 (1987).

13. Pron, A., Gawrys, P., Zagorska, M., Djurado, D. & Demadrille, R. Electroactive materials for organic electronics: preparation strategies,

structural aspects and characterization techniques. *Chem. Soc. Rev.* **39,** 2577 (2010).

14. Hsiao, Y.-S., Kuo, C.-W. & Chen, P. Multifunctional Graphene–PEDOT Microelectrodes for On-Chip Manipulation of Human Mesenchymal Stem Cells. *Adv. Funct. Mater.* **37**, 4649-4656 (2013).

15. Huang, K.-J., Wang, L., Li, J., Yu, M. & Liu, Y.-M. Electrochemical sensing of catechol using a glassy carbon electrode modified with a composite made from silver nanoparticles, polydopamine, and graphene. *Microchim. Acta* **180,** 751–757 (2013).

16. Chopra, S., McGuire, K., Gothard, N., Rao, A. M. & Pham, A. Selective gas detection using a carbon nanotube sensor. *Appl. Phys. Lett.* **83,** 2280–2282 (2003).

17. Yuan, W. & Shi, G. Graphene-based gas sensors. *J. Mater. Chem. A* **1,** 10078–10091 (2013).

18. Forrest, S. R. & Thompson, M. E. Introduction: Organic Electronics and Optoelectronics. *Chem. Rev.* **107,** 923–925 (2007).

19. Chua, C. K. & Pumera, M. Chemical reduction of graphene oxide: a synthetic chemistry viewpoint. *Chem. Soc. Rev.* **43,** 291–312 (2013).

20. Ng, A. M. H., Wang, Y., Lee, W. C., Lim, C. T., Loh, K. P. & Low, H. Y. Patterning of graphene with tunable size and shape for microelectrode array devices. *Carbon* **67,** 390–397 (2014).

21. Chen, N., Li, X., Wang, X., Yu, J., Wang, J., Tang, Z. & Akbar, S. A. Enhanced room temperature sensing of Co3O4-intercalated reduced graphene oxide based gas sensors. *Sens. Actuators B Chem.* **188,** 902–908 (2013).

22. Penmatsa, V., Kim, T., Beidaghi, M., Kawarada, H., Gu, L., Wang, Z. & Wang, C. Three-dimensional graphene nanosheet encrusted carbon micropillar arrays for electrochemical sensing. *Nanoscale* **4,** 3673 (2012).

23. Cai, B., Wang, S., Huang, L., Ning, Y., Zhang, Z. & Zhang, G.-J. Ultrasensitive Label-Free Detection of PNA–DNA Hybridization by Reduced Graphene Oxide Field-Effect Transistor Biosensor. *ACS Nano* **8,** 2632–2638 (2014).

24. Wei, J., Qiu, J., Li, L., Ren, L., Zhang, X., Chaudhuri, J. & Wang, S. A reduced graphene oxide based electrochemical biosensor for tyrosine detection. *Nanotechnology* **23,** 335707 (2012).

25. Li, W., Geng, X., Guo, Y., Rong, J., Gong, Y., Wu, L., Zhang, X., Li, P., Xu, J., Cheng, G., Sun, M. & Liu, L. Reduced Graphene Oxide Electrically Contacted Graphene Sensor for Highly Sensitive Nitric Oxide Detection. *ACS Nano* **5,** 6955–6961 (2011).

26. Wang, J., Li, M., Shi, Z., Li, N. & Gu, Z. Electrocatalytic Oxidation of Norepinephrine at a Glassy Carbon Electrode Modified with Single Wall Carbon Nanotubes. *Electroanalysis* **14,** 225–230 (2002).

27. Saby, C., Ortiz, B., Champagne, G. Y. & Bélanger, D. Electrochemical Modification of Glassy Carbon Electrode Using Aromatic Diazonium Salts. 1. Blocking Effect of 4-Nitrophenyl and 4-Carboxyphenyl Groups. *Langmuir* **13,** 6805–6813 (1997).

28. Wu, S., He, Q., Tan, C., Wang, Y. & Zhang, H. Graphene-Based Electrochemical Sensors. *Small* **9,** 1160–1172 (2013).

29. Frazier, A.B., O'Brien, D.P. & Allen, M.G. Two Dimensional Metallic Microelectrode Arrays for Extracellular Stimulationa nd Recording of Neurons. *IEEE* (1993).

30. Li, F., Xue, M., Ma, X., Zhang, M. & Cao, T. Facile patterning of reduced graphene oxide film into microelectrode array for highly sensitive sensing. *Anal. Chem.* **83,** 6426–6430 (2011).

31. He, Q., Sudibya, H. G., Yin, Z., Wu, S., Li, H., Boey, F., Huang, W., Chen, P. & Zhang, H. Centimeter-Long and Large-Scale Micropatterns of Reduced Graphene Oxide Films: Fabrication and Sensing Applications. *ACS Nano* **4,** 3201–3208 (2010).

32. Chou, S. Y., Krauss, P. R. & Renstrom, P. J. Nanoimprint lithography. *J. Vac. Sci. Technol. B* **14,** 4129–4133 (1996).

33. Guo, L. J. Nanoimprint Lithography: Methods and Material Requirements. *Adv. Mater.* **19,** 495–513 (2007).

34. Toh, S. Y., Loh, K. S., Kamarudin, S. K. & Daud, W. R. W. Graphene production via electrochemical reduction of graphene oxide: Synthesis and characterisation. *Chem. Eng. J.* **251,** 422–434 (2014).

35. Bernheimer, H., Birkmayer, W., Hornykiewicz, O., Jellinger, K. & Seitelberger, F. Brain dopamine and the syndromes of Parkinson and Huntington Clinical, morphological and neurochemical correlations. *J. Neurol. Sci.* **20,** 415–455 (1973).

36. Contreras, F., Fouillioux, C., Bolívar, A., Simonovis, N., Hernandez, R., Hernandez, M. J., Lezama, E. & Velasco, M. Dopamine, hypertension and obesity. *Int. Congr. Ser.* **1237,** 99–107 (2002).

37. Gj, L., Jm, S., Sb, W., C, G., T, W., N, K. & Jl, K. Dopamine D4 receptor gene polymorphism is associated with attention deficit hyperactivity disorder. *Mol. Psychiatry* **1,** 121–124 (1996).

38. Barnes, E. O., O'Mahony, A. M., Aldous, L., Hardacre, C. & Compton, R. G. The electrochemical oxidation of catechol and dopamine on platinum in 1-Ethyl-3-methylimidazolium bis(trifluoromethylsulfonyl)imide ([C2mim][NTf2]) and 1-Butyl-3-methylimidazolium tetrafluoroborate

([C4mim][BF4]): Adsorption effects in ionic liquid voltammetry. *J. Electroanal. Chem.* **646,** 11–17 (2010).

39. Gai, P., Zhang, H., Zhang, Y., Liu, W., Zhu, G., Zhang, X. & Chen, J. Simultaneous electrochemical detection of ascorbic acid, dopamine and uric acid based on nitrogen doped porous carbon nanopolyhedra. *J. Mater. Chem. B* **1,** 2742–2749 (2013).

40. Hubbard, A. T., Stickney, J. L., Soriaga, M. P., Chia, V. K. F., Rosasco, S. D., Schardt, B. C., Solomun, T., Song, D., White, J. H. & Wieckohski, A. Electrochemical processes at well-defined surfaces. *J. Electroanal. Chem. Interfacial Electrochem.* **168,** 43–66 (1984).

41. Yang-Rae Kim, S. B. Electrochemical detection of dopamine in the presence of ascorbic acid using graphene modified electrodes. *Biosens. Bioelectron.* **25,** 2366–2369 (2010).

42. Yu, X., Sheng, K. & Shi, G. A three-dimensional interpenetrating electrode of reduced graphene oxide for selective detection of dopamine. *Analyst* **139,** 4525–4531 (2014).

43. Zachek, M. K., Hermans, A., Wightman, R. M. & McCarty, G. S. Electrochemical Dopamine Detection: Comparing Gold and Carbon Fiber Microelectrodes using Background Subtracted Fast Scan Cyclic Voltammetry. *J. Electroanal. Chem. Lausanne Switz.* **614,** 113–120 (2008).

44. Zhu, W., Chen, T., Ma, X., Ma, H. & Chen, S. Highly sensitive and selective detection of dopamine based on hollow gold nanoparticles-graphene nanocomposite modified electrode. *Colloids Surf. B Biointerfaces* **111,** 321–326 (2013).

45. Zhu, X., Liu, Q., Zhu, X., Li, C., Xu, M. & Liang, Y. Reduction of graphene oxide via ascorbic acid and its application for simultaneous detection of dopamine and ascorbic acid. *Int J Electrochem Sci* **7,** 5172–5184 (2012).

46. Colin-Orozco, E., Corona-Avendano, S., Ramirez-Silva, M. T., Romero-Romo, M. & Palomar-Pardave, M. On the Electrochemical Oxidation of Dopamine, Ascorbic Acid and Uric Acid onto a Bare Carbon Paste Electrode from a 0.1 M NaCl Aqueous Solution at pH 7. *Int. J. Electrochem. Sci.* **7,** 6097–6105 (2012).

47. Zoski, C. G. *Handbook of Electrochemistry*. (Elsevier, 2007).

48. Sotomayor, M. D. P. T., Tanaka, A. A. & Kubota, L. T. Development of an Amperometric Sensor Highly Selective For Dopamine and Analogous Compounds Determination Using Bis(2,2′-Bipyridil) Copper(II) Chloride Complex. *Electroanalysis* **15,** 787–796 (2003).

49. Kumar, A. S., Swetha, P. & Pillai, K. C. Enzyme-less and selective electrochemical sensing of catechol and dopamine using ferrocene bound Nafion membrane modified electrode. *Anal. Methods* **2,** 1962 (2010).

50. Yang, J., Strickler, J. R. & Gunasekaran, S. Indium tin oxide-coated glass modified with reduced graphene oxide sheets and gold nanoparticles as disposable working electrodes for dopamine sensing in meat samples. *Nanoscale* **4,** 4594–4602 (2012).

51. Babaei, A., Babazadeh, M. & Momeni, H. R. A Sensor for Simultaneous Determination of Dopamine and Morphine in Biological Samples Using a Multi-Walled Carbon Nanotube/Chitosan Composite Modified Glassy Carbon Electrode. *Int J Electrochem Sci* **6,** 1382–1395 (2011).

52. Xiaozhi Yu, Z. M. Electrochemical Behavior and Determination of L-Tyrosine at Single-walled Carbon Nanotubes Modified Glassy Carbon Electrode. *Electroanalysis* **20,** 1246 – 1251 (2008).

53. Pratt, K. W. Proposed new electrolytic conductivity primary standards for KCl solutions. *J Res Natl Inst Stand Technol* **96,** 191 (1991).

54. Pashley, R. M., Rzechowicz, M., Pashley, L. R. & Francis, M. J. De-gassed water is a better cleaning agent. *J. Phys. Chem. B* **109,** 1231–1238 (2005).

55. Aoki, K. Theory of ultramicroelectrodes. *Electroanalysis* **5,** 627–639 (1993).

56. Fungaro, D. A. & Brett, C. M. A. Microelectrode arrays: application in batch-injection analysis. *Anal. Chim. Acta* **385,** 257–264 (1999).

57. Cong, H.-P., Ren, X.-C., Wang, P. & Yu, S.-H. Flexible graphene–polyaniline composite paper for high-performance supercapacitor. *Energy Environ. Sci.* **6,** 1185–1191 (2013).

58. Mao, Y., Bao, Y., Gan, S., Li, F. & Niu, L. Electrochemical sensor for dopamine based on a novel graphene-molecular imprinted polymers composite recognition element. *Biosens. Bioelectron.* **28,** 291–297 (2011).

59. Gao, F., Cai, X., Wang, X., Gao, C., Liu, S., Gao, F. & Wang, Q. Highly sensitive and selective detection of dopamine in the presence of ascorbic acid at graphene oxide modified electrode. *Sens. Actuators B Chem.* **186,** 380–387 (2013).

Chapter 5. Reduced graphene oxide microelectrode array design optimization

Abstract

Microelectrode array (MEA) design requires a balance between including as many active microelectrodes on the device to increase signal output without their respective diffusion hemispheres overlapping. If overlap occurs, the MEA can revert back to macroelectrode behavior, compromising the advantageous MEA characteristics of higher signal to noise ratios, operation in highly resistive media, lower limits of detection and greater signal stability in flowing environments. Therefore, determining the optimum density of an MEA is crucial to its performance. In this chapter the optimum interelectrode spacing for reduced graphene oxide based microelectrode arrays (rGO MEA) was investigated at a slow scan rate of 5 mV/s with 9 µm and 10 µm diameter microelectrodes. The optimum separation distance was found to be 15.7 times the radius of the microelectrode to allow the device to operate in an MEA regime.

5.1. Introduction

Microelectrodes have been extensively reported to have superior detection and performance characteristics over conventional macroelectrodes. Observed properties such as higher diffusion flux, greater signal to noise ratios, lower detection limits, operation in highly resistive media, greater signal stability in flowing environments and smaller footprint sizes allowing microelectrodes to be used in small environments have generated much interest in microelectrode sensors.[1–5]

However, a significant problem when using microelectrodes, are signals detected falling within the micro to nanoamp range. Faradaic currents created by electron transfer from and to the target analyte is related to the size of the active layer at which these reactions can occur.[2] As the active area of microelectrodes are small; this results in proportionally small currents. These small currents are susceptible to interference and can be dominated by the inherent system noise, requiring expensive noise filtering instruments to operate the microelectrode with accuracy and precision.[1]

The alternative to decreasing the interference is to increase the current output. The predominant method to increase these signal currents is to fabricate the microelectrode into an array configuration. In an MEA, multiple microelectrodes on the same device act in parallel to generate a current that is equal to the sum of the number of microelectrodes in the array, resulting in higher current outputs while still retaining the advantageous characteristics of a microelectrode.[6,7]

However, considerations need to be taken into account when designing the location of the individual microelectrode active areas relative to each other. Although intuitively it would seem optimal to fabricate as many microelectrodes on the surface as possible, there is a limit to the microelectrode density in an array if microelectrode behavior is desired.

Conventional electrodes have a planar diffusion layer that grows with time, perpendicular to the electrode surface. This is caused by the analyte concentration gradient that is approximately zero at the surface of the electroactive layer and increases towards the bulk concentration as the distance increases from the working electrode surface.[8,9] The presence of the concentration gradient induces diffusion of the analyte material from the bulk solution towards the region of lower concentration (electrode surface). This diffusion process is described by Fick's Law and is always linear.[5,10] This results in the characteristic peak shaped cyclic voltammograms that has been explained in section 1.4.1 of the introduction chapter.

When using a microelectrode, the diffusion layer takes on a different form. As the electroactive area has dimensions in the micron scale, diffusion of the analyte from the sides becomes possible, whereas in a macroelectrode, the diffusion from the edge of the electrode is negligible when compared to the area of the working surface. This results in microelectrode diffusion layers that take on a hemispherical shape.[1] This hemispherical shape allows for a greater flux of analyte towards the electroactive layer whereby diffusion of the analyte and electron transfer are in equilibrium. Consequently the cyclic voltammetry (CV) spectra of a microelectrode takes on a sigmoidal shape where a steady state current is reached as opposed to the formation of

depletion zones.[5] CV can therefore be used to determine when a device is behaving as an MEA. If there is a depletion zone, this means the diffusion hemispheres are overlapping, which would require an increase in interelectrode spacing.

Both planar and hemispherical diffusion layer sizes are affected by the diffusion coefficient of the analyte and the scan speed used. Slow scan rates allow for more time for the diffusion layer to increase in radius, resulting in larger diffusion hemispheres. Conversely faster scan rates results in smaller diffusion hemispheres.[11]

Since the side diffusion of analytes towards a microelectrode is critical to its performance, overlapping of the hemispheres in a microelectrode array must be avoided. Therein lies a significant problem with MEA fabrication.

There have been many reports about MEA geometries that take into account hexagonal or square lattice MEA arrangements, and co planar and shallow recessed MEAs.[13,14] The authors fitted their theoretical simulations to experimental data and found to them be in reasonable agreement within the papers themselves. However, many of these reports do not agree with each other and the concluding minimum interelectrode distance for metal based MEA behavior to occur varies between papers.

For example, Horne et al. determined that interelectrode spacing could be loosely bound by the size of the electrode and should be 20 times greater than the radius of the microelectrode.[13] Other groups such as Compton et al. proposed that the minimum distance for MEA behavior can be determined by the use of the scan rate, the electron transfer properties of the electroactive

material and the diffusion coefficient of the analyte.[15] Further, Aoki et al. proposed a formula to take into account the size of the microelectrode, scan speed, electron transfer properties and diffusion coefficient of the analyte.[1] Another group Guo et al. proposed a formula that relied only on the size of the microelectrode and the recessed depth.[14] Using the formulae found in the above reports, coupled with the experimental data within this chapter of the scan speed used, diffusion coefficient of ruthenium (III) hexamine concentration, transfer kinetics and microelectrode size, the minimum distances according to these respective formulae can be seen in Table 5.1.

Group	**Theoretical equation for microelectrode separation distance**	**Theoretical microelectrode separation distance (μm)**
Horne et al.	$20r$	100
Compton et al.	$2\sqrt{(2D\frac{\Delta E}{v})}$	52
Aoki et al.	$\frac{2r}{\frac{1}{\sqrt{\pi}\frac{Dt}{2r^2}} + 0.97 - 1.10\exp(\frac{-9.90}{\ln(12.37(\frac{Dt}{2r^2})}}$	58
Guo et al.	$10.86 + 6.218\exp\left(-\frac{L+0.0888}{0.222}\right) + 9.435\exp(-\frac{L+0.0888}{0.492})$	93

Table 5.1. Comparison of theoretical formulae and resulting values of minimum separation distances between microelectrodes for MEA behaviour to occur. *r* is the radius of the microelectrode (5 μm), *D* is the diffusion coefficient of the analyte (9.1 x 10^{-6} cm^2 s^{-1}), *v* is the scan rate (5 mV s^{-1}), t is the time of the experiment (37 s), ΔE is the peak to peak separation (0.185 V) and *L* is the recess depth over the radius of the microelectrode (0.8/5).

As can be seen, the resulting theoretical separation distances can vary widely and shows that current simulation techniques may be ignoring certain

variables that have not yet been taken into account and at best, close theoretical approximations have to be settled for. Of course, it is possible to fabricate an MEA that has extremely large separation distances to prevent any chance of diffusion hemisphere overlap. However, this would significantly reduce the performance of the electrode in output current as there would be fewer microelectrode active areas.

As previously stated, diffusion of the analyte and electron transfer to the electrode determines whether a device operates in the microelectrode regime. The electroactive material therefore also has an effect on this window of microelectrode operation. Currently to our best knowledge, all simulations and MEA investigations have been in regards to metal based electroactive layers. No studies have been conducted on rGO MEAs.

rGO's electrical properties make it an ideal candidate for sensor applications and there is a growing research thrust to use graphene based active materials in electrochemical sensors.[16,17] An area of graphene sensing that still has seen little research, is graphene in a microelectrode array format. The reason being that rGO MEA fabrication has been a difficult task with conventional MEA fabrication techniques as described in previous chapters.

To the best of our knowledge the only other report on graphene based MEAs has been by Li et al. in 2011.[18] They report MEA fabrication by coating an indium tin oxide (ITO) substrate with GO. GO is intrinsically insulating so they would selectively reduce periodic parts of the GO layer using a stamping technique with a polydimethylsiloxane (PDMS) well, filled with hydrazine. The areas of the GO layer that came into contact with the hydrazine wells

would be reduced, producing rGO active areas in a periodic fashion and give rise to MEA characteristics.

There are several limitations with this method. Firstly, hydrazine is a highly toxic substance. The stamping procedure also presents reduced areas that are not well defined and any accidental shift of the PDMS layer will cause smearing of the hydrazine and reduce a larger area of GO. Lastly, the GO regions, which are at first insulating, will become active as electrochemical experiments are carried out, which would result in the loss of MEA characteristics.

Although graphene shows good promise to be used in an MEA configuration, no studies have looked into the optimal microelectrode spacings for graphene-based MEAs. Elucidating this minimum separation distance would establish a guide rule for future graphene-based MEA research.

5.2. Materials and Methods

5.2.1. Chemicals

Graphene oxide solution was purchased from Graphenea Inc.

Indium Tin Oxide/Polyethylene Terephthalate (ITO/PET) and Ruthenium (III) Hexamine was purchased from Sigma Aldrich Co.

5.2.2. GO deposition and reduction

2 mg/ml GO solution was spin coated onto ITO/PET at 2000 rpm for 30 seconds. The substrate was then immersed in 0.1 M sodium phosphate buffer saline (Na-PBS) solution pH 4.5. Chronoamperometry was used and held at -0.9V for 2 minutes to reduce the GO.

5.2.3. MEA Fabrication

An MA8 mask aligner was used with AZ 1505 as the resist type to fabricate the MEAs with differing electrode spacings. AZ1505 was spin coated onto the substrate at 3000 rpm for 1 minute. The sample was soft baked at 100^{o}C for 1 minute. The sample was then exposed to 15 seconds of UV light and then placed in a beaker of the photodeveloper at 1:1 ratio of DI water.

The sample was agitated in the photodeveloper for 25 seconds after which it was rinsed with DI water and placed on a 100^{o}C hot plate for 1 minute to dry.

5.2.4. Electrochemical Experiments

A three probe setup was used for electrochemical experiments. Cyclic Voltammetry (CV) was used by attaching the MEA to the working electrode, a platinum mesh as the counter electrode and an Ag/AgCl reference electrode using Ruthenium (III) hexamine as the redox probe.

5.3. Results and Discussion

5.3.1. MEA Characterization

Two series of rGO MEAs were fabricated to determine the optimum separation distances.

According to the equation found in the work of Aoki et al. the ratio of the electrode separation distance (E_d) to the radius of the microelectrode (E_r) would change depending on the size of the microelectrode (Figure 5.1). As the microelectrode radius decreases, the ratio required for separation exponentially increases. This means that there is not one ratio of microelectrode separation that can apply across all MEA radiuses. For instance, a microelectrode of radius 5 µm has a separation ratio of 12.4 whereas a microelectrode of radius 0.5 µm has a ratio of 16. Once the array moves to nanoelectrode regimes, this ratio increases to 25.2 for a 5 nm radius nanoelectrode.

10 and 9 µm diameter MEAs were chosen since the previous chapters were based on 10 µm diameter MEAs, and 9 µm was chosen to ensure that theoretically the E_d/E_r ratio would be similar.

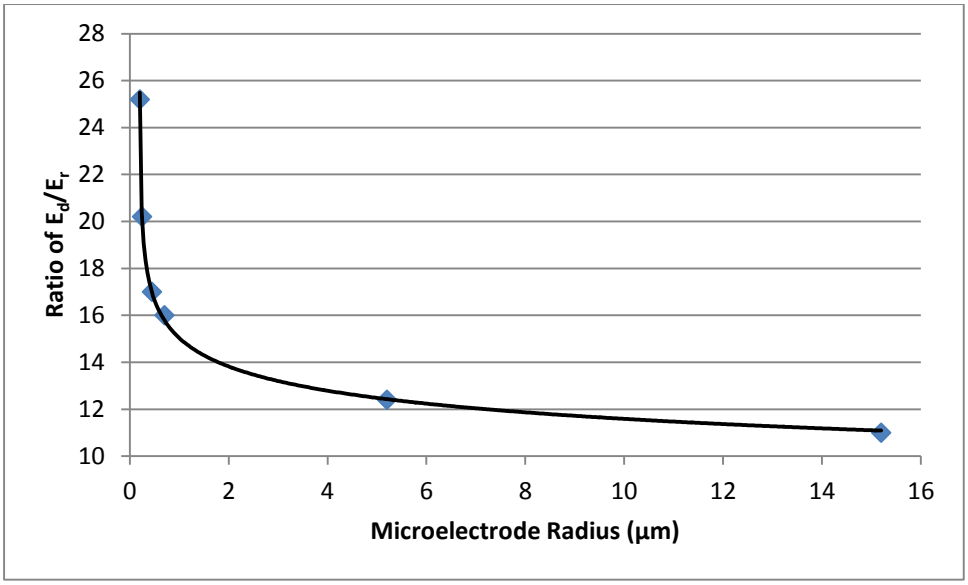

Figure 5.1. Graph of ratio of diffusion layer and microelectrode radius showing exponential increase in separation ratios as electrode diameter decreases.

It is crucial to ensure the fabrication process produced MEAs of the desired microelectrode diameters and interelectrode spacings. rGO MEAs of interelectrode spacings 30, 60, 80 and 120 µm were first fabricated to determine at which point MEA behavior would occur (Appendix B). The data resulted in MEA behavior around the 60 µm range. In order to increase the precision of determining the minimum pitch spacing for MEA behavior 60, 64, 68 and 70 µm were fabricated with 9 and 10 µm microelectrode diameters. These dimensions were measured by SEM.

Figure 5.2 are some images of the dimension verification process using 68 µm interelectrode spacing rGO MEAs with 9 and 10 µm diameter microelectrodes. As can be seen in the SEM images, the fabrication process produced the targeted dimensions of the MEAs.

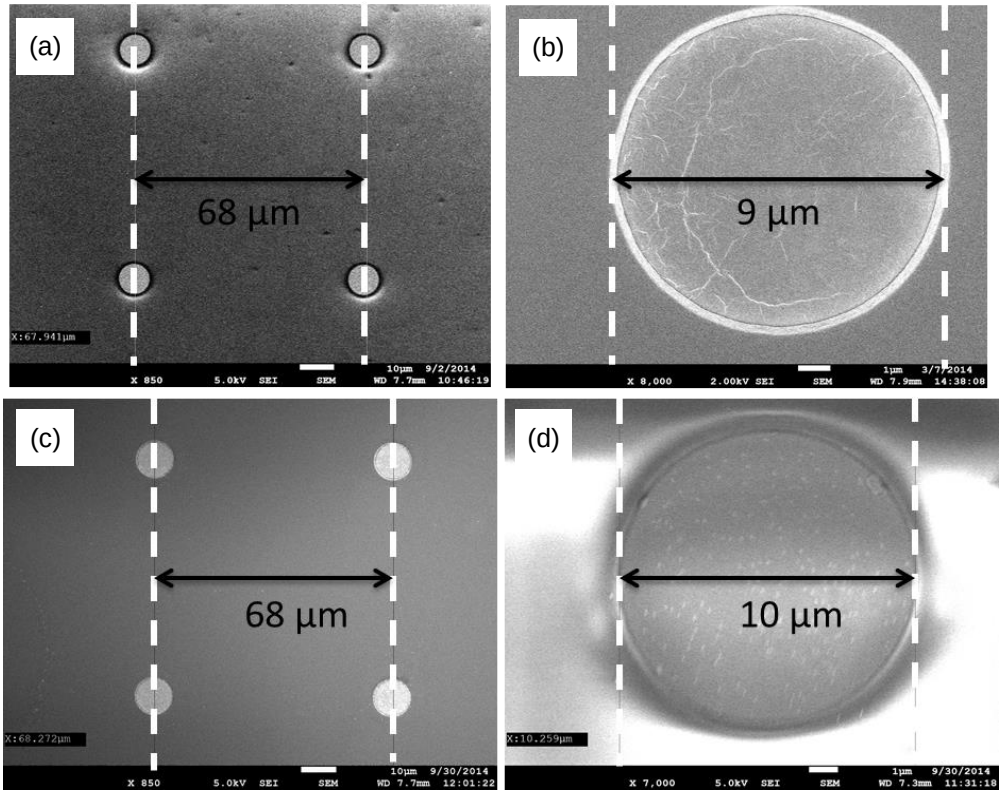

Figure 5.2. SEM images of MEA surfaces. (a) Interelectrode distance for 9 µm series. (b) Diameter of single 9 µm microelectrode. (c) Interelectrode distance for 10 µm microelectrode series. (d) Diameter of single 10 µm microelectrode.

Guo et al. reports that the depth of the microelectrode recess can have an impact on the size of the diffusion hemisphere if the depth to electrode diameter ratio is large. Generally, as the ratio of the recess depth to the electrode diameter increases, so too would the time for the diffusion hemisphere require to expand out of the recess into the bulk solution.[14] This dynamic sounds favorable since it would reduce the likelihood of diffusion hemisphere overlap, however if the recess is too deep then as the diffusion layer expands, it will eventually be bound by the recess side walls. The

individual microelectrodes will then start to behave as a macroelectrode resulting in peak-shaped voltommagrams.[14]

AFM imaging showed the resist layer to be approximately 800 nm thick (Figure 5.3) which is also equivalent to the recess depth. Giving $L = 0.8/10 = 0.08$. At this low ratio, the recess depth is relatively negligible in affecting the diffusion hemisphere size.

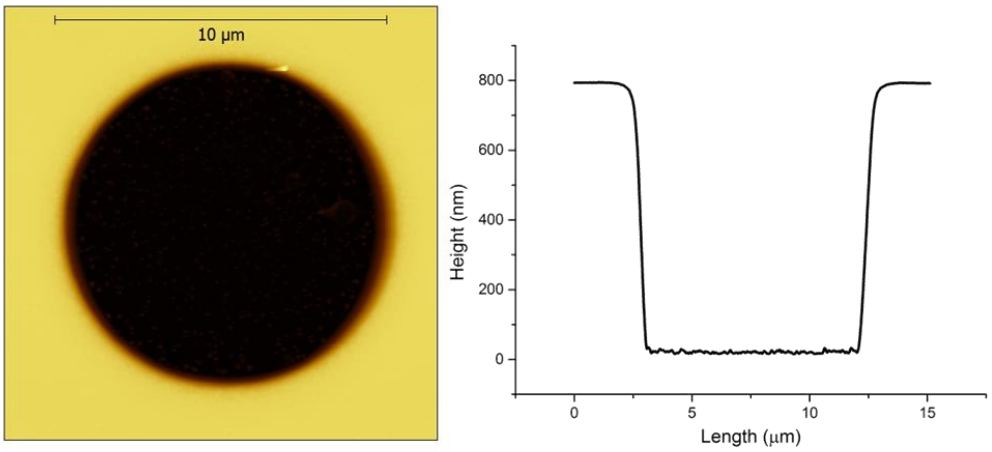

Figure 5.3. AFM imaging of single microelectrode hole with step height profile showing 800 nm thick insulating layer.

5.3.2. Characterization using CV

The advantageous properties of microelectrodes arise when the mass diffusion of the target analyte to the electrode is equivalent to the transfer of electrons from the analyte to the active layer.[1] This results in a steady state current which registers on the CV spectra as a sigmoidal shape. Taking cues from the work reported by Guo et al., the steady state current is bounded by the peak current and the current at the reverse scan. Ideally, there is no depletion and the peak current and the reverse scan current are the same. In their work they

report a criterion of no more than a 5% depletion tolerance as an acceptable limit for microelectrode behavior.[14] In this chapter a stricter criterion of a 3% depletion tolerance was used.

The other variable that affects MEA behavior is the operating scan rate. Gou et al. reported that for a given interelectrode spacing, there is no true microelectrode behavior across all scan rates. This is because at very long MEA operating times, the diffusion hemisphere can expand far into the bulk solution and eventually overlap with adjacent diffusion hemispheres.[14] In order to set a reasonable upper bound on the size of a diffusion hemisphere, a slow scan speed of 5 mV/s was used to determine the optimal interelectrode spacing of an rGO MEA. Typical CV scan rates fall in between the 20 – 40 mV/s range and so a 5 mV/s speed to determine MEA behavior would be applicable to common operating regimes.

5.3.2.1. Depletion of rGO Macroelectrode

The depletion zone of a 0.25 cm^2 rGO macroelectrode was investigated as a baseline reference for CV experiments. Figure 5.4 shows the rGO macroelectrode CV spectra with a clear peak-shaped voltammogram. As the voltage sweeps to values beyond the redox peak, the current drops off significantly. The drop in this case was 43% of the peak current at 10 mV/s and 48% at 100 mV/s. Since rGO behaves like a conventional electroactive layer, any MEA behavior seen can be attributed solely to the geometry of the fabricated array.

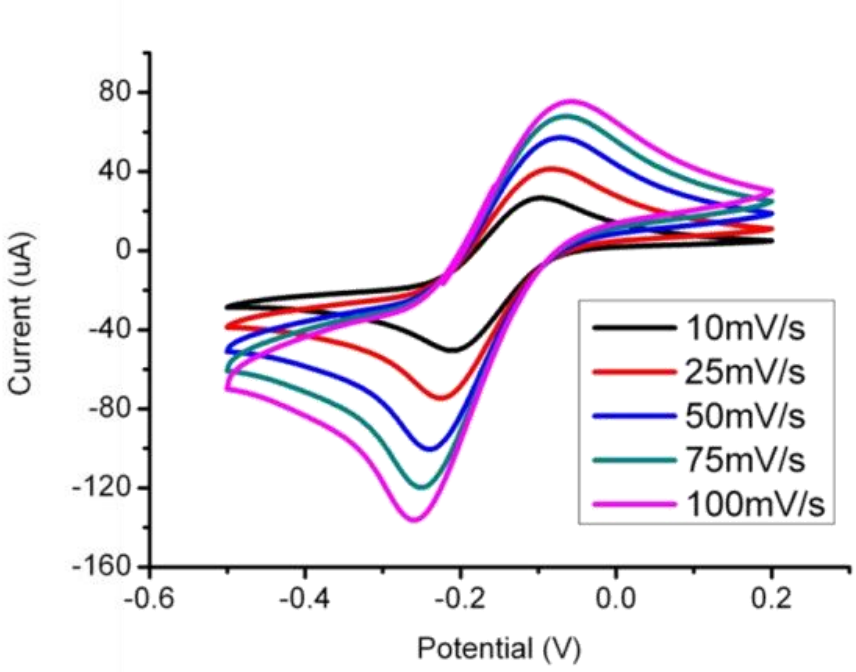

Figure 5.4. CV scan of rGO macroelectrode (0.25 cm^2) with increasing scan rates.

5.3.2.2. MEA Characterization

An array of 30 and 60 µm interelectrode spacing rGO MEAs using 9 µm diameter microelectrodes was fabricated to determine the interelectrode spacing where an MEA geometry would shift from a macroelectrode to a microelectrode regime. In previous chapters, it was found that a spacing of 60 µm would give sigmoidally shaped CV voltammograms. 30 µm pitch spacing was chosen as an intermediate spacing between macroelectrode and microelectrode behavior.

As can be seen in Figure 5.5(a), at a 30 µm spacing array, the CV scans all contain a depletion zone regardless of the scan rate showing predominantly macroelectrode behavior. Interestingly, the depletion for 30 µm interelectrode spacing was 33% at 10 mV/s and 20% for 100 mV/s. This contrasts the rGO

macroelectrode whose depletion percentage increased with faster scan rates. This can be explained because at faster scan rates, the diffusion hemispheres are smaller in size. Consequently the degree of diffusion hemisphere overlap is lessened resulting in a smaller current depletion.

At 60 µm spacing (Figure 5.5(b)) it can be seen that at 10 mV/s there is a slight depletion zone of 6% current decrease. Then at 25 mV/s the depletion zone reduces so that the spectra is sigmoidal in nature with a depletion current of 1%.

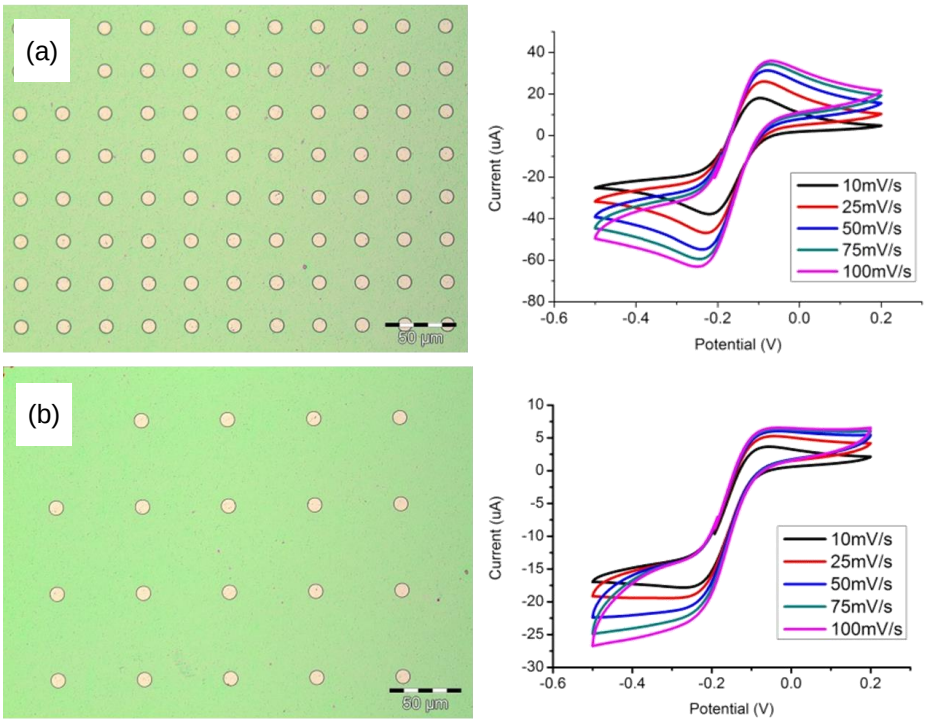

Figure 5.5. Optical image with corresponding CV scan from 10 to 100 mV/s. (a) 30µm pitch spacing. Scalebar is 50 µm (b) 60 µm pitch spacing. Scalebar is 50 µm.

Subsequently arrays of 60, 64, 68 and 70 µm were used to further narrow down the microelectrode regime for higher precision. These interelectrode spacings were used because if MEA behavior occurred in a 60 µm pitch spacing MEA at 25 mV/s, it would stand to reason that larger pitch spacings of

60 µm would be required at 5 mV/s since the diffusion hemisphere will be larger.

A point of interest to note is the CV spectrum of an rGO MEA are more sigmoidal-like at each scan rate when compared to that of G MEA in Figure 3.5 (c). Even though the fabrication parameters were the same for each device, the active material (one being graphene and the other reduced graphene oxide) affected the performance of the MEAs. Peak shaped voltammograms are stronger in intensities for G MEAs due to the conductive properties of reduced graphene oxide.

5.3.3.9 µm diameter MEA series

Figure 5.6 shows scan rates of 60, 64, 68 and 70 µm pitch spacings at 5 mV/s scan rates. At 70 µm pitch spacing the depletion is less than 3% of the peak current. According to our criteria, the device is operating in an MEA regime. This means that the diffusion hemispheres are sufficiently spaced apart, allowing the rate of the flux of the redox analyte towards the active microelectrodes to be high enough to replenish the reduced form of ruthenium hexamine at an equal rate of electron transfer.

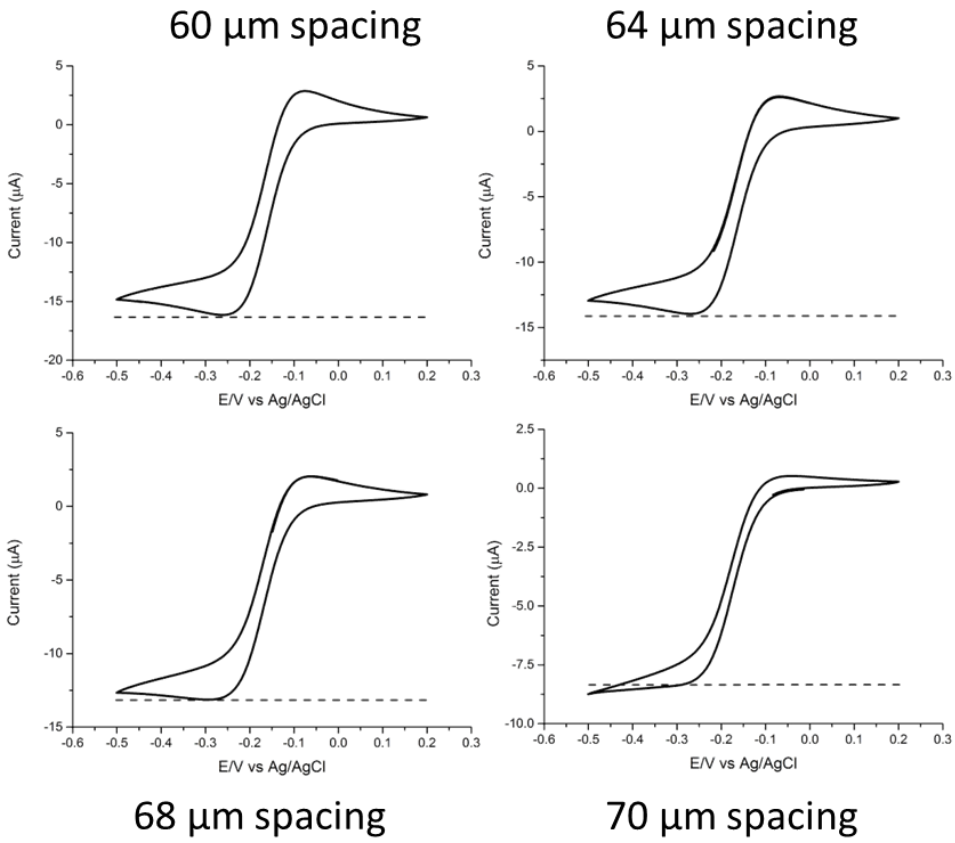

Figure 5.6. CV scans of 5 mV/s scan rates of 9 µm diameter microelectrode arrays at differing interelectrode spacings.

5.3.4. 10 µm diameter MEA series

The same experiment was repeated using 10 µm diameter holes rGO MEAs.

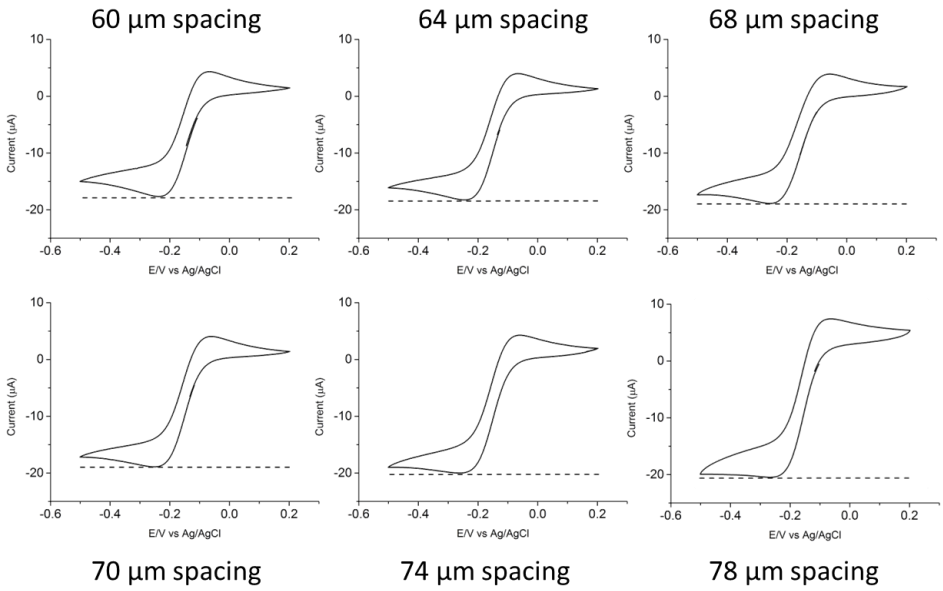

Figure 5.7. CV scans of 5 mV/s scan rates of 9 µm diameter microelectrode arrays at differing interelectrode spacings.

Figure 5.7 shows CV spectra of 5 mV/s scan rates of 60, 64, 68, 70, 74 and 78 µm pitching. In this case, microelectrode behavior occurred at 78 µm spacing (peak current dropped less than 3%) which is larger than the 70 µm spacing required for a 9 µm diameter MEAs. This is to be expected as the diffusion hemispheres of a microelectrode is greatly dependent on the microelectrode diameter.

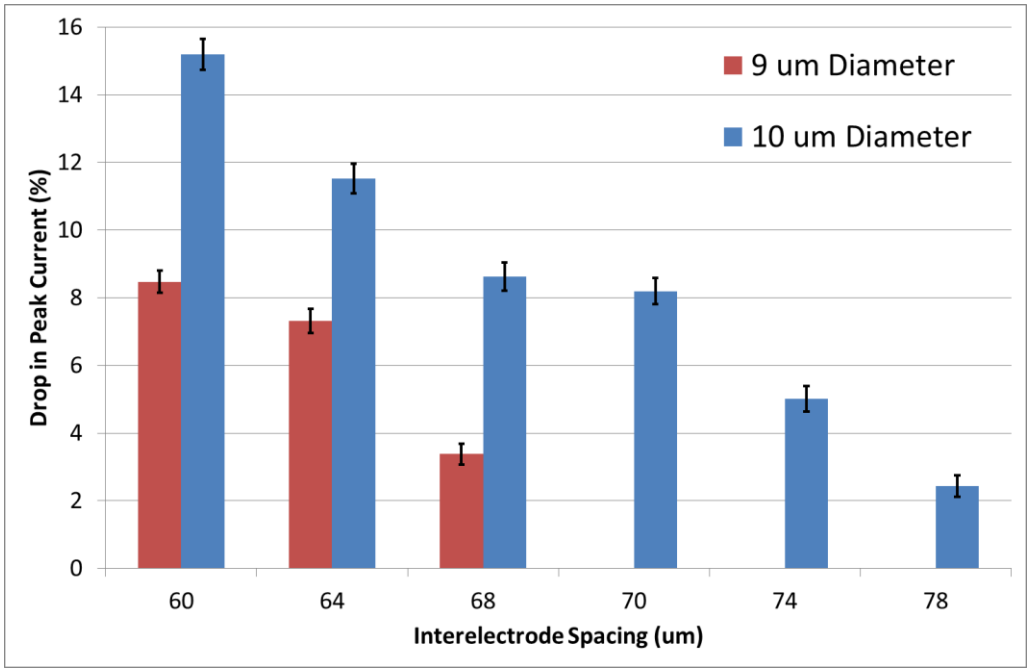

Figure 5.8. Column graph of percentage decrease from peak cathodic current for 9 µm MEA series and 10 µm MEA series.

Figure 5.8 shows a column graph of the percentage depletion. Each interelectrode spacing point was repeated 6 times to obtain a mean and standard deviation of the percentage drop of the current. As can be seen, if MEA occurs when the current drop is less than 3%, the interelectrode spacing of an rGO MEA of 9 µm microelectrode diameter is 70 µm, giving an E_d/E_r ratio of 15.7. For a 10 µm microelectrode diameter, the current drop of less than 3% occurs at an interelectrode spacing of 78 µm which gives an E_d/E_r ratio of 15.7. The ratio of E_d/E_r of 15.7 shows excellent agreement that optimal rGO MEA fabrication should be 15.7 radii to maximize signal to noise ratios without compromising microelectrode characteristics.

It is noted that this ratio is specific for this device with an 800 nm thick resistance layer. Investigation into the effect of the recess depth of an rGO MEA on MEA behavior is still required.

It should also be noted that the ratio may not apply at smaller diameter microelectrodes as theoretical formulae predict that larger ratios are required as microelectrodes decrease in diameter.[12] Further work can be conducted to determine the upper and lower bounds of microelectrode size that the interelectrode spacing to microelectrode radius ratio can be applied too.

5.4. Conclusion

The optimal geometry of an rGO based MEA was probed using CV to determine the point at which MEA behavior occurred for devices of various pitch spacings. The CV spectra of rGO MEAs with increasing interelectrode spacings were characterized. Once depletion currents were less than 3%, the device was considered to be operating in the microelectrode regime. It was found that the ideal E_d/E_r ratio was 15.7 for MEAs with an E_r of 9-10 µm and a recess depth of 800 nm. This result can be used as a guide rule for future rGO MEA-based devices to allow the sensor to consistently function within the microelectrode regime, retaining all its advantageous properties.

Further work can be conducted to determine the upper and lower microelectrode radius bounds of where this ratio can be accurately applied.

5.5. References

1. Aoki, K. Theory of ultramicroelectrodes. *Electroanalysis* **5,** 627–639 (1993).

2. Montenegro, M. I., Montenegro, I., Queirós, M. A. & Daschbach, J. L. *Microelectrodes: Theory and Applications: Theory and Applications*. (Kluwer Academic Publishers, 1991).

3. Oldham, K. B. Theory of microelectrode voltammetry with little electrolyte. *J. Electroanal. Chem. Interfacial Electrochem.* **250,** 1–21 (1988).

4. Jaquins-Gerstl, A. & Michael, A. C. in *Microelectrode Biosens.* (eds. Marinesco, S. & Dale, N.) 55–68 (Humana Press, 2013).

5. Nirmaier, H.-P. & Henze, G. Characteristic behaviour of macro-, semimicro- and microelectrodes in voltammetric and chronoamperometric measurements. *Electroanalysis* **9,** 619–624 (1997).

6. Zoski, C. G. *Handbook of Electrochemistry*. (Elsevier, 2007).

7. Spira, M. E. & Hai, A. Multi-electrode array technologies for neuroscience and cardiology. *Nat. Nanotechnol.* **8,** 83–94 (2013).

8. Brownson, D. A. C. *Handbook of Graphene Electrochemistry*. (Springer, 2014).

9. Edelstein, A. S. & Cammaratra, R. C. *Nanomaterials: Synthesis, Properties and Applications, Second Edition*. (CRC Press, 1998).

10. WOLFRUM, C., LANG, H., MOSER, H. & JORDAN, W. Determination of Diffusion Coefficients Based on Ficks Second Law for Various Boundary Conditions. *Radiochim. Acta* **44-45,** 245–250 (1988).

11. Heerman, L., Matthijs, E. & Langerock, S. The concept of planar diffusion zones. Theory of the potentiostatic transient for multiple nucleation on active sites with diffusion-controlled growth. *Electrochimica Acta* **47,** 905–911 (2001).

12. Tomcik, P. Microelectrode Arrays with Overlapped Diffusion Layers as Electroanalytical Detectors: Theory and Basic Applications. *Sensors* **13,** 13659–13684 (2013).

13. Fletcher, S. & Horne, M. D. Random assemblies of microelectrodes (RAM^{TM} electrodes) for electrochemical studies. *Electrochem. Commun.* **1,** 502–512 (1999).

14. Guo, J. & Lindner, E. Cyclic Voltammograms at Coplanar and Shallow Recessed Microdisk Electrode Arrays: Guidelines for Design and Experiment. *Anal. Chem.* **81,** 130–138 (2009).

15. Henstridge, M. C. & Compton, R. G. Mass transport to micro- and nanoelectrodes and their arrays: a review. *Chem. Rec. N. Y. N* **12,** 63–71 (2012).

16. Becerril, H. A., Mao, J., Liu, Z., Stoltenberg, R. M., Bao, Z. & Chen, Y. Evaluation of solution-processed reduced graphene oxide films as transparent conductors. *ACS Nano* **2,** 463–470 (2008).

17. Gómez-Navarro, C., Weitz, R. T., Bittner, A. M., Scolari, M., Mews, A., Burghard, M. & Kern, K. Electronic Transport Properties of Individual Chemically Reduced Graphene Oxide Sheets. *Nano Lett.* **7,** 3499–3503 (2007).

18. Li, F., Xue, M., Ma, X., Zhang, M. & Cao, T. Facile patterning of reduced graphene oxide film into microelectrode array for highly sensitive sensing. *Anal. Chem.* **83,** 6426–6430 (2011).

Chapter 6. Self-Assembled Peptide Based Reduced Graphene Oxide Nanocomposite for Enhanced Electrochemical Sensing

Abstract

Electrochemical sensor design plays a pivotal role in electrode operating behavior. Two critical design criteria are the size of the active layer and the type of active layer used in the electrode. These two parameters affect the output current of a sensor and thereby its performance in detection. As sensor sizes become smaller, so too do the signal currents generated in analyte sensing.

This problem is addressed in this paper by the use of a non-planar porous electroactive network consisting of reduced graphene oxide (rGO) and N-fluorenylmethoxycarbonyldiphenylalanine (Fmoc-FF) nanocomposite. The composite of rGO/Fmoc-FF is a 3-dmensional network that increases the effective electroactive area resulting in an approximate 40% increase in cathodic current for two coatings.

In order to form a uniform nanocomposite coating, optimization of the pH and Fmoc-FF concentrations were investigated. The nanocomposite was found to be stable for extended periods of electrochemical testing and had a wide electrochemical window of 2.3 V. The sensor was used to detect serotonin even in the presence of interfering dopamine and ascorbic acid molecules and found to have superior sensitivities to other reported rGO based devices.

6.1. Introduction

The two main criteria that affect the performance of a sensor are its selectivity and its sensitivity. Selectivity is related to how the sensor responds to one species of analyte in the presence of other interfering species. The sensitivity is related to the output current and the concentration of the target species. In turn, selectivity and sensitivity are affected by the type of material the active layer is made of, which governs chemical interaction between the species and the electrode.[1] Sensitivity is also related to the size of the active layer according to the Randles-Sevcik equation. As the functional area of the sensor increases, a higher peak current is detected, leading to greater sensitivities and lower limits of detection.[2]

A prerequisite of an active layer is that it has to be conductive. Traditionally, electroactive active layers have been metal based. Recently there have been many reports on the synthesis and characterization of new sensor active layers that have shifted away from metals to conducting polymers[3–5] and carbon based materials, such as glassy carbon,[6–8] carbon nanotubes,[9–11] graphene[12–14] and reduced graphene oxide (rGO).[15–17]

rGO has been reported to be an excellent electroactive material for sensing.[18] Its high flexibility, biocompatibility and electrical conductivity makes it an excellent candidate to be a bio/chemical electroactive material.[12,19]

Most sensors today are planar, whereby the electroactive surface is 2D, therefore if signal increase is required through increasing the size of the functional electroactive area; it is likely the electrode would also increase in size. A larger device footprint would limit the environments that the sensor

can used in, for example, in micro fluidic channels or biological systems such as blood vessels.

To increase signal gains without having to increase sensor size, there have been several physical modification routes reported. Firstly, fabricating the sensor into a microelectrode array format allows for an increase in diffusion flux of the analyte towards the electroactive area, thereby increasing current gains.[20,21]

Secondly, porous organic compounds have also been used to replace traditional 2D planar electro active areas, thereby increasing the effective electrode surface area using materials such as macroporous carbon.[22] Lastly, graphene foam has been used to enhance sensing properties[23] and Liu et al. reports a combination of cobalt oxide nanowires supported on carbon foam.[24]

However a drawback of these techniques is that they require tedious preparation methods and/or extreme conditions. For example, carbonizing of the graphene foam requires process temperatures up to 700 ^{o}C followed by synthesis of the cobalt nanowires and then subsequent mixing steps between the nanowires and the graphene foam are carried out overnight. Once mixed, the solution is then drop cast onto a glassy carbon electrode. Drop casting electroactive materials onto other electrodes may allow for useful investigation into the properties of novel electroactive materials in the lab; however it doesn't scale well into mass sensor fabrication due to active layer uniformity issues. This is because as a droplet dries, the suspended solid active material is not evenly distributed over the surface, which leads to inconsistent device performances.

To mediate the tedious preparation procedures, a candidate material that has garnered interest as an electroactive layer is self-assembling hydrogels. These hydrogels have attracted much interest in the areas of bio-applications and conducting organic materials.[25–32] Hydrogels are networked polymer chains that are cross-linked with each other. Dissolving the precursor monomers in solution, the crosslinking process can be initiated by external stimuli such as temperature or pH changes.[33–36] The precursor hydrogel molecules form a fibrous network throughout the solution they are dissolved in, which causes a significant increase in viscosity, creating a gel like substance. This polymeric network forms highly cross-linked fibers resulting in a complex web-like morphology at the micron level.[37,38]

Peptide based hydrogels are a subset of the hydrogel family and have proven to be a potentially important class of hydrogel for future bioapplications. Some advantageous characteristics of peptide-based hydrogels are low toxicity, biocompatibility, spontaneous self-assembly, being made of differing chemical groups which allow for ease of functionalization or modification, doesn't require complicated synthesis methods involving harsh reaction conditions, no complex chemistry, and no harmful catalysts or tedious purification and preparation procedures.[39–43]

N-fluorenylmethoxycarbonyldiphenylalanine (Fmoc-FF) is a peptide that can spontaneously self-assemble into a hydrogel network without the need for harmful chemicals. Dissolving Fmoc-FF in an alkaline solution and then lowering the pH below a critical level results in a rigid and transparent

hydrogel. Coupled with its biocompatibility, Fmoc-FF hydrogels have been used in various applications such as drug delivery, cell culturing and energy storage.[32,44–46]

Self-assembly of the Fmoc-FF hydrogel is predominantly governed by the π-π interactions between the Fmoc groups (Figure 6.1) forming a chiral tube-like structure. These Fmoc-FF tubes then aggregate beside each other to form long range fibrous networks in 3-D space.[47]

Yemini et al. reported the use of Fmoc-FF on carbon screen printed electrodes (SPE) to enhance current output. A drop of Fmoc-FF solution was deposited on the active surface of an SPE and allowed to dry, leaving large clusters of peptide nanotubes. The signal enhancement was attributed to an increase in active surface area created by the Fmoc-FF tubes.[48]

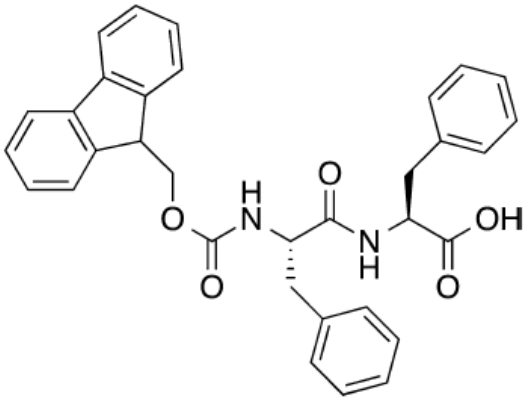

Figure 6.1. Molecular structure of Fmoc-FF

In another work by Xing et al. GO was mixed with a similar peptide based hydrogel. It was found that the mechanical, fluorescent and thermal properties of the hydrogel could be tailored depending on the concentration of the GO added.[49]

Utilizing the self-assembling nature of the Fmoc-FF molecule, the network formed can act as a molecular scaffold and electrical pathway for the active rGO flakes. This allows for more electroactive sites per area to be exposed to the environment, resulting in current increases that can be realized without having to increase the sensor size in the 2D plane but rather being able to quantitatively increase the number of rGO active sites in the Z direction (Figure 6.2).

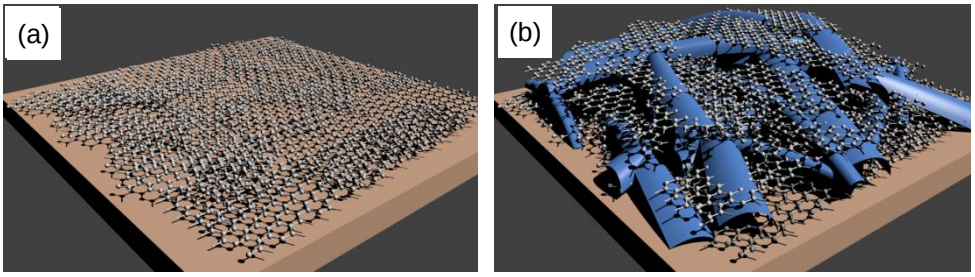

Figure 6.2. (a) rGO layer on a substrate showing the 2D planar nature of a typical electrode. (b) GO/Fmoc-FF layer showing scaffold effect of the Fmoc-FF allowing more rGO active sites to be exposed.

Peptide based hydrogels can alleviate the conventional complex steps of synthesising 3D active layer materials, however in the cited reports the peptide hydrogels are still drop cast onto an electrode layer, which still leaves the problem of uneven active material distribution and inconsistent device performance. Controlling hydrogel thicknesses has not been a concern as characterization of the bulk hydrogel material has been the predominant focus. Synthesis of new active materials that can enhance current output with uniform spin coating properties would allow for larger area electrode coatings increasing device fabrication output and higher sensitivities.

In this chapter peptide based rGO nanocomposites (rGO NC) were investigated. Fmoc-FF was chosen due to its electrochemical properties, and for the ease at which it forms a fiborous network. Its benzene ring chemical structure backbone that would allow GO sheets to bond to it via π-π stacking. Other advantageous characteristics of easy synthesis by adjusting the pH of the solution in which the peptide precursors are dissolved, uniform large area substrate coating and increased sensitivities were probed. This allows for quantitative comparisons to normal rGO electroactive layers and allows for scaling of rGO NC sensor fabrication.

An optimal pH and Fmoc-FF concentration was determined to trigger hydrogel formation, without creating dense clustering that would prevent uniform spin coating of the hydrogel layer. With said ideal final pH in mind, the GO solution and initial Fmoc-FF solution were prepared in such a manner as to arrive at the ideal final pH and concentration upon combination. The mixing of the GO and Fmoc-FF solutions then resulted in a nanocomposite solution that could be readily spin coated onto any surface, leaving GO flakes intertwined with the Fmoc-FF network.

6.2. Materials and Methods

6.2.1. Chemicals

4 mg/ml GO solution was purchased from Graphenea Inc. Serotonin, reagent grade ascorbic acid, dopamine hydrochloride and Ruthenium (III) Hexamine were purchased from Sigma Aldrich Co. and Fmoc-FF was purchased from BaChem.

6.2.2. Fmoc-FF rGO.

Stock solutions of pH 11, 11.5, 12 and 12.5 were made by filling glass bottles with 30 ml DI water and adding NaOH until the desired pH was reached.

The Fmoc-FF and GO composite was prepared by mixing 4 mg of Fmoc-FF into 1 ml of the stock DI water with varying pH in Eppendorf Tubes. The solution was then vortexed for 30 minutes. 1 ml of 4mg/ml GO solution was added to the Fmoc-FF solution and vortexed for a further 5 minutes.

6.2.3. Electrochemical Reduction

The GO/Fmoc-FF solution was spin coated onto an ITO/PET substrate at 2000 rpm for 30 seconds and then placed on a heater plate at 100^{o}C for 1 minute to dry. The substrate was immersed in sodium phosphate buffer saline (Na-PBS) at pH 4.5 with an Ag/AgCl reference electrode and platinum mesh as a counter electrode. Chronoamperometry (CA) was used at a set voltage of -0.9 V for 2 minutes.

Cyclic voltammetry (CV) and differential pulse voltammetry (DPV) were carried out using a 3 probe setup. The substrate was connected to the working electrode, Ag/AgCl reference electrode and platinum mesh as the counter electrode. 0.1 M KCl solution with 2.5 mM Ruthenium (III) Hexamine as the redox probe was used for CV measurements. 0.1M Na-PBS solution at pH 7.4 was used in DPV experiments for detection of serotonin.

6.2.4. Atomic Force Microscopy (AFM)

An ICON Bruker AFM was used to conduct topological characterization. The respective GO NC solutions were spin coated onto ITO/PET substrates and electrochemically reduced after which they were imaged using tapping mode AFM. Images were post processed using Gwyddion. Step height profiles and roughness values were extracted using the Gwyddion program. The RMS mean and standard deviation values were taken from 10 2 x 2 μm areas.

6.2.5. Scanning Electron Microscopy (SEM)

SEM imaging was conducted by spin coating the GO NC solutions onto ITO/PET substrates, electrochemically reduced and then imaged in a FEGSEM JSM 7600F environmental SEM. A metal coating layer was not required as the material was conductive enough to prevent charging effects.

6.3. Results and Discussion

Conventional usage of FMOC-FF as a hydrogel involved the synthesis of highly networked clusters without considering the thickness of the gel. In order to create a relatively planar rGO active nanocomposite material, studies into the gelation characteristics by pH switching were necessary. Fmoc-FF molecules are ionized when dissolved in solution. At high pH, the monomers do not self-assemble due to electrostatic repulsion. As the pH is brought lower,

the charge is neutralized and the electrostatic repulsive forces decrease leading to self-assembly[50] The degree of self-assembly is affected by the pH, allowing tuning of the properties of the GO NC layer by adjusting pH values.[51]

6.3.1. Effect of pH

As previously stated, it has been well documented that the Fmoc-FF gelation process can be triggered by pH changes.

4 aliquots of DI water were adjusted to varied levels of alkalinity (pH 11, 11.5, 12, and 12.5) using NaOH. Fmoc-FF was then added to each. It was observed that Fmoc-FF did not dissolve well into pH 11, partially dissolved in pH 11.5 and only fully dissolved in at pH 12 and 12.5. To form the GO NC, GO must be added and the pH of the mixture be brought low enough to start the self-assembling process. The 4mg/ml GO purchased had a pH of 1.8, making it an ideal solution to trigger self-assembly and concurrently add GO flakes to the solution. After mixing the GO solution into the various Fmoc-FF solutions, the final pH of the solution varied and therefore affected the final morphology of the GO/Fmoc-FF network structure. As the pH is lowered, more of the ionized Fmoc-FF monomers are neutralized favoring a greater degree of self-assembly of the hydrogel.

Figure 6.3 shows optical images of differing morphologies of the GO composite layer based upon the final pH of the solution. Figure 6.3(a) is a substrate with only GO. Figure 6.3(b) shows a solution with an initial pH of 11 and a final pH of 3.7. The self-assembled layer was rod-like due to Fmoc-FF being unable to properly dissolve at pH 11. Figure 6.3(c) shows

morphology derived from an initial pH of 11.5 and a final pH of 3.8. Strong hydrogel assembly is present; however the layer is not uniform, as evidenced by the randomly distributed large clusters of peptides across the film. These hydrogel clusters would vary in size from 200 to 1500 μm with thicknesses that was measured to be 3 to 4 μm. The inconsistency disallowed any controlled comparisons of the effect of the hydrogel on sensor performance. Each substrate that was spin coated with the GO NC solution of pH 3.8 would yield vastly different active layer coatings. Figure 6.3(d) is from an initial solution of pH 12 and a final pH of 11.5. The image in Figure 6.3(d) shows absence of clustering. At pH 12.5, upon mixing with the GO solution and spin coating, only GO flakes were seen on the substrate. This is because the final pH of 12.1 was not low enough for neutralization of the Fmoc-FF molecules that allowed self-assembly to occur. Tang et al. reports similar trends when they investigated pH changes in Fmoc-FF solutions. They found that the Fmoc-FF would undergo strong hydrogelation below pH 7 and also reported a small population of Fmoc-FF fibrils forming at a pH 10.5.[50] It should be noted that the GO NC solution with a final pH of 11.5 remained stable and could still be uniformly spin coated.

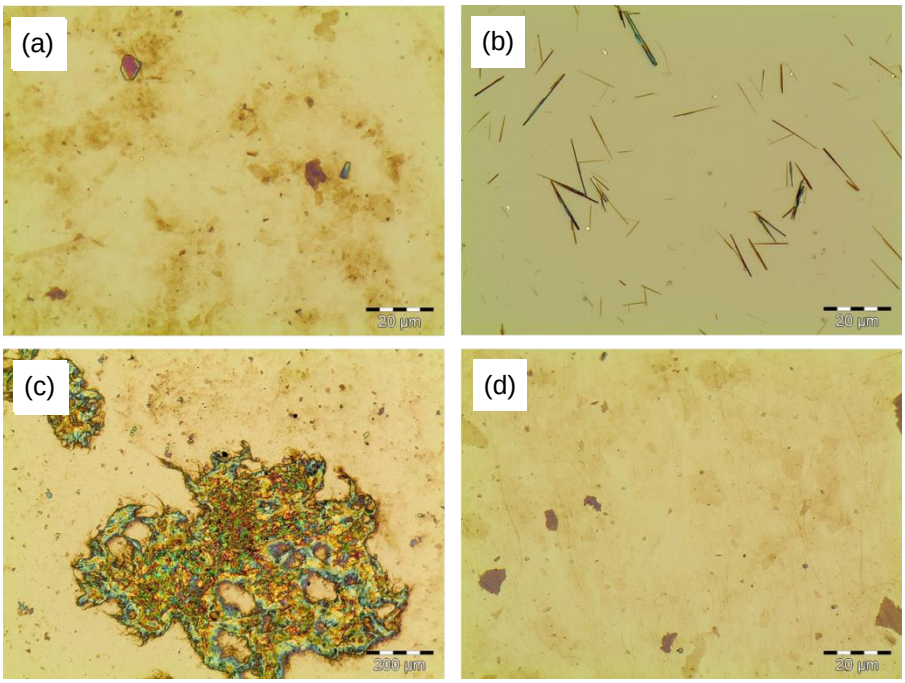

Figure 6.3. Optical images of (a) Spin coated GO. Scale bar is 20 µm. (b) Fmoc-FF forming short rod-like structures. Scale bar is 20 µm. (c) Fmoc-FF island clusters. Scale bar is 200 µm. (d) Fmoc-FF forming uniform fibrous layer with GO flakes intermixed. Scale bar is 20 µm.

SEM imaging was conducted on the various samples. As shown in Figure 6.4(a), the substrate was coated with GO flakes and rod-like structures of Fmoc-FF as opposed to the long fibrils expected in Fmoc-FF gelation. This was due to the lowered Fmoc-FF concentration since the peptide did not dissolve very well into a solution of pH 11. Figure 6.4(b) shows the GO flakes preferentially agglomerating within the island networks of the Fmoc-FF. The surrounding substrates are relatively bare of GO flakes. It is suspected that this is because hydrogel formation occurs by π-π stacking between Fmoc-FF molecules via their fluorenyl and phenyl rings. The same mechanism allows the GO sheets to also π-π stack highly favoring the hydrogel clusters instead of the substrate. Figure 6.4(c) shows a uniform layer of GO flakes dispersed and intertwined throughout the fibrous network of the Fmoc-FF self-assembled

layer. Figure 6.4(d) shows a substrate that has been coated with only Fmoc-FF. This was done using a 1 ml HCl solution at pH 1.8 and mixing it with a 1 ml solution of Fmoc-FF dissolved in DI water at pH 12. As can be seen, there is little difference in the morphology of the pH 12 self-assembled layer with or without GO flakes. Triggering of the gelation process can be done independent of GO and shows a uniform coating is possible just by pH adjustment, the presence of GO does not interrupt the self-assembly process, opening up the possibilities of fabricating other uniform electroactive Fmoc-FF based nanocomposites.

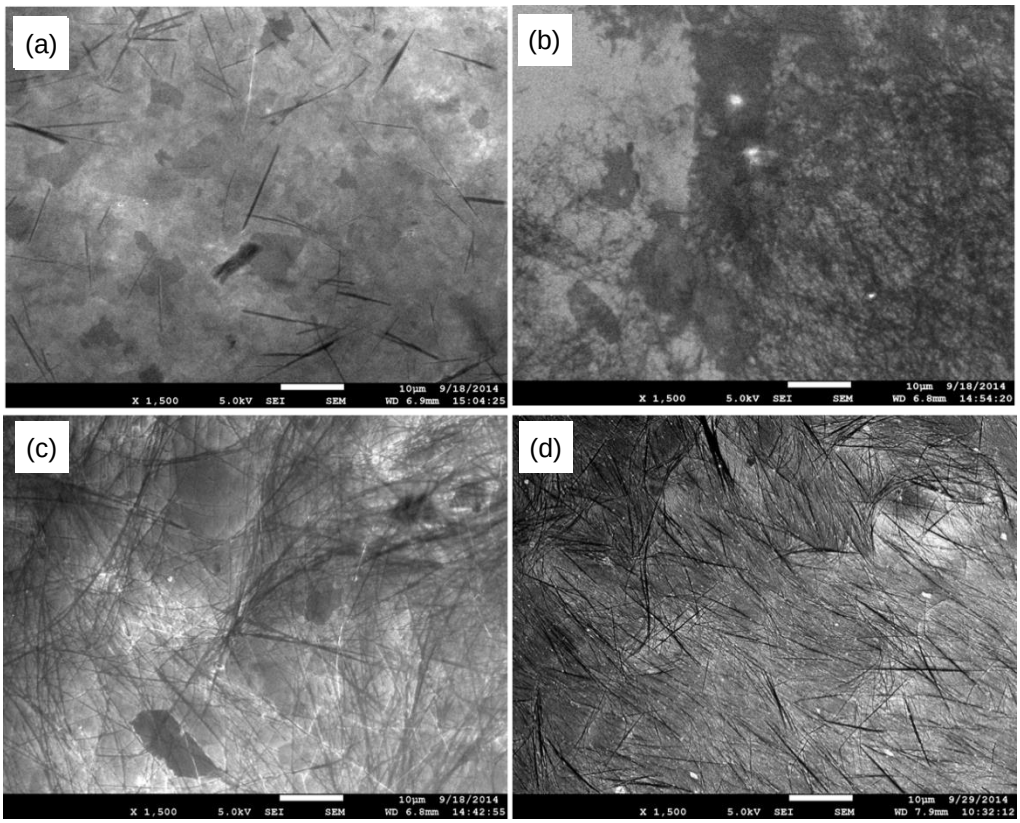

Figure 6.4. SEM imaging of spin coated (a) pH 3.7 - GO NC showing GO flakes with rod-like structure Fmoc-FF. (b) pH 3.8 - showing large clusters of GO/Fmoc-FF clusters with surrounding areas being largely devoid of GO flakes. (c) pH 11.5 - GO/Fmoc-FF layer showing uniform layer of Fmoc-FF fibres with GO flakes intertwined within. (d) pH 11.5 - Fmoc-FF layer with no GO added to the mixture.

AFM imaging was conducted on rGO NC and Fmoc-FF that was spincoated onto ITO/PET substrates. To measure the fibril widths and height and also the roughness of the rGO NC layer, the surface roughness root mean square (RMS) can be measured by AFM. RMS values represents the standard deviation of surface heights over the scanned area. As surface heights increase so too does the surface roughness and RMS values, that is layers that are flat have lower RMS values as compared to highly porous layers that have higher RMS values.[52] RMS measurements were used to show the morphological differences in the rGO NC layer and the rGO layer.

Figure 6.5(a) shows AFM imaging of rGO NC layer with final pH 11.5 showing Fmoc-FF fibres ranging from 10-150 nm in width. The thickness of the fibrils and roughness of the area was measured to be on average 9 nm with a 5 nm root mean square (RMS) roughness suggesting that the fibers are flat ribbons. This is consistent with other reports that detail the formation of the networks that are made up of 3 nm wide Fmoc-FF ribbons and organize themselves in a lateral fashion to create thicker ribbons.[53] 10 RMS values were taken over the substrate and the standard deviation was 0.8 nm showing good uniformity. This is in contrast to the rGO NC layers with final pH 3.7 and 3.8, where rod-like or large clustering occurred. Selecting areas on the substrate that would be representative of the entire layer could not be done due to the inconsistent coverage of the rGO NC layer.

Figure 6.5(b) shows Fmoc-FF with final pH 11.5 without GO flakes. The thickness was 8 nm with a roughness RMS of 7.1 nm with a standard deviation of 0.9 nm.

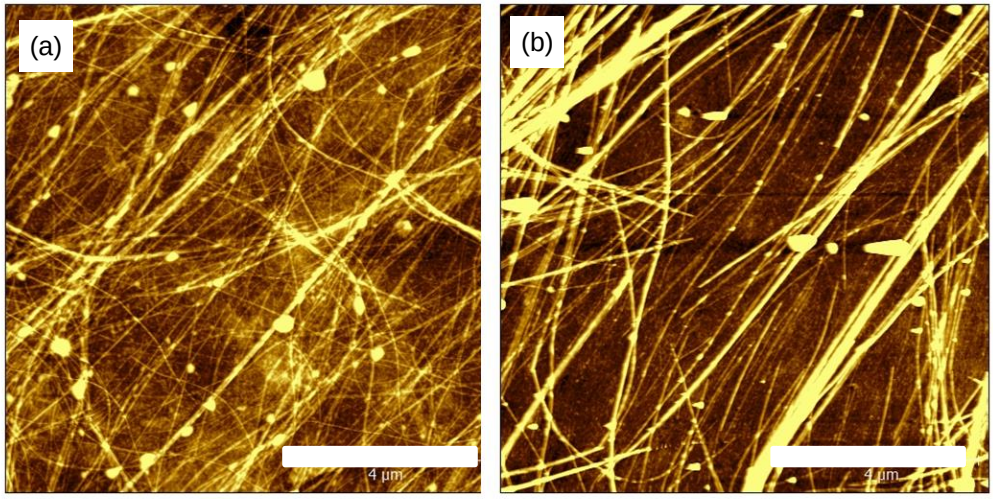

Figure 6.5. AFM Imaging of (a) GO/Fmoc-FF. White scale bar 4 µm. (b) Fmoc-FF without GO. White scale bar 4 µm.

Figure 6.6(a)-(c) shows SEM imaging and AFM imaging of a GO layer that has not been mixed with Fmoc-FF. The thickness was found to be 4 nm with a 2 nm RMS roughness and a standard deviation of 0.2 nm. Coupled with the height figures of GO NC, this suggests that the nanocomposite structure has increased the thickness and roughness of the rGO active layer.

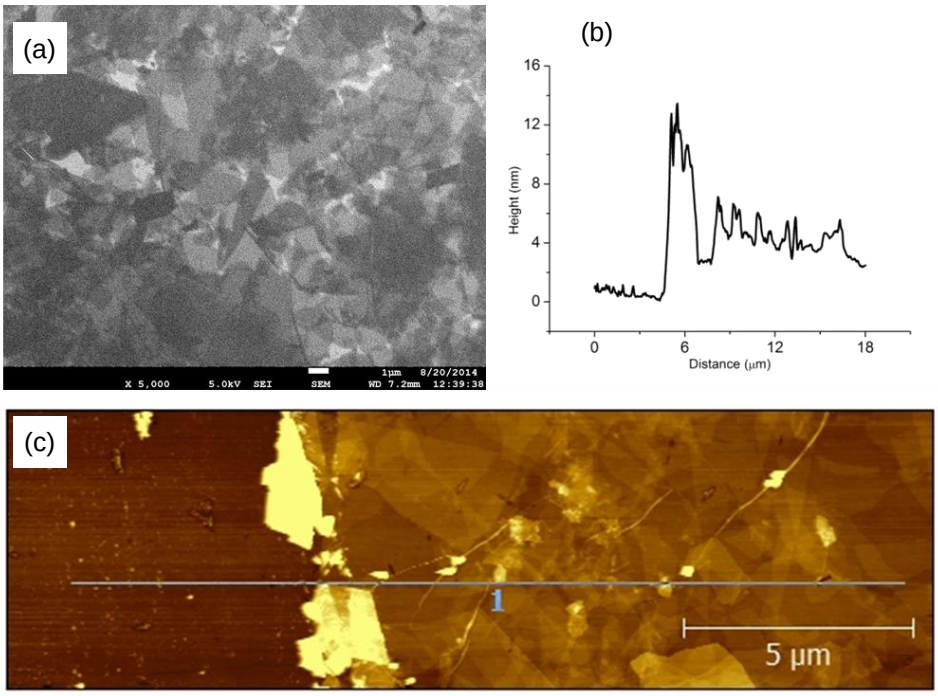

Figure 6.6. (a) SEM image of rGO layer. (b) Step height profile of rGO layer. (c) AFM imaging of step height of rGO layer.

6.3.2. Effect of Fmoc-FF Concentration

Knowing the ideal starting pH of 12, the effect of Fmoc-FF concentration was investigated. Concentrations of 1, 3 and 4 mg/ml Fmoc-FF/ 2 mg/ml GO solutions were made using the same process as 2 mg/ml Fmoc-FF/GO solutions.

During spin coating of the varying GO NC concentration solutions, the substrate had dense clustering over the surface that was not uniform for concentrations of 4 mg/ml and 3 mg/ml. Figure 6.8(a)-(b) shows SEM images of the GO NC concentrations that were did not uniformly coat. Large clustering of the hydrogel was evident. Previous results showed that clustering and non-uniformity occurred at lower pH values, however in this case the pH values remain the same but the concentrations have increased.

The high concentrations of Fmoc-FF causes the intermolecular interactions to dominate the electrostatic repulsive forces resulting in self-assembly.[54] In this case the self-assembly has occurred to a degree where uniform spin coating was not evident.

Figure 6.8(c) showed uniform coating of the rGO NC material. There was no large clustering of the hydrogel, and there was little deviation in the RMS values across the sample as previously mentioned.

Figure 6.8(d) (1mg/ml Fmoc-FF concentration) showed very few hydrogel fibrils, that otherwise would have been expected at this pH. The fibrils that could be seen were short and rod like in appearance. This shows that pH and concentration of the hydrogels are interdependent. It could be that uniform coating can be achieved at differing concentrations by adjusting the final pH. In this case since the pH value of the GO solution was fixed, 2 mg/ml Fmoc-FF was the optimal concentration found for a final solution pH of 11.5. Lower concentrations of Fmoc-FF may still allow similar hydrogel morphologies as 2 mg/ml except the final pH may need to be adjusted to a lower point to increase the neutralization of the ionized molecules to begin self-assembly. There have been reports in a similar vein in which salts were added to the hydrogel solution to lower intermolecular repulsion and begin the self-assembly without adjusting the pH.[30,55] However more experiments are required to determine Fmoc-FF's pH dependent behavior for differing concentrations that would allow the material to be spin coated uniformly.

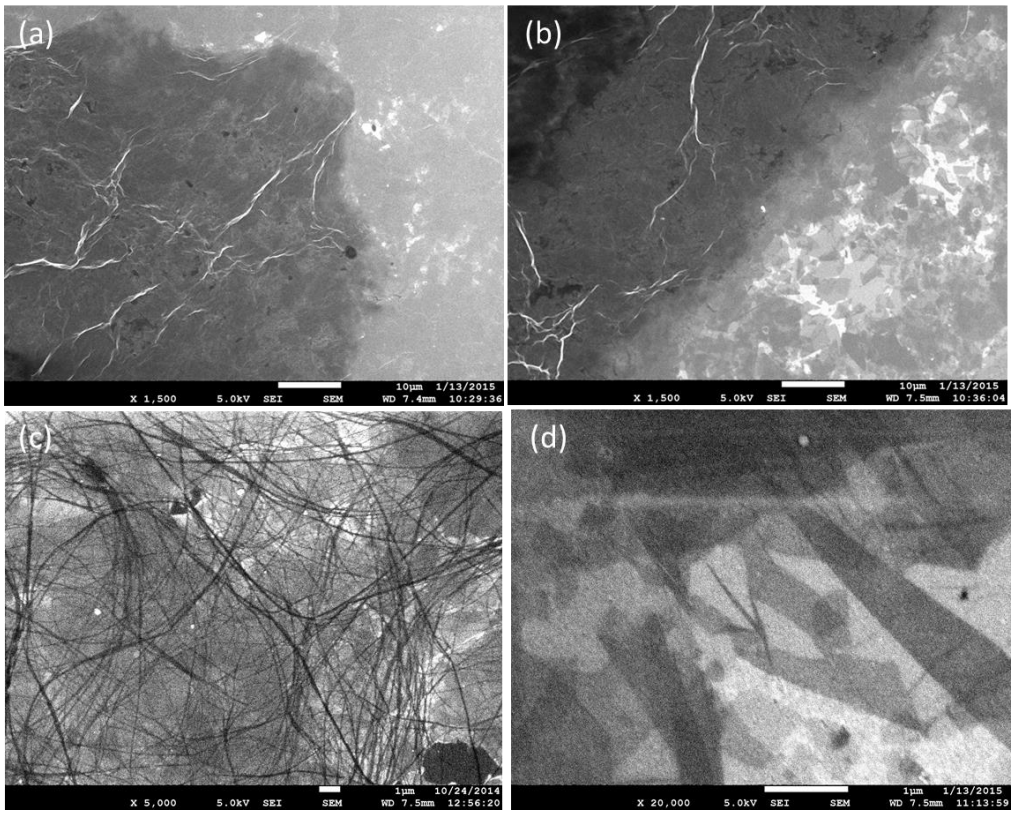

Figure 6.8. SEM imaging of coatings with differing Fmoc-FF concentrations. (a) Coating using 4 mg/ml. White scale bar is 10 µm. (b) Coating using 3 mg/ml. White scale bar is 10 µm. (c) Coating using 2mg/ml. White scale bar is 1 µm. (d) Coating using 1 mg/ml. White scale bar is 1 µm.

6.3.3. Effect of Fmoc-FF Concentration

Knowing the optimal starting pH (12) and concentration (2mg/ml) of Fmoc-FF, all further experiments were done using these conditions. GO NC was investigated to determine if it could withstand electrochemical treatment. In order for the GO NC to be electroactive, the GO flakes needed to be reduced to recover electrical conductivity characteristics.[56] Electrochemical reduction was chosen as the reduction method.

The potential window of rGO NC was investigated using 0.1 M KCl solution with a 0.25 cm^2 electrode of GO NC (Figure 6.9(a)). The potential window

measured a potential range in which the active material does not oxidize or reduce and contribute to the signal current. As seen, the electrochemical window of GO NC is from -1.1 to 1.2 V, showing that the Fmoc-FF network does not negatively affect the electrochemical window of rGO and has similar values to other reported rGO potential windows.[57–59]

The stability of the rGO NC was also tested. CV was run at a slow scan speed of 5 mV/s for 120 cycles for 8 hours. As can be seen in Figure 6.9(b), the peak cathodic and anodic currents do not change significantly over the course of the scan time and the onset potential for oxidation and reduction does not change, showing that the rGO NC electroactive material is stable and possesses a large potential window.

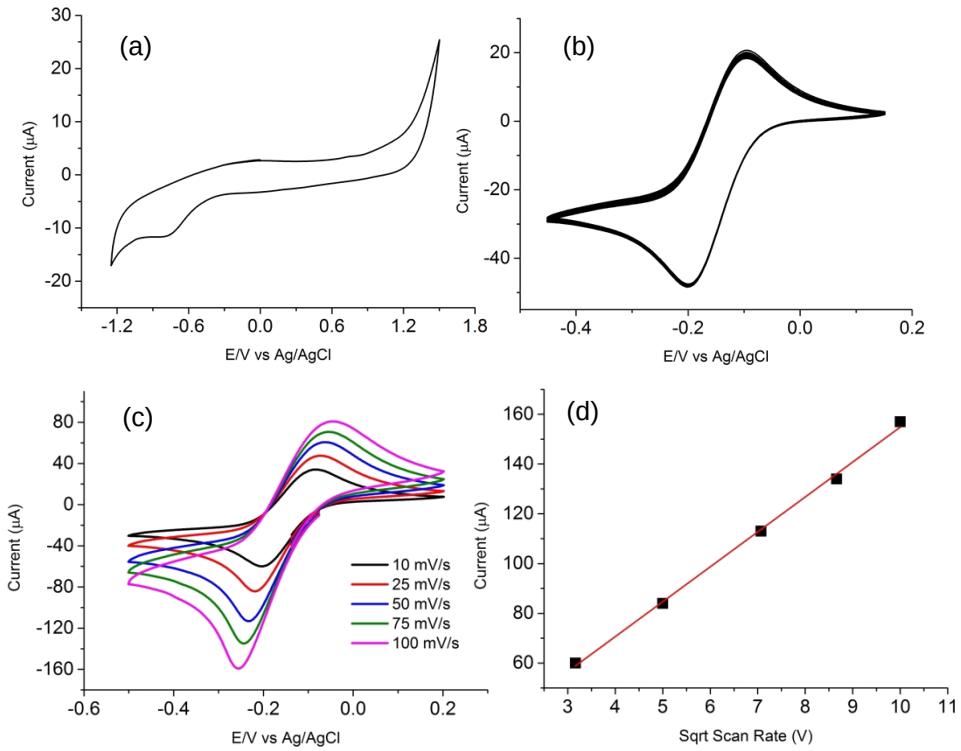

Figure 6.9. (a) Electrochemical window of rGO NC. (b) 8 Hrs of CV at 5 mV/s of rGO NC stability testing. (c) 0.25 cm^2 rGO NC electrode at differing scan rates. (d) Plot of current vs sqrt of scan rate showing oxidation/reduction is diffusion limited.

Figure 6.11(c) shows an rGO NC electrode at differing scan rates. The oxidation and reduction potentials are similar to an rGO macroelectrode which indicates that rGO is the predominating electroactive material and any contribution from the Fmoc-FF is negligible. Figure 6.9 (d) shows a plot of peak cathodic peak current vs the square root of the scan rate. The linear regression fit has an r^2 of 0.99 which shows that the process is diffusion limited.

The peak cathodic current generated by rGO NC was compared to ITO, rGO and Fmoc-FF. 0.25 cm^2 macroelectrodes were fabricated with differing electroactive materials. The peak current can be predicted using the Randles-Sevcik equation.[2]

$$i_p = 2.69 \times 10^5 \, n^{3/2} \, AD^{1/2} Cv^{1/2}$$

where i_p is the peak current, n is the number of electrons transferred in one reaction, A is the electrode area, D is the diffusion coefficient, C is the concentration of the ruthenium (III) hexamine and v is the scan rate.

In this case $n = 1$, $A = 0.25$, $D = 3.02 \times 10^{-3}$, $C = 2.5 \times 10^{-6}$ and $v = 0.01$ the predicted peak current is 50.7 µA.

As seen in Figure 6.10, the approximate cathodic peak current for ITO, rGO and Fmoc-FF is approximately 50 µA. However for rGO NC, the peak current is 65 µA, an increase of approximately 25 %. This increase in peak current is attributed to the rGO flakes being intermixed into the Fmoc-FF network. The 3-D like scaffolding nature of the self-assembled network increases the active sites per area of the electrode as the redox probe can diffuse into the Fmoc-FF

matrix. An rGO macroelectrode with a thicker 8 nm layer was also compared to determine if the thickness had any impact on the signal response. As seen, a thicker rGO active layer comparative to the thickness of an rGO NC layer did not increase the peak current. This shows that the networked morphology of the rGO NC layer was responsible for the increase in cathodic current.

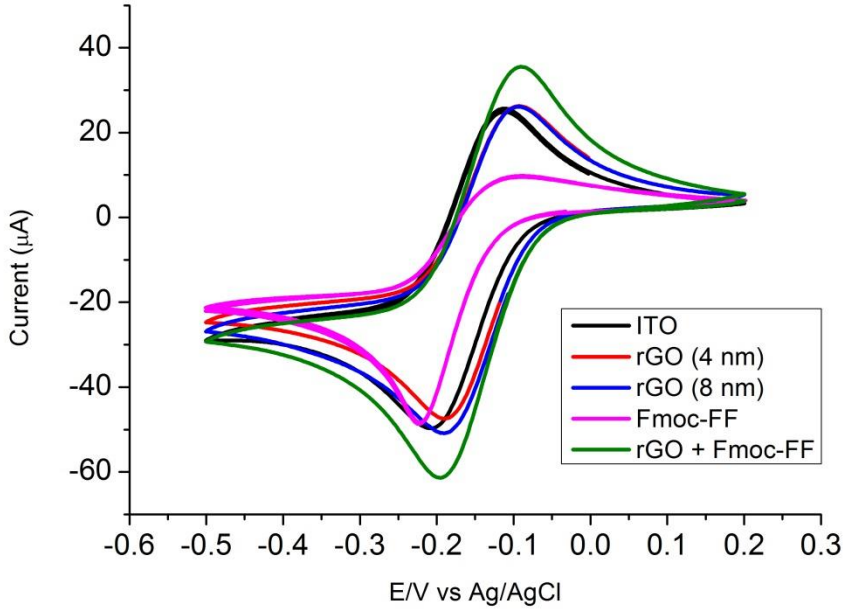

Figure 6.10. CV comparison of peak cathodic currents with differing electroactive substrates of the same size.

6.3.4. Effect of Multiple Coatings

The effect of multiple coatings on electrochemical properties of the rGO NC was investigated. After spin coating a layer of GO NC, it was allowed to dry for 3 hours before applying the next coating of GO NC. Using this method, samples of one, two and three layers of GO NC were fabricated. The samples were then electrochemically reduced.

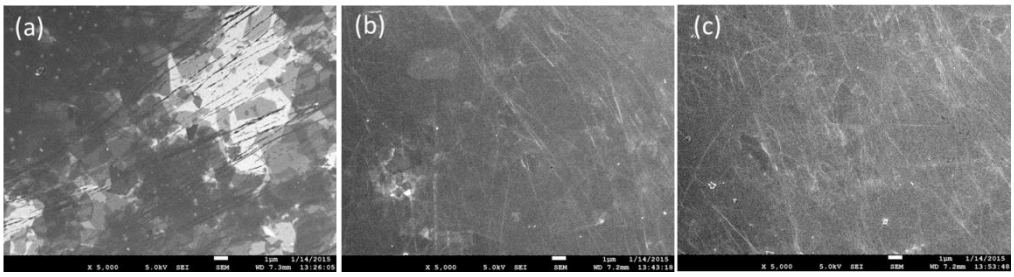

Figure 6.11. SEM imaging of (a) One layer rGO NC (b) Two layer rGO NC and (c) Three layer rGO NC

SEM imaging was used to image the surface morphology of the spin coated hydrogels. Figure 6.11 shows a difference between one and two layers, with a second coating giving a thicker layer of GO over the ITO surface. The GO flake outlines are now harder to resolve due to the thicker coating. Figure 6.11(c) shows three layers of rGO NC. There was little difference between a second and third coating since application of the second coating on the ITO/PET was more complete, resulting in a third coating layer having minimal morphological effect.

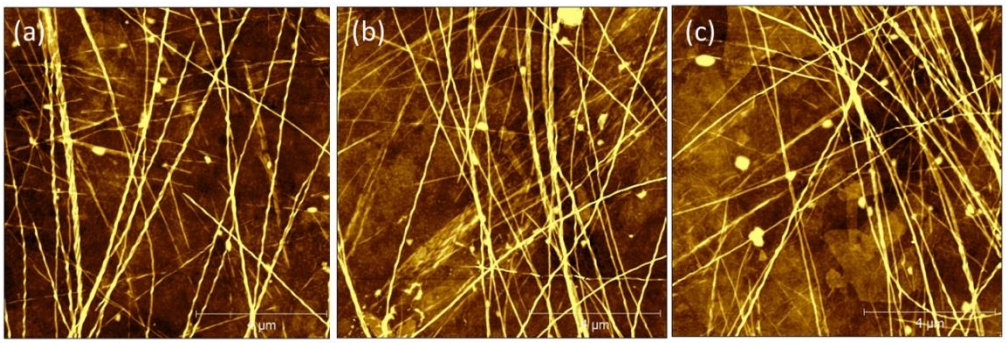

Figure 6.12. AFM imaging of (a) One layer rGO NC (b) Two layer rGO NC and (c) Three layer rGO NC.

AFM imaging was performed on the multi layer GO NCs. For two layer rGO NC, the RMS was 10 nm with a standard deviation of 0.9 nm, increasing by 3 nm from a single layer of rGO NC. The three layer rGO NC also had an RMS

of 10 nm with a standard deviation of 0.9 nm. This indicates that a third coating may not have increased the porous properties of the active layer in any appreciable manner.

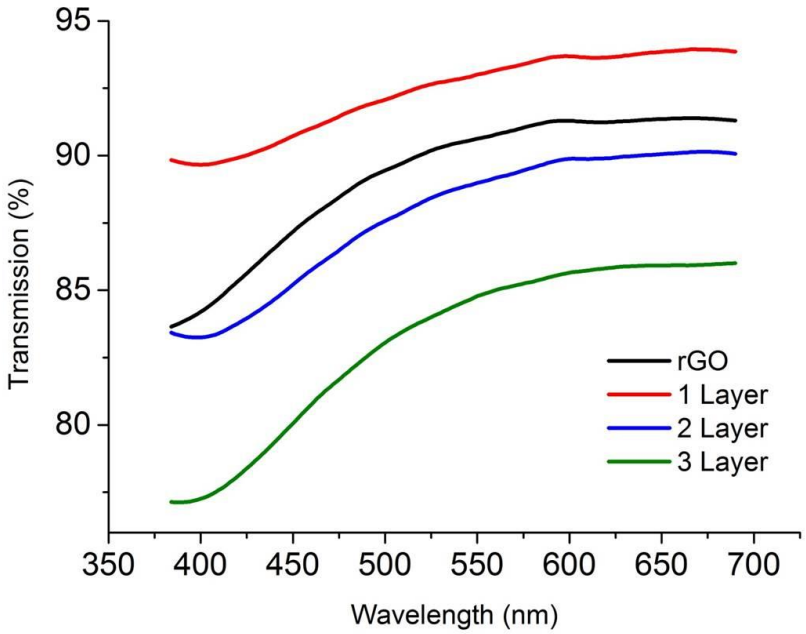

Figure 6.13. UV-Vis comparison of rGO, one layer rGO NC, two layer rGO NC and three layer rGO NC.

UV-Vis was used to compare the layer thickness. The thicker the layer, the greater the degree of blocked visible light. In Figure 6.13, it can be seen that one layer of rGO NC would block 7% of visible light at 550 nm, two layers Blocked 11 % and three layers blocked 15%. An rGO layer was also characterized and blocked 11%. From the incremental decrease in transmission it can be concluded that multiple coatings of the GO NC can be carried out in a uniform manner. Also it can be noted that one layer of rGO NC has a greater transparency than one layer of rGO even though the

electrochemical properties are enhanced for an rGO NC as compared to one layer rGO.

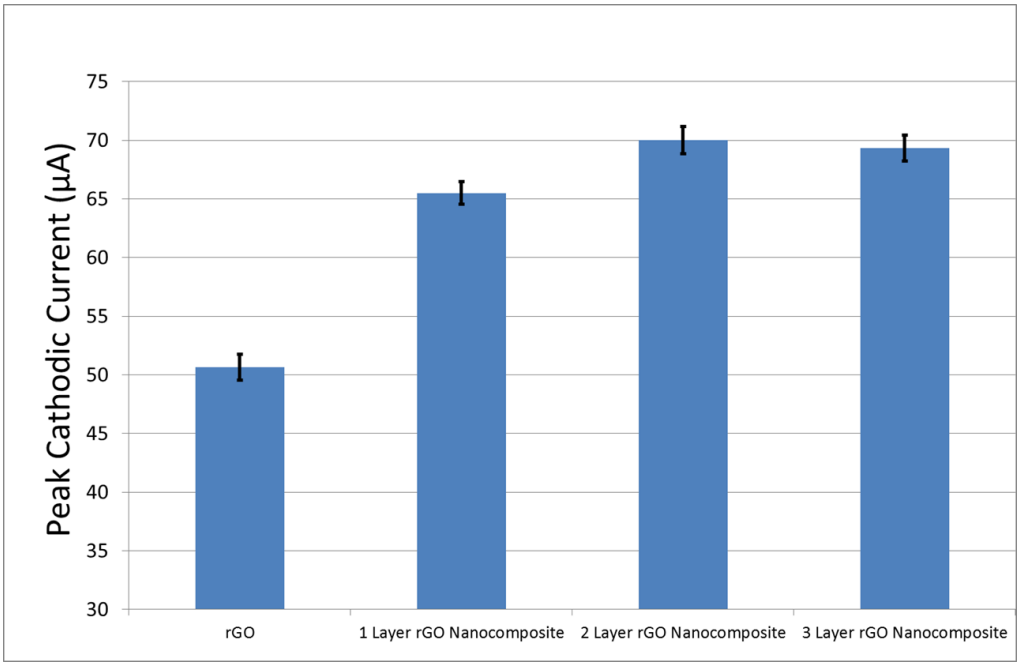

Figure 6.14. Peak cathodic currents of rGO, one layer rGO NC, two layer rGO NC and three layer rGO NC.

The peak cathodic currents of the multi layer rGO NC was characterized. Using the same conditions as the previous CV experiment, each sample data point was gathered 6 times and the error bars plotted from the standard deviation, showing good precision. As can be seen in Figure 6.14, there is an increase of 5 µA for two layer rGO NC, which is a 7 % increase from one layer rGO NC and a 40 % increase when compared to an rGO layer, with no further increase in peak current with a third layer. This is due to the porosity of the second layer increasing as compared to the first as seen in the RMS shifting from 7 nm for one layer to 10 nm for the second layer. Once the third layer is applied there is no more change in the RMS indicating porosity has not increased. This is why there is also no increase in the cathodic peak

current. From this data it can be seen that there is merit to consider applying a second rGO NC coating to increase signal currents but a third coating would be unnecessary.

6.3.5. Differential Pulse Voltammetry (DPV) detection of Serotonin

Serotonin or 5-hydroxytryptamine (5-HT) is a type of neurotransmitter that can be found in platelets, the intestinal tract and the central nervous system. 5-HT is manufactured in the brain and intestines and has a direct impact on mood, appetite, sleep, memory and sexual function.[60]

Figure 6.15 shows an 0.25 cm^2 rGO NC electrode detecting 5-HT using DPV. 100 µM injections of 5-HT were introduced into a 0.1M Na-PBS solution at pH 7.4 with the rGO NC electrode attached to a potentiostat. Oxidation of 5-HT occurred at 0.32 V which is in agreement with other reports of graphene based 5-HT detection.[61] The rGO NC displayed a sensitivity of 2.68 nA uM^{-1} cm^{-2}. This value shows superior sensitivities to other reported rGO based sensors towards 5-HT detection.[62–64]

The detection characteristics of rGO NC towards serotonin in the presence of interfering compounds were also investigated. Dopamine (DA) and ascorbic acid (AA) are compounds that are usually present in the human body alongside serotonin.[65] DA and AA was added to the solution and as seen in Figure 6.15, the rGO NC was able to resolve the DA/AA interfering peaks without affecting the serotonin peak. The DA/AA peak occurred at 0.15 V and increased in peak current as the two compounds were added. This overlap in oxidation peaks was first mentioned in Chapter 4, however in this case the

oxidation potential of serotonin was different enough for the peaks to be resolved and not interfere with serotonin detection. This shows that rGO NC is a good candidate as an active layer in biosensor designs.

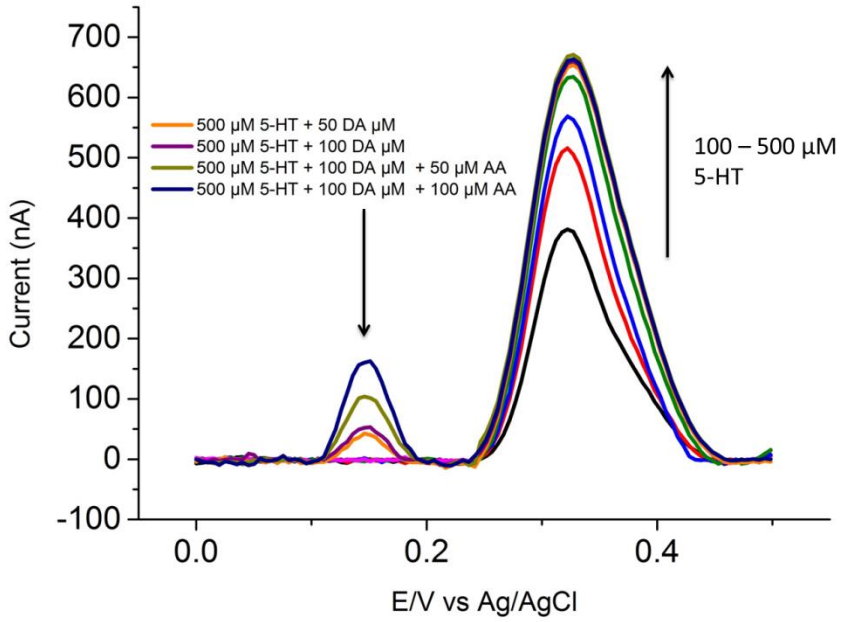

Figure 6.15. DPV spectra of Serotonin (5-HT) detection using one layer rGO NC with interfering dopamine (DA) and ascorbic acid (AA) compounds.

6.3.6. rGO NC Microelectrode Array Configuration

The rGO NC layer was also configured into an MEA using a reverse imprint method. A poly methyl methacrylate (PMMA) layer, patterned with periodic microelectrode holes, was transferred onto the rGO NC/ITO/PET substrate (Figure 6.16(a)). CV was used to determine if the device exhibited MEA characteristics using ruthenium (III) hexamine as the redox probe. Figure 6.16(b) shows sigmoidal CV spectra of the rGO NC device which is evidence of the PMMA transferred layer adhering well to the rGO NC layer and shows that the rGO NC is amenable to be used in an MEA platform.[15] The PMMA

layer transfer process still requires more optimization but shows promise as a facile method to configure 3D active layers into an MEA format.

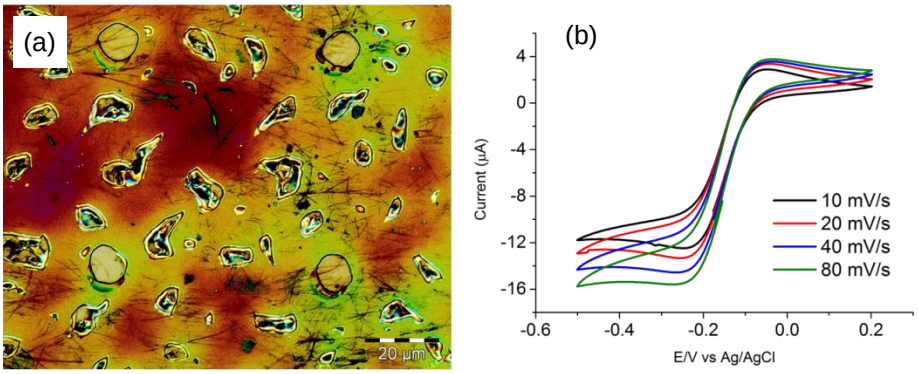

Figure 6.16. (a) Optical image of transferred PMMA layer onto rGO NC substrate. The 4 10 µm diameter microelectrode holes can be clearly seen. (b) CV voltammogram of the device showing MEA characteristics.

6.4. Conclusion

A method to synthesize an rGO NC electro active material that can be applied uniformly across a large area with increased output current was developed. A specific pH and concentration of Fmoc-FF is required in order to allow the nanocomposite to be spin coated as a uniform layer. However, more research needs to be conducted on the interdependence of concentration and pH of the Fmoc-FF solution to provide optimal conditions for uniform spin coating. The intermixing of the electroactive rGO flakes into the Fmoc-FF scaffold allowed for more active areas to be exposed to the environment providing greater signal currents. Multiple coatings of rGO NC were investigated and found that coatings beyond a second layer did not improve the performance of the sensor. However two coatings improved the current peak by 7%.

Serotonin was then detected using the rGO NC active layer in the presence of interfering compounds. The rGO NC layer was then configured into an MEA format. This work allows the increase of sensor performance by increasing the active areas sites without having to increase sensor size. A method to uniformly coat large areas which is superior to the conventional method of drop casting to test new electroactive materials was shown. The self-assembling Fmoc-FF scaffold can also be used with other materials and is not limited to GO.

6.5. References

1. Chen, S. in *Handb. Electrochem.* (ed. Zoski, C. G.) 33–III (Elsevier, 2007).
2. Bard, A. J. & Faulkner, L. R. *Electrochemical Methods: Fundamentals and Applications*. (Wiley, 2000).
3. Cao, Y., Smith, P. & Heeger, A. J. Counter-ion induced processibility of conducting polyaniline and of conducting polyblends of polyaniline in bulk polymers. *Synth. Met.* **48,** 91–97 (1992).
4. Tourillon, G. & Garnier, F. New electrochemically generated organic conducting polymers. *J. Electroanal. Chem. Interfacial Electrochem.* **135,** 173–178 (1982).
5. Macdiarmid, A. G., Chiang, J. C., Richter, A. F. & Epstein, A. J. Polyaniline: a new concept in conducting polymers. *Synth. Met.* **18,** 285–290 (1987).
6. Chen, P. & McCreery, R. L. Control of Electron Transfer Kinetics at Glassy Carbon Electrodes by Specific Surface Modification. *Anal. Chem.* **68,** 3958–3965 (1996).
7. Saby, C., Ortiz, B., Champagne, G. Y. & Bélanger, D. Electrochemical Modification of Glassy Carbon Electrode Using Aromatic Diazonium Salts. 1. Blocking Effect of 4-Nitrophenyl and 4-Carboxyphenyl Groups. *Langmuir* **13,** 6805–6813 (1997).
8. Huang, K.-J., Wang, L., Li, J., Yu, M. & Liu, Y.-M. Electrochemical sensing of catechol using a glassy carbon electrode modified with a composite made from silver nanoparticles, polydopamine, and graphene. *Microchim. Acta* **180,** 751–757 (2013).

9. Chen, Y.-C., Hsu, H.-L., Lee, Y.-T., Su, H.-C., Yen, S.-J., Chen, C.-H., Hsu, W.-L., Yew, T.-R., Yeh, S.-R., Yao, D.-J., Chang, Y.-C. & Chen, H. An active, flexible carbon nanotube microelectrode array for recording electrocorticograms. *J. Neural Eng.* **8,** 034001 (2011).
10. Castro Smirnov, J. R., Jover, E., Amade, R., Gabriel, G., Villa, R. & Bertran, E. Vertically aligned carbon nanotubes for microelectrode arrays applications. *J. Nanosci. Nanotechnol.* **12,** 6941–6947 (2012).
11. Pacios, M., Yilmaz, N., Martín-Fernández, I., Villa, R., Godignon, P., Del Valle, M., Bartrolí, J. & Esplandiu, M. J. A simple approach for DNA detection on carbon nanotube microelectrode arrays. *Sens. Actuators B Chem.* **162,** 120–127 (2012).
12. Brownson, D. A. C., Kampouris, D. K. & Banks, C. E. Graphene electrochemistry: fundamental concepts through to prominent applications. *Chem. Soc. Rev.* **41,** 6944–6976 (2012).
13. Ng, A. M. H., Wang, Y., Lee, W. C., Lim, C. T., Loh, K. P. & Low, H. Y. Patterning of graphene with tunable size and shape for microelectrode array devices. *Carbon* **67,** 390–397 (2014).
14. Yoon, H. J., Jun, D. H., Yang, J. H., Zhou, Z., Yang, S. S. & Cheng, M. M.-C. Carbon dioxide gas sensor using a graphene sheet. *Sens. Actuators B Chem.* **157,** 310–313 (2011).
15. Ng, A. M. H., Kenry, null, Teck Lim, C., Low, H. Y. & Loh, K. P. Highly sensitive reduced graphene oxide microelectrode array sensor. *Biosens. Bioelectron.* **65C,** 265–273 (2014).

16. Becerril, H. A., Mao, J., Liu, Z., Stoltenberg, R. M., Bao, Z. & Chen, Y. Evaluation of solution-processed reduced graphene oxide films as transparent conductors. *ACS Nano* **2,** 463–470 (2008).

17. Cai, B., Wang, S., Huang, L., Ning, Y., Zhang, Z. & Zhang, G.-J. Ultrasensitive Label-Free Detection of PNA–DNA Hybridization by Reduced Graphene Oxide Field-Effect Transistor Biosensor. *ACS Nano* **8,** 2632–2638 (2014).

18. Fu, C., Zhao, G., Zhang, H. & Li, S. Evaluation and Characterization of Reduced Graphene Oxide Nanosheets as Anode Materials for Lithium-Ion Batteries. *Int J Electrochem Sci* **8,** 6269–6280 (2013).

19. Guo, S. & Dong, S. Graphene nanosheet: synthesis, molecular engineering, thin film, hybrids, and energy and analytical applications. *Chem. Soc. Rev.* **40,** 2644–2672 (2011).

20. Aoki, K. Theory of ultramicroelectrodes. *Electroanalysis* **5,** 627–639 (1993).

21. Montenegro, M. I., Montenegro, I., Queirós, M. A. & Daschbach, J. L. *Microelectrodes: Theory and Applications: Theory and Applications*. (Kluwer Academic Publishers, 1991).

22. Wang, L., Zhang, Q., Chen, S., Xu, F., Chen, S., Jia, J., Tan, H., Hou, H. & Song, Y. Electrochemical Sensing and Biosensing Platform Based on Biomass-Derived Macroporous Carbon Materials. *Anal. Chem.* **86,** 1414–1421 (2014).

23. Dong, X., Wang, X., Wang, L., Song, H., Zhang, H., Huang, W. & Chen, P. 3D Graphene Foam as a Monolithic and Macroporous Carbon

Electrode for Electrochemical Sensing. *ACS Appl. Mater. Interfaces* **4,** 3129–3133 (2012).

24. Liu, M., He, S. & Chen, W. Co3O4 nanowires supported on 3D N-doped carbon foam as an electrochemical sensing platform for efficient H2O2 detection. *Nanoscale* **6,** 11769–11776 (2014).
25. Hoffman, A. S. Hydrogels for biomedical applications. *Adv. Drug Deliv. Rev.* **54,** 3–12 (2002).
26. Elisseeff, J. Hydrogels: Structure starts to gel. *Nat. Mater.* **7,** 271–273 (2008).
27. Zhao, Y., Liu, B., Pan, L. & Yu, G. 3D nanostructured conductive polymer hydrogels for high-performance electrochemical devices. *Energy Environ. Sci.* **6,** 2856–2870 (2013).
28. Oliveira, M. A. M., Boyer, C., Nele, M., Pinto, J. C., Zetterlund, P. B. & Davis, T. P. Synthesis of Biodegradable Hydrogel Nanoparticles for Bioapplications Using Inverse Miniemulsion RAFT Polymerization. *Macromolecules* **44,** 7167–7175 (2011).
29. Hoare, T. R. & Kohane, D. S. Hydrogels in drug delivery: Progress and challenges. *Polymer* **49,** 1993–2007 (2008).
30. Gupta, P., Vermani, K. & Garg, S. Hydrogels: from controlled release to pH-responsive drug delivery. *Drug Discov. Today* **7,** 569–579 (2002).
31. Tibbitt, M. W. & Anseth, K. S. Hydrogels as extracellular matrix mimics for 3D cell culture. *Biotechnol. Bioeng.* **103,** 655–663 (2009).
32. Jayawarna, V., Ali, M., Jowitt, T. A., Miller, A. F., Saiani, A., Gough, J. E. & Ulijn, R. V. Nanostructured Hydrogels for Three-Dimensional Cell

Culture Through Self-Assembly of Fluorenylmethoxycarbonyl–Dipeptides. *Adv. Mater.* **18,** 611–614 (2006).

33. Richter, A., Paschew, G., Klatt, S., Lienig, J., Arndt, K.-F. & Adler, H.-J. P. Review on Hydrogel-based pH Sensors and Microsensors. *Sensors* **8,** 561–581 (2008).
34. Bat, E., Lin, E.-W., Saxer, S. & Maynard, H. D. Morphing Hydrogel Patterns by Thermo-Reversible Fluorescence Switching. *Macromol. Rapid Commun.* **35,** 1260–1265 (2014).
35. Lee, E.-M., Gwon, S.-Y., Ji, B.-C. & Kim, S.-H. Temperature and acid/base-driven dual switching of poly(N-isopropylacrylamide) hydrogel with Azo dye. *Fibers Polym.* **12,** 142–144 (2011).
36. Atwe, A., Gupta, A., Kant, R., Das, M., Sharma, I. & Bhattacharya, S. A novel microfluidic switch for pH control using Chitosan based hydrogels. *Microsyst. Technol.* **20,** 1373–1381 (2014).
37. Okay, O. in *Hydrogel Sens. Actuators* (eds. Gerlach, G. & Arndt, K.-F.) **6,** 1–14 (Springer Berlin Heidelberg, 2009).
38. Hennink, W. E. & van Nostrum, C. F. Novel crosslinking methods to design hydrogels. *Adv. Drug Deliv. Rev.* **54,** 13–36 (2002).
39. Dasgupta, A., Mondal, J. H. & Das, D. Peptide hydrogels. *RSC Adv.* **3,** 9117–9149 (2013).
40. Banwell, E. F., Abelardo, E. S., Adams, D. J., Birchall, M. A., Corrigan, A., Donald, A. M., Kirkland, M., Serpell, L. C., Butler, M. F. & Woolfson, D. N. Rational design and application of responsive α-helical peptide hydrogels. *Nat. Mater.* **8,** 596–600 (2009).

41. Altunbas, A. & Pochan, D. J. Peptide-based and polypeptide-based hydrogels for drug delivery and tissue engineering. *Top. Curr. Chem.* **310,** 135–167 (2012).

42. Jonker, A. M., Löwik, D. W. P. M. & van Hest, J. C. M. Peptide- and Protein-Based Hydrogels. *Chem. Mater.* **24,** 759–773 (2012).

43. Seow, W. Y. & Hauser, C. A. E. Short to ultrashort peptide hydrogels for biomedical uses. *Mater. Today* **17,** 381–388 (2014).

44. Huang, R., Qi, W., Feng, L., Su, R. & He, Z. Self-assembling peptide–polysaccharide hybrid hydrogel as a potential carrier for drug delivery. *Soft Matter* **7,** 6222 (2011).

45. Chung, H. J. & Park, T. G. Self-assembled and nanostructured hydrogels for drug delivery and tissue engineering. *Nano Today* **4,** 429–437 (2009).

46. Ryu, J., Kim, S.-W., Kang, K. & Park, C. B. Mineralization of Self-assembled Peptide Nanofibers for Rechargeable Lithium Ion Batteries. *Adv. Mater.* **22,** 5537–5541 (2010).

47. Tang, C., Ulijn, R. V. & Saiani, A. Effect of Glycine Substitution on Fmoc–Diphenylalanine Self-Assembly and Gelation Properties. *Langmuir* **27,** 14438–14449 (2011).

48. Yemini, M., Reches, M., Rishpon, J. & Gazit, E. Novel Electrochemical Biosensing Platform Using Self-Assembled Peptide Nanotubes. *Nano Lett.* **5,** 183–186 (2005).

49. Xing, P., Chu, X., Li, S., Ma, M. & Hao, A. Hybrid Gels Assembled from Fmoc-Amino Acid and Graphene Oxide with Controllable Properties. *ChemPhysChem* **15,** 2377–2385 (2014).

50. Tang, C., Smith, A. M., Collins, R. F., Ulijn, R. V. & Saiani, A. Fmoc-Diphenylalanine Self-Assembly Mechanism Induces Apparent pKa Shifts. *Langmuir* **25,** 9447–9453 (2009).

51. De, S. K., Aluru, N. R., Johnson, B., Crone, W. C., Beebe, D. J. & Moore, J. Equilibrium swelling and kinetics of pH-responsive hydrogels: models, experiments, and simulations. *J. Microelectromechanical Syst.* **11,** 544–555 (2002).

52. Raposo, M., Ferreira, Q. & Ribeiro, P. A. A guide for atomic force microscopy analysis of soft-condensed matter. *Mod. Res. Educ. Top. Microsc.* **1,** 758–769 (2007).

53. Zhou, M., Smith, A. M., Das, A. K., Hodson, N. W., Collins, R. F., Ulijn, R. V. & Gough, J. E. Self-assembled peptide-based hydrogels as scaffolds for anchorage-dependent cells. *Biomaterials* **30,** 2523–2530 (2009).

54. Fung, S. Y., Keyes, C., Duhamel, J. & Chen, P. Concentration Effect on the Aggregation of a Self-Assembling Oligopeptide. *Biophys. J.* **85,** 537–548 (2003).

55. Smith, A. Fibril formation by short synthetic peptides. *Subcell. Biochem.* **65,** 29–51 (2012).

56. Toh, S. Y., Loh, K. S., Kamarudin, S. K. & Daud, W. R. W. Graphene production via electrochemical reduction of graphene oxide: Synthesis and characterisation. *Chem. Eng. J.* **251,** 422–434 (2014).

57. Chen, Y., Zhang, X., Zhang, D., Yu, P. & Ma, Y. High performance supercapacitors based on reduced graphene oxide in aqueous and ionic liquid electrolytes. *Carbon* **49,** 573–580 (2011).

58. Abellán, G., Martínez, J. G., Otero, T. F., Ribera, A. & Coronado, E. A chemical and electrochemical multivalent memory made from FeNi3-graphene nanocomposites. *Electrochem. Commun.* **39,** 15–18 (2014).

59. Zhu, X., Yan, Z., Wu, W., Zeng, W., Du, Y., Zhong, Y., Zhai, H., Ji, H. & Zhu, Y. Manipulating Size of Li3V2(PO4)3 with Reduced Graphene Oxide: towards High-Performance Composite Cathode for Lithium Ion Batteries. *Sci. Rep.* **4,** (2014).

60. Lesch, K.-P., Bengel, D., Heils, A., Sabol, S. Z., Greenberg, B. D., Petri, S., Benjamin, J., Müller, C. R., Hamer, D. H. & Murphy, D. L. Association of Anxiety-Related Traits with a Polymorphism in the Serotonin Transporter Gene Regulatory Region. *Science* **274,** 1527–1531 (1996).

61. Xue, C., Wang, X., Zhu, W., Han, Q., Zhu, C., Hong, J., Zhou, X. & Jiang, H. Electrochemical serotonin sensing interface based on double-layered membrane of reduced graphene oxide/polyaniline nanocomposites and molecularly imprinted polymers embedded with gold nanoparticles. *Sens. Actuators B Chem.* **196,** 57–63 (2014).

62. Valentini, F., Romanazzo, D., Carbone, M. & Palleschi, G. Modified Screen-Printed Electrodes Based on Oxidized Graphene Nanoribbons for the Selective Electrochemical Detection of Several Molecules. *Electroanalysis* **24,** 872–881 (2012).

63. Alwarappan, S., Erdem, A., Liu, C. & Li, C.-Z. Probing the Electrochemical Properties of Graphene Nanosheets for Biosensing Applications. *J. Phys. Chem. C* **113,** 8853–8857 (2009).

64. Valentini, F., Roscioli, D., Carbone, M., Conte, V., Floris, B., Palleschi, G., Flammini, R., Bauer, E. M., Nasillo, G. & Caponetti, E. Oxidized Graphene in Ionic Liquids for Assembling Chemically Modified Electrodes: A Structural and Electrochemical Characterization Study. *Anal. Chem.* **84,** 5823–5831 (2012).

65. Zhou, J., Sheng, M., Jiang, X., Wu, G. & Gao, F. Simultaneous Determination of Dopamine, Serotonin and Ascorbic Acid at a Glassy Carbon Electrode Modified with Carbon-Spheres. *Sensors* **13,** 14029–14040 (2013).

Chapter 7. Conclusion

7.1. Summary and Outlook

This thesis reports the patterning, manipulation and electrochemical sensing properties of graphene and its derivatives in a microelectrode array configuration. Graphene is a material that has been characterized to have remarkable properties but in order to realize graphene devices, methods to selectively shape and place graphene in designated areas must be developed.

In Chapter 3, a method to cut and shape single layer graphene sheets using nanoimprint lithography (NIL) was presented. Utilizing NIL, graphene sheets that could be patterned into various size and shapes, from hexagonal rings to 5 μm discs and sub-micron graphene ribbons was shown. The patterned graphene could then be transferred onto other substrates by PMMA encapsulation. A graphene microelectrode array sensor (MEA) device was fabricated using a novel self-aligning technique that allowed the patterning of a graphene layer into an MEA configuration. The device was used to detect the hydrogen peroxide secreted by MCF-7 Breast cancer cells that were seeded at a low density of 3000 cm^{-2} showing the potential of NIL use in graphene MEA fabrication.

In Chapter 4, further development of the MEA process was carried out by fabricating a flexible reduced graphene oxide biosensor. Consisting of fully biocompatible materials, the sensor demonstrated performances that were superior in sensitivity to other reported rGO based electrodes towards

dopamine. The device could be readily cleaned and integrated into a microfluidic system showing good potential as a biosensor platform.

In the design and fabrication of an MEA, the greater the density of microelectrodes the greater the sensitivity of the device. However there is an upper limit to this density before microelectrodes are spaced too closely together and cause diffusion hemisphere overlap. When overlap occurs, the MEA device operates in a macroelectrode regime and loses advantageous microelectrode characteristics. In Chapter 5 the optimum pitch spacing ratio of interelectrode distance to microelectrode radius was reported. Using a series of rGO MEAs with varying interelectrode distances, CV was employed to characterize when the pitch spacing was sufficient to allow an rGO MEA to operate in the microelectrode array regime. This value was found to be 15.7 times the microelectrode radius and can be used as a guide rule for future rGO MEA fabrication.

Chapter 6 explores a new composite active layer material made from a self-assembling peptide Fmoc-FF mixed with GO. The conditions under which the hydrogel could be uniformly spin coated was first investigated, adjusting pH and peptide concentrations so that peptide fibrils would form as a scaffold layer without forming large clusters within the solution that could not be uniformly spin coated. The hydrogel network acted as a scaffold for the rGO flakes which allowed more active sites to be exposed to the environment. This resulted in a 40 % increase in detected current for a two coating layer, showing that a sensor's sensitivity can be increased without having to increase its footprint size through the use of the self-assembling hydrogel. The rGO NC was then used to detect serotonin even in the presence of dopamine and

ascorbic acid interference. An etch free MEA fabrication method, using a reverse PMMA transfer technique was then used to configure the rGO composite layer into an MEA format. The rGO NC showed its promise as an electroactive layer that could a) Increase biosensor performance and b) Be readily synthesized over a large area through self-assembly.

It is undeniable that graphene has the potential to impact a vast array of applications. This dissertation shows one of these areas being the field of biosensing. The healthcare industry is an ever growing field and biosensors play an integral part in clinical and non clinical diagnostics. Research and development is constantly looking for ways to improve the portability, sensitivity and manufacturing expenses of these devices. Graphene with its unique electrical, mechanical and biocompatible properties has spurred a large drive to fabricate graphene based biosensors.

Further work still remains on how graphene based device fabrication processes can be scaled up. However with graphene being researched across the globe in various disciplines, it will only be a matter of time before graphene-based devices move from the research lab to the marketplace.

Appendices

Appendix A. XPS data of GO and rGO.

XPS analysis was carried out on GO and rGO to elucidate the type of oxygen functional groups that were removed from the GO flakes during reduction.

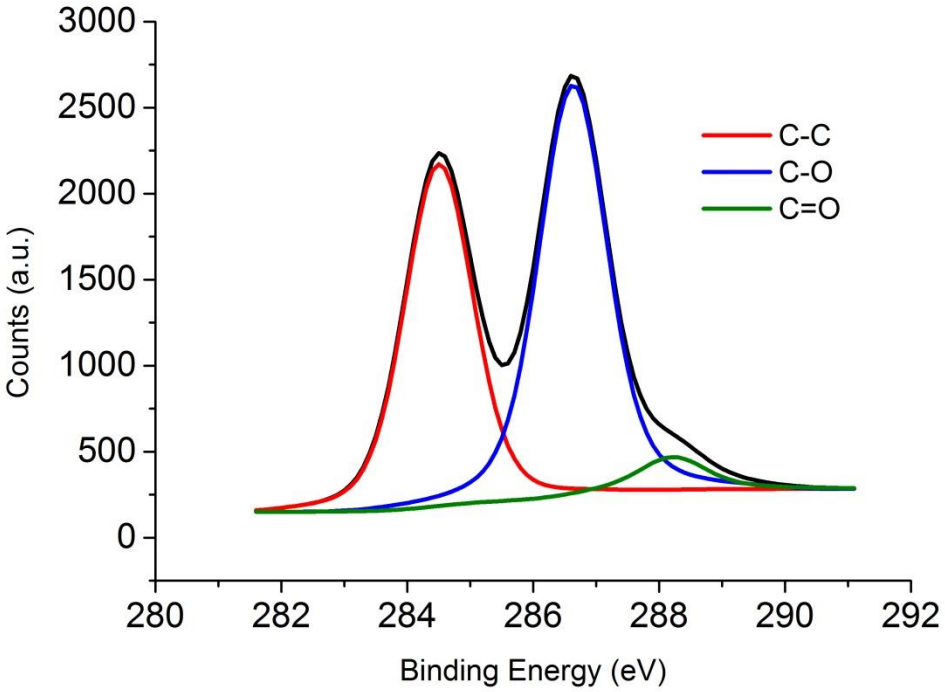

Figure s1. XPS spectra of GO

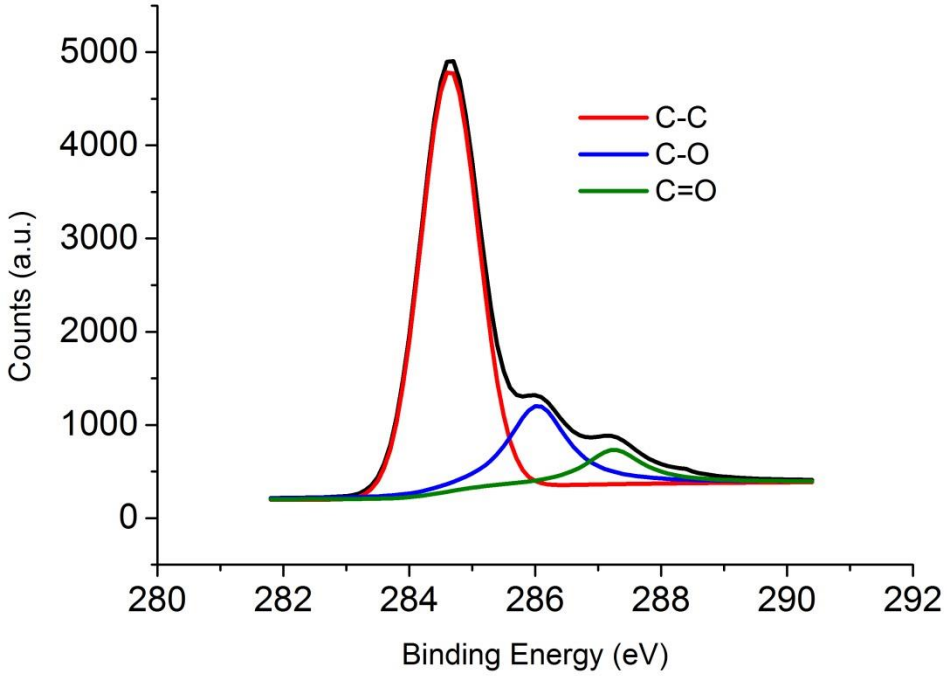

Figure s2. XPS spectra of rGO

Curve fitting was performed for both samples of the C1s spectra found in figures s1 and s2. Table s1 below contains the corresponding bond types, binding energies and the proportions found in the GO and rGO samples.

Table s1. XPS data of oxygen groups found in GO and rGO.

	GO			rGO		
Bond Type	C-C	C-O	C=O	C-C	C-O	C=O
Binding Energy (eV)	284.5	286.6	288.2	284.6	286	287.7
Proportion (%)	42.9	52.6	4.5	70.7	19.6	9.7

Initially the epoxy, hydroxyl and carbonyl groups found at binding energies 286.6 and 288.2 in GO have a deconvoluted peak intensities of a 57.1% relative to the total peak intensity, however upon reduction the composition drops to 29.3%. The significant reduction in sp3-bonded sites due to oxygen groups allows rGO to 'regain' electroactive characteristics. As seen in the table, the hydroxyl and epoxy groups display a major reduction in peak intensities after reduction.

Appendix B. CV behaviour of 30, 60 80 andn 120 µm rGO MEA pitch spacing.

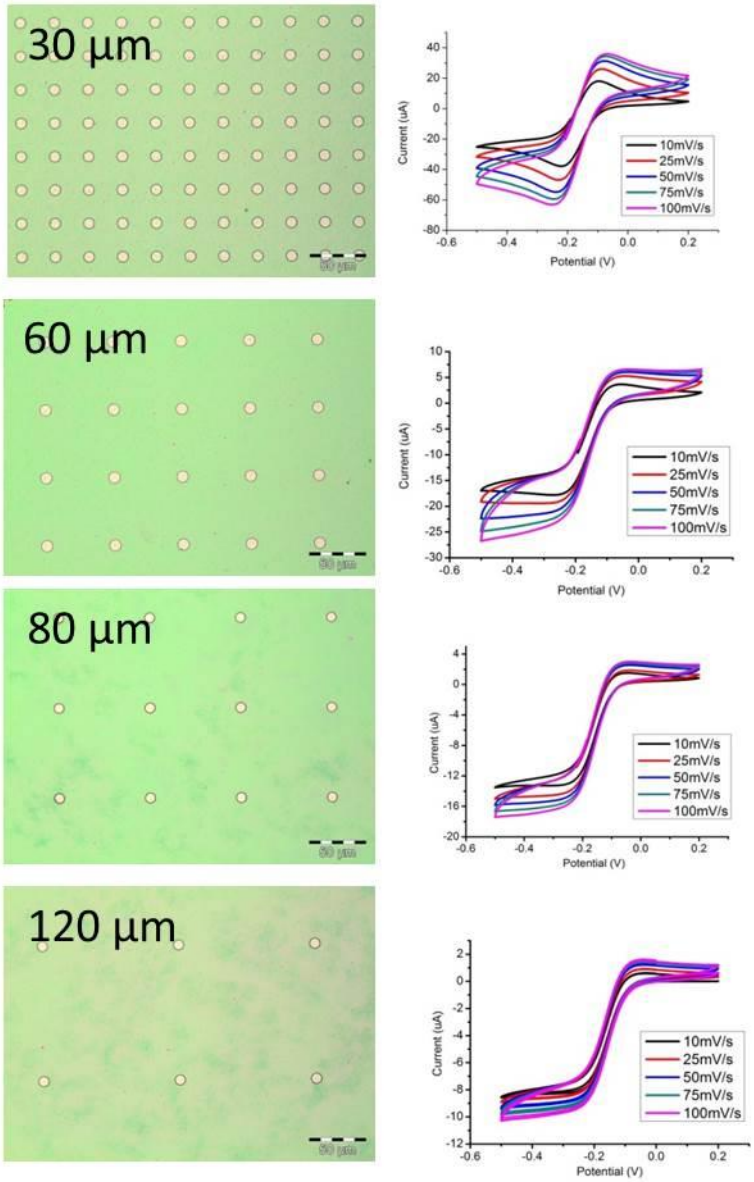

Figure s3. 30 to 120 µm rGO MEA pitch spacings and corresponding CV spectra.

Initial experiments (Figure 1) used 30, 60, 80 and 120 µm pitch spacings using the same CV setup reported. It was found that a sigmoidal spectra of 0% depletion was first seen at 60 um 25 mV/s scan rate. In order to increase the precision of determining the minimum pitch spacing for microelectrode array

behavior to occur, further experiments were carried out using 60, 64, 68 and 70 μm, which is the data set that was finally reported in the thesis.

In the above CV spectra data set at pitch spacings of 80 um and above, sigmoidal behavior can be seen at 10 mV/s.